Investigating the effects of impermeant anions on the electrical and computational properties of neurons

Presented by:

Dr. Eran F. Shorer

SHRERA001

Supervised by:

A.Prof Joseph V. Raimondo

Submitted to the Department of Human Biology at the Faculty of Health Sciences of the University of Cape Town in fulfillment of the academic requirements for a **Masters of Medical Science in Neuroscience (Physiology)**

June 2022

Anti-Plagiarism Declaration

1. I know that plagiarism is wrong. Plagiarism is using another's work and ppretendingthat it is one's own.

2. I have used the Journal of Neuroscience convention for citation and referencing. Each contribution to, and quotation in, this report from the work(s) of other people has been attributed and has been cited and referenced.

3. This report is my own work.

4. I have not allowed, and will not allow anyone to copy my work with the intention of passing it off as their own work or part thereof.

June 2022

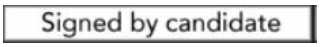

Eran Frank Shorer

Acknowledgments

Although this thesis bears my name and I will be bestowed the degree, its completion is anything but a solo accomplishment; it is a puzzle that required several pieces to serendipitously fall into place. Most crucially, my supervisor - Joe. This project would never have been born without the trust and willingness to shepherd a medical student wanting to explore his passion for neuroscience and computing. I not only learned so much about the scientific process and rigors of theoretical exploration, but I observed the human element of managing the lab and its members whilst balancing multiple academic, personal, and societal responsibilities. Lessons from his mentorship and approach to science are the cement I will use to build my career as I construct a scientist in his image.

Another core piece of this puzzle is Dr. Kira Dusterwald and Dr. Christopher Currin whose work I have so heavily relied on. Chris introduced me to the world of biophysical modeling and inadvertently set me off on an alternate career trajectory which aligns mwith any of my passions; while Kira and Joe's genius provided much of the theoretical framework such that I could explore impermeant anions with sound foundational backing.

Despite a wealth of guidance, this project required me to step out of medical internship such that I would be without salary. The financial means to take this project forward were generously supplied by the David and Elaine Potter Foundation, funding provided by grants given to my supervisor (Joe), and additional support from my parents.

Science is never performed in isolation - thank you to my friends and family that created the environment of support and patience required to nurture research. My mum, dad, and brother fostered my interest in science from a young age and sustained me financially at every step of the way. I could not be luckier to have had their love and support.

The production of this thesis is truly an accomplishment for all those who supported me. They deserved to be as proud of it as I am.

Abstract

Impermeant anions (proteins, amino acids, etc.) are negatively charged ions that are unable to traverse the cell membrane. Impermeant anion quantities and their average charge vary with metabolism as well as protein and nucleic acid synthesis/turnover. The effect of spatiotemporal changes to impermeant anions on neurons is poorly understood. Using a multicompartment electrodiffusion-based computational model I investigated the influence of impermeant anions on neuronal cellular physiology, passive cable properties, and synaptic integration. Spatial differences in the average charge of impermeant anions result in a non-isopotential dendrite with ionic microdomains. At steady state local discrepancies in membrane potentials and ion concentrations do not impact the passive or active electrical properties of neurons as ionic driving forces are unchanged, irrespective of impermeant anion mean charge. These findings explain how electrical signalling remains consistent in the face of an ever-changing impermeant anion milieu with implications related to our understanding of both normal and pathological neuronal physiology.

CONTENTS

List of Tables & Figures:

List of Abbreviations and Symbols

A_m	membrane area scaling parameter – surface area divided by volume
APs	action potentials
CCC	cation-chloride cotransporter
Cl^-	chloride ion
C_m	membrane capacitance
Δ	delta, meaning colloquially difference or change between
DF	driving force of an ion – difference between the membrane potential and the ion's reversal potential
dt	time step (seconds)
D_{ion}	diffusion constant for an ion in an aqueous medium
dx	size of the distance step between two compartments
ED	electrodiffusion
E_{ion}	reversal/equilibrium/Nernst potential for an ion
E_{GABA}	reversal potential through type A γ-aminobutyric acid receptors
E_{NMDA}	reversal potential through N-methyl-D-aspartate receptors
EPSP	excitatory post-synaptic potential
Eq.	equation
F	the Faraday constant, 96485.3329 $s \cdot A \cdot mol^{-1}$
Fig.	figure
g_{ion}	conductance of an ion across the membrane
$GABA_ARs$	type A γ-aminobutyric acid receptors
GHK	Goldman-Hodgkin-Katz (equation)
HCO_3^-	bicarbonate ion
HH	Hodgkin-Huxley (channel type)
H_p	hydrostatic pressure
H_2O	water
I	current in amperes
$[ion]_i$	concentration of an ion in the intracellular compartment
$[ion]_o$	concentration of an ion in the extracellular compartment
IPSP	inhibitory post-synaptic potential
J_R	flux through transporter *R*
K^+	potassium ion
KCC2	potassium-chloride cotransporter type 2
k_m	membrane tension
l	length
ln	natural logarithm
μ_{ion}	mobility constant for a particular ion
n	number of moles
N_A	Avogadro's constant for the number of molecules in a mole, 6.0221408×10^{23} mol^{-1}
Na^+	sodium ion
Na^+/K^+ *ATPase*	sodium potassium ATPase pump
NKCC1	sodium potassium chloride cotransporter type 1
NMDARs	N-methyl-D-aspartate receptors
NPE	Nernst-Plank Equation
P	sodium potassium ATPase pump constant
$P_{m\ ion}$	membrane permeability constant for a particular ion

π	the constant pi, 3.14159265356
Π_i / Π_o	intracellular/extracellular osmolarity
p_w	osmotic permeability of a membrane
q	charge in coulombs
r	radius
r_t	fraction of bound receptor at time point t (in relation to synaptic pulse)
R	the gas constant, 8.3144598 $J \cdot mol^{-1} \cdot K^{-1}$
R_{ion}	resistance of an ion across the membrane
SA	surface area
t	time
TM	transmembrane
V_m	membrane potential (mV)
v_w	partial molar volume of water
w	volume
X^z	group of impermeant anions, with mean charge (valence) of z
z_{ion}	mean charge of a particular ion

1. INTRODUCTION

1.1. CELLULAR ARCHITECTURE AND ELECTRICAL PROPERTIES OF NEURONS

1.1.1. BUILDING BLOCKS OF THE BRAIN

Neurons are the functional units of the brain. They receive inputs, transform them, and produce output signals targeting other neurons. Common cellular components – somata, dendrites, and axons - facilitate signal propagation between neurons. (**Fig 1.1**).

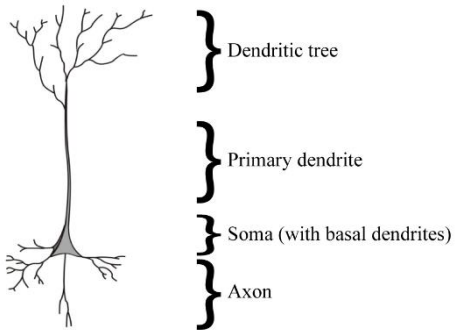

Fig. 1.1: Morphology of a neuron

Inside the soma (cell body) of the neuron lies the cell nucleus and other cellular organelles loosely embedded in a gel-like cytoplasm. Here ribosomes and endoplasmic reticula synthesize proteins and other macromolecules which provide structural integrity and maintain neuronal homeostasis.

Slender cytoplasmic extensions called dendrites conduct electrical signals toward the soma from apical and basal regions. Primary dendrites extend from the soma and branch out distally forming the dendritic tree. Dendritic branches narrow and contain fewer cellular organelles as the tree lengthens (Hammond, 2015). Electrical signals entering via dendrites are neural inputs that get integrated and transformed.

Should the summation of incoming inputs reach a threshold, the neuron discharges an action potential (output signal) down its axon. The terminal end of an axon communicates with a dendrite of another neuron forming a synapse, the basis for neural signal transfer.

1.2.1. NEURAL SIGNAL PROPAGATION

Synapses are chemical-electrical interfaces between communicating neurons. An activated pre-synaptic neuron releases chemical neurotransmitters which bind to receptor proteins on the post-synaptic neuron. Interaction with a neurotransmitter then transforms the structure of the receptor to become a channel for ion flux between the extracellular environment and the neuron.

The magnitude and direction of ionic flux determines the electrical effect on the post-synaptic membrane. Ionic motion across the membrane either increases (depolarizes) or decreases (hyperpolarizes) the post-synaptic membrane potential, ultimately contributing to excitatory or inhibitory signalling. Excitatory signalling increases the likelihood of triggering an action potential, while inhibitory signalling reduces the likelihood. Tight control of excitatory and inhibitory signalling underpins precise neural communication.

1.3.1. IONIC HOMEOSTASIS IN NEURONS AND THE NERNST POTENTIAL

Ionic homeostasis refers to the self-regulating control mechanisms involved in stabilizing ion concentrations. In neurons, ion homeostasis is what ensures most neurons remain at rest, while only specific neurons are activated. Ions enter and exit neurons across a semi-permeable membrane that acts as a gatekeeper against most ionic fluxes.

Two forces govern ionic motion across the semipermeable membrane. Firstly, *diffusion* - the movement of ions from a region of high ionic concentration to a region of low concentration. Water follows ionic motion across the membrane via *osmosis* such that osmotic balance is maintained. Secondly, *drift* - the flux of charged molecules due to the local electrical field. The net flux of ions therefore is a combination of both chemical and electrical forces.

The *Nernst-Planck Equation* (NPE) is used to calculate the magnitude and direction of ion flux. The equation summates Fick's Law of Diffusion and Ohm's Law for Drift by using the Einstein Relation stating that fluxes of diffusion and drift are additive in the same medium (flux = *drift* + *diffusion)*.

In steady state (resting) conditions, the net flux of an ion is equal to zero, and the NPE can be rearranged (- *drift* = *diffusion*) to find the electrical potential required to maintain an ion concentration gradient across the membrane. This voltage is also referred to as the Nernst potential, reversal potential, or equilibrium potential of an ion (Coombs et al., 1955). Multiple

ionic species exist on either side of the membrane and thus the Nernst equation cannot be used to determine the potential of the entire membrane.

1.4.1. MEMBRANE POTENTIAL AND IONIC DRIVING FORCES

The "charge-sum" and "charge-difference" approach are two popular methods to calculate the resting membrane potential (V_m). The "charge-sum" approach models the neuronal membrane as an equivalent circuit and then uses Kirchhoff's Current Law, which states that the total current entering a junction or a node equals the charge leaving the node. Therefore, the summation of currents is equal to zero ($I_{Capacitance} + I_{ion} = 0$) which becomes a differential equation that is solvable. The solution however requires the initialization values to be known. The "charge-difference" method (Fraser and Huang, 2004) provides the same solution for Vm (**Eq. 1.1**), without requiring initialization values, by utilizing the formula for capacitance ($C_m = q/V_m$). Charge (q) is the difference between the extracellular and intracellular ion charges. As a neuron existing in a neutral extracellular environment will have an extracellular charge of zero, only the intracellular charge is considered. The intracellular charge is the differences between cations and anion concentrations, divided by the cell volume to arrive at a net mole. This value is multiplied by Faraday's constant (F) to convert mol to coulombs.

$$V_m = \frac{F \times ([Na^+]_i + [K^+]_i - [Cl^-]_i + z[X^-]_i) \times w}{C_m} \quad \textbf{(Eq.1.1)}$$

In the charge-difference equation, $[Na^+]_i$ represents sodium concentration, $[K^+]_i$ is the potassium concentration, $[Cl^-]_i$ is the chloride concentration. $[X^-]_i$ refers to the concentration of impermeant anions, with a mean charge of z.

The membrane potential (V_m) of a neuron at rest lies within the range of - 40 to - 80mV (depending on cell type), indicating that the composition of the internal neuron environment consists of more net negative than positive charges. **Fig. 1.2** shows the concentration gradients across the membrane which set up the membrane potential.

Ion	Intracellular concentration (mM)	Extracellular concentration (mM)	Reversal potential (E_{ion}) (mV)
Sodium Na^+	5-15	145	90.7 - 61.1
Potassium K^+	140	5	- 89.7
Chloride Cl^-	4	110	- 89
Bicarbonate HCO_3^-	10	24	- 23

Table 1.2: Table of ion concentrations and ionic reversal (equilibrium) potentials in neurons.

The driving force (DF) of an ion is equal to the difference between the membrane potential and its equilibrium potential (V_m - E_{ion}) and is the net force acting on the ion at rest. To calculate the ionic current for a particular ion (I_{ion}) across the membrane due to its driving force Ohm's law (I = V/R) can be used, shown in **Eq.1.2**.

$$I_{ion} = g_{ion}(V_m - E_{ion}) \quad \textbf{(Eq.1.2)}$$

The inverse of resistance (1/R), conductance (g_{ion}), is often preferred in neuroscience as it intuitively relates to how easily an ion can cross the membrane. This is determined by the number of open ion channels at a given time. Altered membrane conductances to specific ions at discrete time intervals underpins ionic flux across the semipermeable membrane – the basis of neural communication. However, not all ions are able to cross the membrane (impermeant ions), yet how these impermeant ions might influence neural signalling is not well understood.

1.2. IMPERMEANT ANIONS

1.2.1. PROPERTIES OF IMPERMEANT ANIONS

The three major anion species in the brain are chloride (Cl^-), bicarbonate (HCO_3^-), and impermeant anions. Impermeant molecules (some anionic some cationic) are defined by their inability to traverse the cell membrane. Although, no experimental studies characterise local impermeant molecular charge in neurons, analytically, the average (bulk) charge of all intracellular impermeant molecules is approximated as -0.85 (Düsterwald et al., 2018) when impermeant molecule concentrations are known. In this thesis we consider these molecules in bulk and refer to them as impermeant anions.

Impermeant anions make up a heterogenous milieu of molecules including sulphates (SO^{4-}), phosphates (PO^{4-}), phosphorylated molecules such as ribonucleotides, metabolic end products and other intracellular proteins (such as actin and tubulin) and which are negatively charged at physiological pH (Burton, 1983; Glykys et al., 2014a; Rahmati et al., 2021). The core impermeant anion properties of functional importance are 1) concentration, 2) charge, and 3) distribution.

There are approximately 10000 protein types in the CNS (contributing to the milieu of impermeant molecules), with the majority having an isoelectric point (pI) less than a pH of 7 (Gianazza, and Righetti, 1980; Morón and Devi, 2007). At physiological pH most proteins will donate protons and exist as a weak base with a negative charge. The charge of impermeant anions likely varies on the local pH and abundance of phosphate groups among other factors.

Impermeant anions are distributed both intracellularly and extracellularly. Intracellularly, proteins are non-uniformly dispersed in the cytoplasm because cellular machinery for protein synthesis occurs at differing spatial locations. Large macromolecules (for instance microtubules modified with polyglutamate chains) are relatively immobile along the dendrite (Liu et al., 2013), while smaller impermeant anions may travel along dendrites via cytoplasmic transport mechanisms (Koleske, 2013). The distribution of impermeant anions is understudied, however for the purpose of this thesis they are assumed to be able to vary at fixed locations and are not diffusable.

Extracellularly, impermeant anion distribution is more stable. The most prominent extracellular impermeant anions are scaffolding proteins such as proteoglycans which anchor neurons to the extracellular matrix (Cui et al., 2013; Thul et al., 2017).
Individual proteins and cellular macromolecules have specific functions ranging from DNA replication to neurotransmission; however, when considered collectively on the basis of their cumulative charge and osmotic activity impermeant anions are a core component of what establishes membrane potential and cell volume.

1.2.2. IMPERMEANT ANIONS, THE PUMP LEAK MECHANISM, AND MAINTENANCE OF CELL VOLUME

Impermeant anions cannot cross the semipermeable membrane yet still contribute to the osmotic load in a cell, a phenomenon referred to as the Donnan Effect (Donnan, 1911). In the absence of ion pumps, impermeant anions (and the cations attracted to them) passively draw in water resulting in osmotic instability that can lead to cell swelling and lysis (Blaustein et al., 2012; Sperelakis, 2012; Kay, 2017).

To counteract the Donnan Effect, animal cells utilize ion pumps to shift ions against their concentration gradient – moving water out of the cell in the process. The sodium-potassium ATPase (Na-K ATPase), the most crucial active transport mechanism, pumps three Na^+ ions out of the neuron in exchange for two K^+ ions which enter (Tosteson and Hoffman, 1960). The excess of negative ions in the cell results in a negative resting membrane potential.

The Donnan Effect and ion pumps ultimately create electrochemical gradients to maintain cell volume. Leak channels in the cell membrane permit ions to move down electrochemical gradients to achieve electroneutrality. This system is referred to as the "pump-leak mechanism" (Kay, 2017) and is what couples cell volume and resting membrane potential of animal cells. Although impermeant anions are crucial in the regulation of neural homeostasis, their role in neural signalling remains controversial.

1.3. INHIBITORY SIGNALLING AND IMPERMEANT ANIONS

Communication between neurons necessitates a delicate control of excitatory and inhibitory signals. Inhibition is vital for controlling when and where particular neurons are active, thereby enabling precise neural activity. Moreover, many neurons are recurrently connected so without inhibitory control widespread excitation would occur (Doyon et al., 2016). Faults in inhibition lead to an array of neurological and psychiatric disorders including epilepsy (Alfonsa et al., 2015), schizophrenia (Taylor and Tso, 2015), and Huntington's disease (Hsu et al., 2018). Discovery of molecular treatments for these disorders relies upon understanding the intricate cellular physiology underpinning neural inhibition.

1.3.1. GABA MEDIATES INHIBITION VIA CHLORIDE INFLUX

Fast synaptic inhibition is predominantly mediated by the neurotransmitter GABA (γ-aminobutyric acid) binding to $GABA_A$ receptors. Binding changes the receptor's conformation to act as transmembrane ion channel permeable to Cl^- (and to a lesser extent HCO_3^-) (Kaila, 1992). Inward movement of Cl^- hyperpolarizes (inhibits) neurons.
The $GABA_A$ receptor, however, is permeable to Cl^- in both directions. The direction of Cl^- flux is set by the Cl^- driving force (DF; **Eq.1.3**), which is the difference between the membrane potential (V_m) and the Cl^- reversal potential (E_{Cl}; **Eq.1.4**).

$$DF_{Cl} = V_m - E_{Cl} \quad \textbf{(Eq.1.3)}$$

$$E_{Cl} = \frac{-RT}{F} \times ln\left(\frac{[Cl_{out}]}{[Cl_{in}]}\right) \quad \textbf{(Eq.1.4)}$$

At a stable membrane potential, E_{Cl} dictates the direction of Cl^- flux. Under these circumstances, inhibition (Cl^- influx) can only occur if the intracellular Cl^- concentration remains low (Ben-Ari, 2002). Minor increases in intracellular Cl^- concentrations can tilt the $[Cl_{out}]$: $[Cl_{in}]$ ratio leading to Cl^- extrusion through $GABA_A$ receptors and a paradoxical depolarizing excitatory current (Raimondo et al., 2017). Neural inhibition therefore depends on establishing and maintaining Cl^- concentration gradients.

1.3.2. DETERMINANTS OF CHLORIDE CONCENTRATION

Both intracellular and extracellular Cl^- concentrations are regulated by dynamic systems. Extracellular Cl^- concentration is tightly controlled by the renal and gastrointestinal system

(serum Cl^-) , and is further regulated in the CSF by the choroid plexus(Abbott et al., 1971), rendering the extracellular Cl^- concentration as effectively constant. The focus of this thesis is on internal Cl^- concentration, which is predominantly determined by chloride cotransporters (CCCs)(Blaesse et al., 2009) and impermeant anions (Düsterwald et al., 2018).
Chloride cotransporters are a family of ion transporters which utilize secondary active transport mechanisms (either Na^+ or K^+ concentration gradients) to alter Cl^- concentrations (Kahle et al., 2015). The two most prominent CCCs in the nervous system are NKCC1 and KCC2.

The KCC2 transporter is the most important regulator of Cl^- in adult neurons (Rivera et al., 1999; Ben-Ari, 2002). KCC2 exploits the K^+ concentration gradient to move Cl^- out of neurons, thus maintaining the low intracellular Cl^- concentrations. By extruding Cl^- , KCC2 ensures that GABAergic signalling remains inhibitory (Kaila et al., 2014). In theoretical, pharmacological, as well as disease models manipulating KCC2 has been shown to influence Cl^- driving force (Barmashenko et al., 2011; Lee et al., 2011; Tang et al., 2015; Düsterwald et al., 2018).

The dogma of KCC2 determining Cl^- driving force has been recently challenged, with some scientists proposing that impermeant anions may also influence Cl^- concentrations and hence contribute to inhibitory signalling (Delpire and Staley, 2014; Glykys et al., 2014a, 2017). Speculatively, the electrostatic and osmotic effects of impermeant anions are thought to be able to displace Cl^- locally and shift concentrations within a neuron.

1.3.3. CHLORIDE MICRODOMAINS

Regions of distinct Cl^- concentrations within an individual dendrite ("Cl^- microdomains") have recently garnered attention in the field. Several studies have experimentally observed Cl^- microdomains in neurons (Vardi et al., 2000; Glykys et al., 2014a; Mohapatra et al., 2016; Rahmati et al., 2021), however what establishes these microdomains is still debated (Doyon et al., 2016).

One school of thought is that spatial differences in KCC2 density/strength along a dendrite are the cause of regions with higher/lower Cl^- concentration (Vardi et al., 2000; Szabadics et al., 2006; Zhang et al., 2013; Düsterwald et al., 2018). Another idea is that the distribution of impermeant anions are more responsible for establishing Cl^- microdomains (Glykys et al.,

2014a; Rahmati et al., 2021). As experimental methods to test these hypotheses are limited, uncertainty over the cause and maintenance of these microdomains still persist.

Further controversy exists regarding the functional significance of Cl^- microdomains that may arise from impermeant anions (Glykys et al., 2014b; Voipio et al., 2014). Some studies suggest that E_{Cl} is different as a result of impermeant anion driven Cl^- microdomains, they then postulate that GABAergic signalling at these regions should be different, driven by local differences in Cl- driving force (Rahmati et al., 2021). It should be noted however that impermeant anion driven differences in local Cl- driving force have not been demonstrated experimentally. Furthermore, how impermeant anions could actually affect inhibitory signalling and synaptic integration is not well understood.

1.3.4. NON-ISOPOTENTIAL DENDRITES AND INHIBITION

Impermeant anions are known to affect the membrane potential of neurons (Johnston and Wu, 1995). If impermeant anions were responsible for regions of altered Cl^- concentrations, then the membrane potential in these regions would be altered too – violating the assumption of isopotentiality (equal membrane potentials at all spatial locations) used in most neural models. The biophysics of non-isopotential neurons are poorly described and how inhibition may differ between non-isopotential and isopotential neurons is unknown.

I hypothesize that because membrane potential and E_{Cl} both shift due to impermeant anion charge differences, Cl^- driving force would be the same at each point along the neuron. Identical Cl^- driving forces should leave inhibition unaffected by local shifts in impermeant anion mean charge.

Answering this hypothesis is not possible with current experimental techniques. Mapping the precise subcellular distribution of impermeant anions whilst simultaneously gathering electrical signals has yet to be performed. Moreover redistribution of Cl^- can occur at rapid time scales along the dendrite (Doyon et al., 2011), and recording electrochemical signals along such narrow spatiotemporal scales is extremely challenging. Computational approaches to simulate neural physiology have been devised to overcome these experimental obstacles.

1.4. MODELLING DENDRITES

Several models have been proposed to predict neural functioning, each of which balance detail with abstraction. On one extreme of the spectrum, black-box models focus solely on the input, processing, and output (functional) aspects of neurons, and are useful when trying to predict neuronal spiking frequencies; however, these models are limited in describing effects related to neural structure and biophysics. On the other hand, detailed morphological models most accurately account for neuronal structure such as dendritic branching patterns, although, not all aspects of morphology are necessary for understanding the dynamics of a single neuron and efforts to incorporate detailed structure may be redundant and computationally expensive (Herz et al., 2006). Equivalent circuit multi-compartmental models strike a balance between detail and abstraction.

1.4.1. EQUIVALENT CIRCUIT MODELS AND CABLE THEORY

Equivalent circuit models liken the core electrical properties of neurons to electronic components in a circuit, with each component in the circuit representing an electrical property of the neuron (Hodgkin and Huxley, 1952). The semipermeable plasma membrane is modelled as a capacitor based on the dielectric properties of the membrane with ions accumulating on either side of it. The capacitance of most neuronal membranes is approximately $1\mu F/cm^2$ (Johnston and Wu, 1995).

Ion channels both permit and prevent ions crossing the membrane thus are modelled as variable conductances with permeabilities for specific ions. The conductances of these channels can vary with time and voltage, for instance at a synaptic junction when neurotransmitters bind causing post-synaptic ion channels to open allowing ionic flux.

Internal resistance (r_i) is the resistance to the flow of ions along the length of the dendrite due to the cytoplasm (and intraneuronal structures). The dendrite length (x) and cross-sectional area (A) are the determinants of the internal resistance.

Lastly, the driving force of a particular ion is modelled as a battery supplying a voltage equal to the difference between the membrane potential and the ionic reversal potential.

Cable Theory models segments of dendrite with electrical equivalent circuits composed of resistances and capacitances and therefore considers how an electrical signal attenuates as it propagates along a dendrite by ensuring that dendritic diameter, dendritic length, and intracellular axial resistance are accounted for. Schematic C below demonstrates how sequential equivalent circuits in series can be combined and modelled as a cable (Keener and Sneyd, 2009).

Using cable theory one can predict the passive cable properties of a dendrite, namely the membrane time and length constants. Tau($\boldsymbol{\tau}$), the membrane time constant, is defined as the time for the membrane voltage to reach 66% of the final membrane voltage. Tau is considered as the product between the membrane resistance (R_m), and the membrane capacitance (C_m). Tau is therefore solely predicted based on membrane specific determinants; consequently, one would not predict that impermeant anions fluxes alter Tau.

$$\tau = R_m \times C_m \quad \textbf{(Eq.1.5)}$$

Lamba (λ), the membrane space constant, is defined as the distance for the membrane voltage to reach 2/3 of its initial value. Lambda is determined by the membrane resistance (R_m), and internal resistance (R_i).

$$\lambda = \sqrt{\frac{R_m}{R_i}} \quad \textbf{(Eq.1.6)}$$

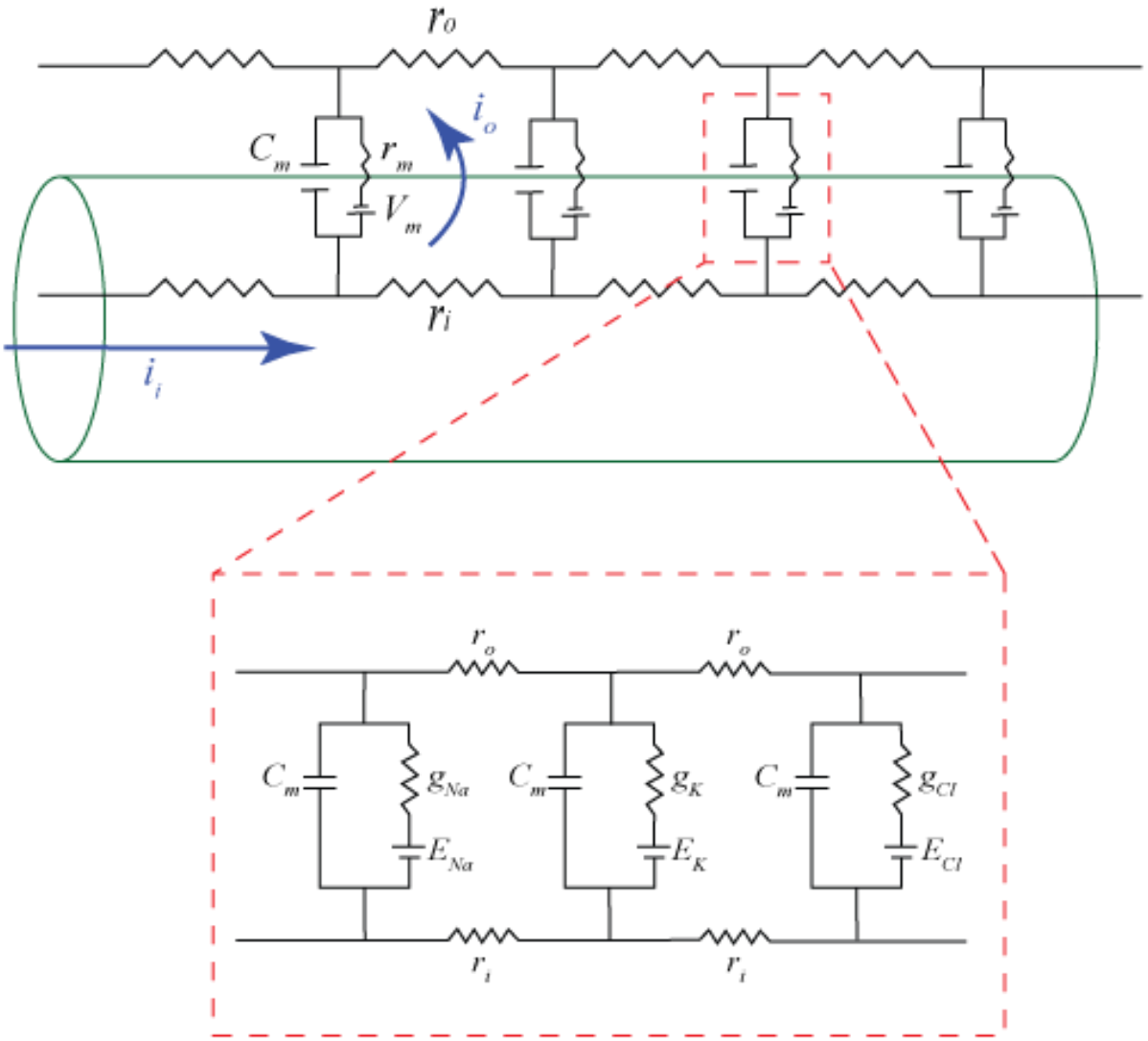

Fig. 1.3: Schematic depicting relationship between Cable Theory and equivalent circuit models. Dendrite acting as a cable (shown in green), with single electrical compartment modelled as an equivalent circuit (shown in red). C_m = Membrane capacitance, V_m = membrane voltage, r_m = membrane resistance, r_i = internal (axial) resistance, r_o = outward resistance , i_i = inward current, i_o = outward current, g_{na} = conductance for sodium, g_k = conductance for potassium, g_{cl} = conductance for chloride, E_{na} = Sodium reversal potential, E_k = potassium reversal potential, E_{cl} = chloride reversal potential.

1.4.2. Limitations of Cable Theory

Cable Theory typically considers the equilibrium potential of each ionic species as being constant along the length of the dendrite (Lopreore et al., 2008). Across large spatial scales the reversal potentials are relatively stable, thus the assumption that the transmembrane concentration gradient of each ion can be considered constant is relatively sound and provides similar predictions as can be gathered from experiment (Markram et al., 2015). In smaller

spaces however, there are rapid ionic fluxes within dendritic compartments, resulting in fluctuating ionic reversal potentials and membrane potentials (Brumback and Staley, 2008). Given steady state scenarios (where no dynamic ionic fluxes are occurring and reversal potentials are stable), cable theory would predict that given uniform, stable ionic conductances, neurons would have an equal membrane potential across the entire dendritic tree (i.e., be isopotential).

With this in mind a major limitation of cable theory and traditional equivalent circuit models is that they do not model impermeant anion concentration, mean charge, or distribution. It is not possible to model impermeant anions within a "charge sum" equivalent circuit framework, as they are unable to cross the cell membrane or move locally, as other permeant ion species can.

For these reasons using traditional computational tools based on equivalent circuits and the "charge sum" approach (such as the simulation software NEURON(Hines and Carnevale, 2001)) would be inappropriate. Studying the influence of impermeant anions on the electrical properties of neurons and investigating properties of non-isopotential dendrites, requires alternative more detailed electrodiffusion based models (Doyon et al., 2016).

1.4.3. ELECTRODIFFUSION BASED MODELS

Electrodiffusion, calculated with the Nernst-Plank equation, encompasses ionic movement resulting from electric fields (drift), as well as the movement of ions along their concentration gradients (diffusion) (Qian and Sejnowski, 1989; Savtchenko et al., 2017; Solbrå et al., 2018; Ellingsrud et al., 2020). Calculating the detailed interaction between the electric field and current allows for the simultaneous and precise determination of ionic concentrations at discrete moments in space and time - dynamic values not accessible in Cable Theory.

Qian and Sejnowski (1989) developed one of the first electrodiffusion based models and compared it to Cable Theory. They found that in settings of rapid ionic flux and thin dendritic processes significant errors were made in the predictions of membrane potentials and ion concentrations with Cable Theory relative to their one-dimensional electrodiffusion based model. Electrodiffusive phenomena are necessary to explain properties synaptic signalling and synaptic plasticity at regions of rapid ionic flux such as dendritic spines (Trappenberg, 2010).

Despite the promises of electrodiffusion based models, modelling in this highly dynamic, non-linear, and intricate fashion requires significant computational power. This hurdle prevented neuroscientists from adopting electrodiffusion models, however with the computational resources now publicly available, the computations involved can be performed in a few hours as opposed to days or weeks.

1.5. RATIONALE

Experimental techniques are currently unable to measure rapid chemical and electrical changes in dendrites that may occur with changes to impermeant anions. I propose creating a computational electrodiffusion based biophysical model incorporating the pump-leak mechanism and impermeant anions to simulate these aspects of neural electrophysiology (**objective A**). Using the biophysical model, I will investigate the role of impermeant anion quantity and mean charge (valence) on electrical and osmotic homeostasis in neurons. Specifically, I will evaluate whether spatial heterogeneities in impermeant anion distribution can influence the isopotentiality of neurons and whether this can explain the phenomenon of ionic microdomains (**objective B**). I will then compare the passive cable properties of non-isopotential and isopotential dendrites (**objective C**), as well as their potential impact on excitatory and inhibitory synaptic input (**objective D**). Lastly, I will probe whether impermeant anions influence synaptic integration/action potential generation (**objective E**). This thesis will advance our understanding of the electrical and computational effects impermeant anions may play in neurons.

1.6. AIMS AND OBJECTIVES

The overall aim of my thesis is to develope a biophysically accurate computational neuronal model incorporating electrodiffusion to investigate the influence of impermeant anions on the electrical and information processing properties of neurons.

The objectives are as follows:

A. Develope a multicompartmental neuronal model incorporating electrodiffusion to dynamically simulate changes in ion homeostasis, volume regulation and electrical activity.

B. Describe the effects of impermeant anions concentration, mean charge (valency), and distribution on the electrical properties of neurons.

i. Investigate the isopotential status of dendrites when impermeant anion mean charge is changed in different spatial compartments.

ii. Probe the relationship between impermeant anions and ionic microdomains.

C. Investigate whether impermeant anions alter passive cable properties dendrites

i. Compare membrane time and length constants between the biophysical multicompartmental dendrite and an isopotential dendrite in NEURON

ii. Assess whether regional changes in impermeant anion mean charge influences membrane time and length constants

D. Investigate how excitatory or inhibitory synaptic input is modified by the presence of impermeant anions.

E. Investigate how impermeant anions affect synaptic integration and neuronal output.

i. Compare the influence of impermeant anions and KCC2 conductance on synaptic integration.

2. METHODS

2.1. MULTICOMPARTMENT MORPHOLOGY

I simulated a neuron using a multicompartmental model within an extracellular bath (**Fig. 2.1**). The multicompartment model consisted of nine cylindrical compartments linearly arranged along the longitudinal axis. Ions were modelled to move between compartments and the surrounding extracellular environment (transmembrane), and between adjacent compartments (axial electrodiffusion). The extracellular environment was modelled as an "infinite bath" with fixed ion concentrations. Each compartment was modelled as a cylinder with a diameter of 1µm and length of 20µm.

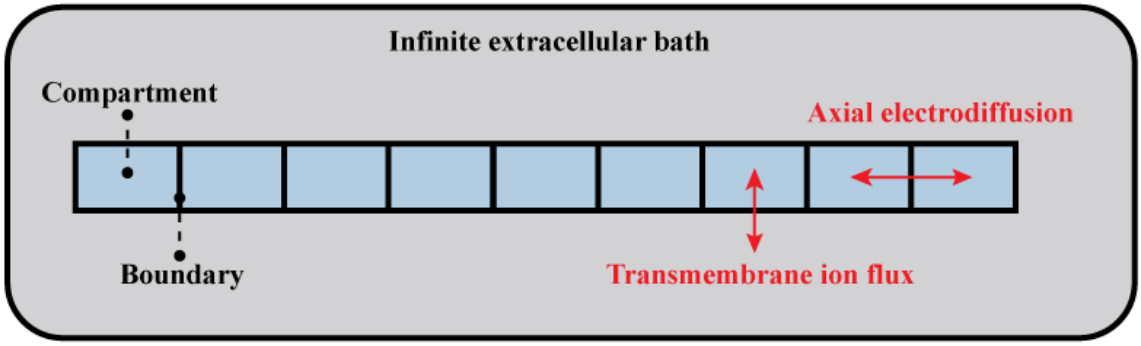

Fig. 2.1: Multicompartment model within an infinite bath. In this bird's eye view, compartments are displayed as rectangles shaded as blue. Nine compartments are linearly arranged to form the multicompartment model. The extracellular environment is modelled as an infinite bath with a fixed ion concentration. Ionic motion is possible both across the membrane (between the intracellular and extracellular space), and between compartments via electrodiffusion.

I made two assumptions regarding the morphology: firstly, that the compartment swells only in the radial dimension (therefore not affecting the electrodiffusion equations that are length dependant); secondly; that the surface area of the compartment is fixed i.e., as volume changes I consider the cell to wrinkle or become less wrinkled, shown in **Fig 2.2 Method A**. This method is preferred over a scaled surface area (**Fig 2.2 Method B**) for simplicity as this allows membrane capacitance and ion conductances, that are surface area dependant, to remain constant. For the final set of experiments, I added a soma (length = 40µm; diameter = 2µm) onto compartment 1.

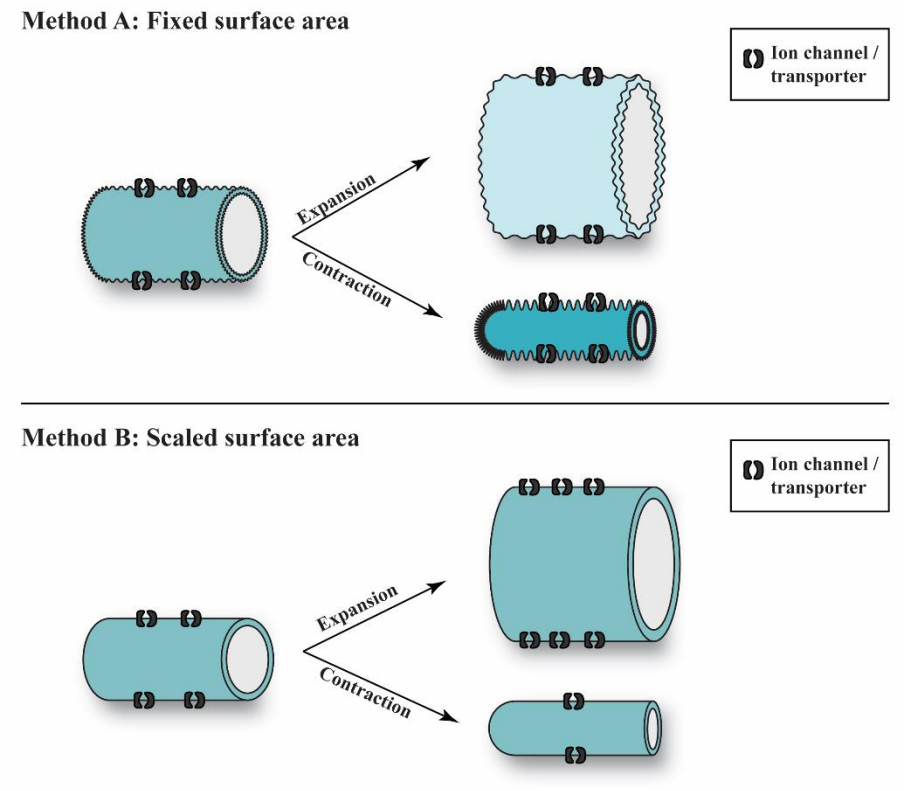

Fig. 2.2: Single compartment morphology and method of radial volume change with fixed versus scaled surface area. Each compartment was modelled as a cylinder with a diameter of 1µm and a length of 20µm. Volume change occurred along the radial axis. I employed Method A where the total surface area remains constant despite volume changing, this can be imagined as the cell becoming more or less wrinkled with volume contraction and expansion. This method was preferred to scaling the surface area (Method B) as the membrane capacitance and ion channels/transporters conductance would scale with the surface area thus changing the electrical properties of the cell.

2.2. TRANSMEMBRANE ION FLUX

2.2.1. ION CHANNELS

Ionic flow between the internal and external environment were permitted via leak, sodium-potassium ATPase, and KCC2 transporters (**Fig. 2.3**). Hodgkin Huxley channels were added in the final set of experiments to model action potential generation occurring in the somatic compartment. The direction of ionic flow was determined by respective osmolar and electrical gradients.

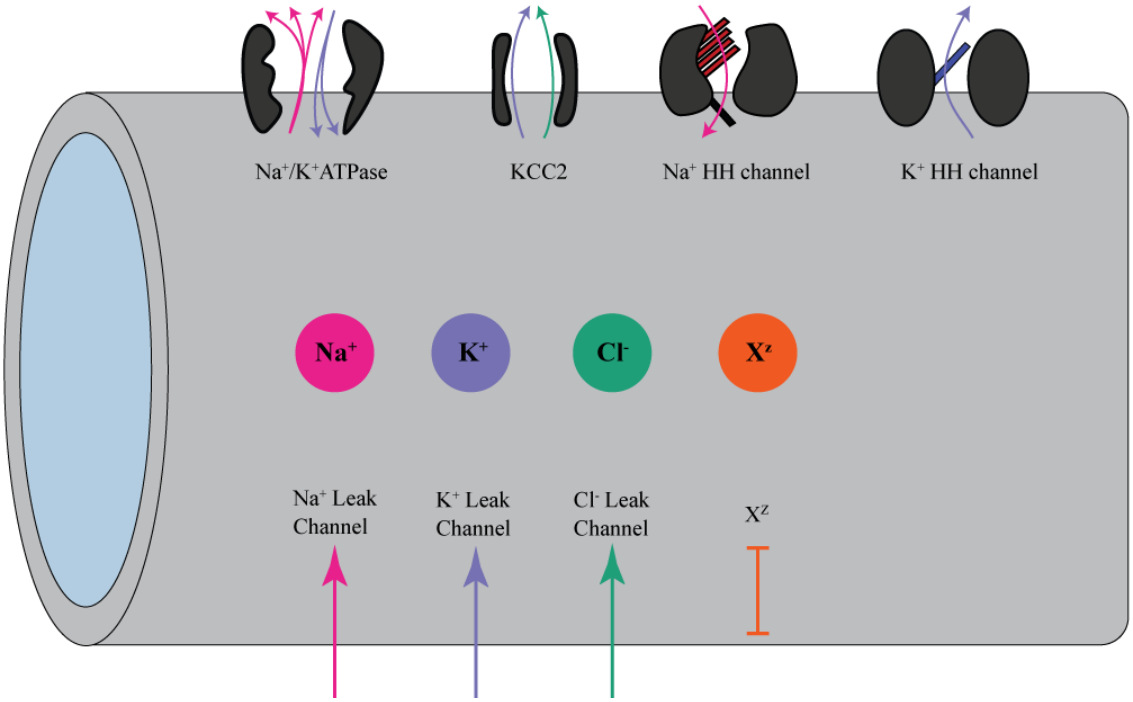

Fig. 2.3: Methods of transmembrane ion flux in a single compartment. Permeant ions (Na^+; K^+; Cl^-) can traverse the cell membrane via leak channels which facilitate diffusion ion diffusion between the internal and external environments. Impermeant anions (X^z) are trapped within the intracellular compartment. In all compartments the Na^+/ K^+ ATPase pumps 3 Na^+ ions out the compartment in exchange for 2 K^+, while the KCC2 transporter moves K^+ and Cl^- out the cell in equal amounts. In the final set of experiments Hodgkin Huxley (HH) Na^+ and K^+ channels were added to facilitate action potential firing in the somatic compartment.

	Value	Description
Constants		
F	96485.33 C/mol	Faraday Constant
R	8.31446 J/(K·mol)	Universal gas constant
T	310.15 K	Absolute temperature (37C)
Parameters		
dt	10^{-6} s	Simulation time step
C_m	$2x10^{-4}$ F/dm^2	Membrane capacitance (Qian and Sejnowski, 1989)
g_{Na}	20 µS/cm^2	Na^+ leak conductance (Kager et al., 2000)
g_K	70 µS/cm^2	K^+ leak conductance (Kager et al., 2000)
g_{Cl}	20 µS/cm^2	Cl^- leak conductance (Kager et al., 2000)
P	0.1 C/(dm^2/s)	Na/K-ATPase pump rate (fitted)
$[Na^+]_o$	145mM	Extracellular Na^+ concentration
$[K^+]_o$	3.5mM	Extracellular K^+ concentration
$[Cl^-]_o$	119mM	Extracellular Cl^- concentration
$[X^-]_o$	29.5mM	Extracellular Impermeant anion concentration (Raimondo et al., 2015)
v_w	0.018 dm^3/mol	Partial molar volume of water (Hernández and Cristina, 1998)
p_w	0.018 dm/s	Osmotic permeability (Hernández and Cristina, 1998)
D_{Na}	6.65 x 10^{-8} dm^2/s	Na^+ diffusion constant, 50% of value used in (Hille, 2001; Düsterwald et al., 2018) based on comparison of passive signalling in NEURON
D_K	9.85 x 10^{-8} dm^2/s	K^+ diffusion constant, 50% of value used in (Hille, 2001; Düsterwald et al., 2018) based on comparison of passive signalling in NEURON
D_{Cl}	1.015 x 10^{-7}dm^2/s	Cl^- diffusion constant, 50% of value used in (Hille, 2001; Düsterwald et al., 2018) based on comparison of passive signalling in NEURON
I_{ext}	0.1 nA	External input current
α_{GABA}	0.5 ms^{-1}mM	Forward rate constant for GABA binding (Destexhe et al., 1993)
β_{GABA}	0.1 ms^{-1}	Reverse rate constant for GABA binding (Destexhe et al., 1993)

α_{NMDA}	2 $ms^{-1}mM$	Forward rate constant for NMDA binding (Destexhe et al., 1993)
β_{NMDA}	1 ms^{-1}	Reverse rate constant for NMDA binding (Destexhe et al., 1993)
Hodgkin-Huxley (HH) parameters		All sourced from (H Chiel and Gill, 2022)
$\bar{g}_{Na}$	120 mS/cm^2	Maximal HH Na^+ conductance
$\bar{g}_{K}$	36 mS/cm^2	Maximal HH K^+ conductance
V_1	100 mV·ms	HH parameter 1
V_2	-55 mV	HH parameter 2
V_3	10 mV	HH parameter 3
V_4	0.125 ms^{-1}	HH parameter 4
V_5	-65 mV	HH parameter 5
V_6	80 mV	HH parameter 6
V_7	10 mV·ms	HH parameter 7
V_8	-40 mV	HH parameter 8
V_9	10 mV	HH parameter 9
V_{10}	4 ms^{-1}	HH parameter 10
V_{11}	-65 mV	HH parameter 11
V_{12}	18 mV	HH parameter 12
V_{13}	0.07 ms^{-1}	HH parameter 13
V_{14}	-65 mV	HH parameter 14
V_{15}	20 mV	HH parameter 15
V_{16}	1 ms	HH parameter 16
V_{17}	-35 mV	HH parameter 17
V_{18}	10 mV	HH parameter 18
Variables		
$[Na^+]_i$	14 mM	Intracellular Na^+ concentration
$[K^+]_i$	122.9 mM	Intracellular K^+ concentration
$[Cl^-]_i$	5.2 mM	Intracellular Cl^- concentration
$[X^-]_i$	154.9mM	Intracellular impermeant anion concentration
z	-0.85	Intracellular impermeant anion mean charge (based on (Lodish et al., 2009; Raimondo et al., 2015)
g_{KCC2}	20 $\mu S/cm^2$	KCC2 conductance (Doyon et al., 2016)

$GABA_{Max}$	1 mM	Saturating concentration of GABA molecules
$NMDA_{Max}$	1 mM	Saturating concentration of NMDA molecules
g_{GABA}	1 nS	Conductance of GABAergic synapses
g_{NMDA}	1 nS	Conductance of glutamatergic synapses
n	0	Proportion of voltage gated HH K^+ channels open
m	0	Proportion of voltage gated HH Na^+ m-gates open
h	1	Proportion of voltage gated HH Na^+ m-gates open
α_n	0	Rate of voltage gated HH K^+ channels opening
β_n	0	Rate of voltage gated HH K^+ channels closing
α_m	0	Rate of voltage gated HH Na^+ m-gate opening
β_m	0	Rate of voltage gated HH Na^+ m-gate closing
α_h	0	Rate of voltage gated HH N^+ h-gate opening
β_h	0	Rate of voltage gated HH Na^+ h-gate closing

Fig. 2.4: Table of constants and parameters

2.2.2. MEMBRANE POTENTIAL

Membrane potentials refer to the voltage differences between the inside of a compartment and the extracellular environment. All membrane potentials are denoted with a subscript "*m*".
The membrane potential (V_m) was calculated using the 'Charge Difference' approach used by Fraser and Huang(2004)

$$V_m = \frac{F \times w([\mathrm{Na}^+]_i + [K^+]_i - [Cl^-]_i + z[X^z]_i)}{C_m SA}$$

This formula is a derivation of the capacitance equation ($V = q/C_m$). The numerator of the equation sums the difference between intracellular cation and anion concentrations, which is multiplied by the volume to get a molar quantity. Multiplication by Faradays constants (F) converts the molar quantity to coulombs. The membrane capacitance (C_m) is calculated per unit surface area; thus, I multiply by surface area to get the total membrane capacitance.

2.2.3. IONIC REVERSAL POTENTIAL AND DRIVING FORCE

Ionic reversal potential across the membrane (E_{ion}) is defined as the membrane potential at which there is no net flux of a particular ion between the internal and the extracellular environment. The derivation of this equation is discussed in the introduction.

$$E_{ion} = \frac{RT}{zF} \ln\left(\frac{[ion]_o}{[ion]_i}\right)$$

At an ion's resting potential, the electrical forces balance the diffusive forces across the membrane and hence there is no net ion flux. In neurons however the membrane potential is rarely at ionic reversal potential and thus there is a potential difference for the ionic flux – defined as the ionic driving force (DF_{ion}).

$$DF_{\text{ion}} = V_m - E_{ion}$$

2.2.4. LEAK CHANNELS

Leak channels permit bidirectional motion of ions across the membrane. A cell membrane will have multiple leak channels; however, I simplified this by modelling a single leak current for each ion. I calculated leak current using a modified form of ohms law, where the channel conductance (inverse of resistance) is multiplied by the ionic driving force.

$$I_{leak} = g_{ion}(v_m - E_{ion})$$

Ionic conductances(g_{na}, g_k, and g_{cl}) were set to those in Düsterwald et al. (2018), which were obtained from conductances used in the similar models on ModelDB(McDougal et al., 2017) and ion channel genealogy (Podlaski et al., 2017).

2.2.5. NA^+/K^+ ATPASE

The Na^+/K^+-ATPase utilizes the energy from the hydrolysis of ATP to shift two potassium ions into the cell in exchange for three sodium ions which move extracellularly. This process is critical for establishing a negative resting membrane potential and ensuring volume control. I modelled the flux through the ATPase (J_p) based on the formula employed by Keener and Sneyd (2009):

$$J_p = P \cdot \left(\frac{[Na]_i}{[Na]_o}\right)^3$$

The flux rate (J_p) is a function of the pump constant (P) and the sodium (Na^+) concentration ratio between the internal and external environment. The pump constant was set to 0.1

C/(dm^2.s) based on a fitted curve establishing actual values of sodium concentrations and membrane potentials(Düsterwald et al., 2018). For all simulations, to model the situation where no additional energy was used by the system following any particular manipulation, I kept J_p constant by using the initial sodium concentration (as opposed to updating it at each time step).

2.2.6. KCC2 COTRANSPORTERS

The type 2 K-Cl cotransporter (KCC2) is an essential regulator of chloride ion concentration. It utilizes the transmembrane gradient of both potassium and chloride to move these ions bidirectionally across the cell membrane. Flux through the KCC2 transporter was modelled using the formula suggested by Doyon et al. (2011, 2016), where the conductance of KCC2 was also provided as a fixed value (20 µS/cm^2)

$$J_{KCC2} = g_{KCC2} \cdot (E_k - E_{Cl})$$

2.2.7. NET TRANSMEMBRANE ION FLUX EQUATIONS

The rates of change for each ion concentration across the membrane was based on the sum of the leak, ATPase and KCC2 fluxes for the respective ions. The conductance of each ion channel is given as Siemens/dm^2 of the cell membrane; therefore, membrane surface area (SA) is included in this calculation. This sum is divided by Faraday's constant to convert the charge to moles and is divided by the volume to get a concentration change (*d*[Ion]) per unit time (*dt*). A forward Euler method was used to update variables at each time step.

$$\frac{d[Na^+]_i}{dt} = \frac{-SA}{F \cdot w} \cdot (g_{Na}(v_m - E_{Na}) + 3J_p)$$

$$\frac{d[K^+]_i}{dt} = \frac{-SA}{F \cdot w} \cdot (g_K(v_m - E_K) - 2J_p - J_{KCC2})$$

$$\frac{d[Cl^-]_i}{dt} = \frac{SA}{F \cdot w} \cdot (g_{Cl}(v_m - E_{Cl}) + J_{KCC2})$$

2.3. AXIAL ION FLUX

2.3.1. ELECTRODIFFUSION

In addition to transmembrane motion, ionic species can move in the axial plane. For simplicity this is regarded as a single dimension along the length of the axon or dendrite. Like transmembrane motion, chemical and electrical forces drive ionic movement through the cytoplasm; however, unlike movement across the membrane, there are no channels that permit ionic movement at discrete spatial points. Instead, ions are assumed to be able to move across the entire surface area.

To model the axial flux of ions the Nernst-Planck Equation (NPE) was used (Qian and Sejnowski, 1989). This equation calculates the flux of ions based on diffusion (chemical forces) and drift (electrical forces) and has been shown to be more accurate than either of these forces alone especially in small structures such as dendrites. The NPE calculates the flux density (J) for ion C as follows:

$$J = -D\frac{zF^2}{RT}[C]\frac{dV_m}{dx} - DF\frac{d[C]}{dx}$$

In the NPE, the first term represents the ionic drift, where the diffusion constant for a particular ion (D) is multiplied by the voltage difference (dV_m) over the axial length (dx) between two regions. The second term based on concentration differences (d[C])represents the diffusion of the ion diffusion constant for that ion (D) is multiplied by its mean charge (z). The distance between the midpoints between adjacent compartments was used as the dx term. The negative sign in both terms indicate that the direction of current flow is opposite to the concentration/voltage gradients.

The flux for each ion was calculated between adjacent compartments i to $i + 1$, with flux units of mol/(s.dm^2), using the equation below. To determine the molar concentration of ions the flux was multiplied by the shared surface area and divided by the compartment volume to determine the flux in terms of molar concentration (M/s). A forward Euler method was used to update variables at each timestep.

$$C_{i \to i+1} = -\frac{dt}{l_i}D\left(\frac{zF}{RT}\frac{([C]_i + [C]_{i+1})}{2}\frac{(V_{m_i} - V_{m_{i+1}})}{dx} + \frac{([C]_i - [C]_{i+1})}{dx}\right)$$

2.3.2. BOUNDARY POTENTIALS AND AXIAL DRIVING FORCE

Boundary potentials refers to the voltage differences that occur across the boundary between compartments such that the boundary acts as a theoretical membrane. All boundary potentials are denoted with a subscript "*b*".

The boundary potential (V_b) between two compartments (compartment A and B) was defined as the difference between the membrane potentials of the 2 compartments.

$$V_b = V_{m\ compartment\ A} - V_{m\ compartment\ B}$$

Boundary reversal potentials for a particular ion ($E_{b\ ion}$) were calculated in a similar way to ionic reversal potentials across the membrane however the ionic concentrations between the two compartments, rather than the internal and external environments, are used in the calculation.

$$E_{b\ ion} = \frac{RT}{zF} \ln\left(\frac{[ion]_{compartment\ A}}{[ion]_{compartment\ B}}\right)$$

The boundary driving force for an ion ($DF_{b\ ion}$) is therefore defined as the difference between the boundary potential and the boundary ionic reversal potential for that ion.

$$DF_{b\ ion} = V_b - E_{b\ ion}$$

2.4. IMPERMEANT ANION MANIPULATION

2.4.1. CHANGING IMPERMEANT ANION QUANTITY

When altering impermeant anion quantities ("X-flux") in a compartment I add absolute moles of impermeant anions to the compartment (as opposed to adding molar concentration). I used a flux rate of 10^{-15} mol/s which was multiplied by the time step and divided by the volume at that timestep to calculate the change in concentration of impermeants in the compartment.

2.4.2. CHANGING IMPERMEANT ANION CHARGE

In several simulations I changed the mean charge of impermeant anions ("z-flux") away from the default (z = -0.85). This was performed by calculating the difference between the desired final mean charge and the initial default mean charge. This value was divided by the time step to get the incremental value by which to change the mean time at each iteration.

$$\frac{dz}{dt} = \frac{(z_{final} - z_{initial})}{duration\ of\ flux}$$

2.5. COMPARTMENT VOLUME AND SURFACE AREA

I updated the volume of each compartment at every time step to ensure osmotic balance. Each compartment was modelled as a cylinder with volume (w) calculated as:

$$w = \pi r^2 l$$

Radius is denoted by r, and cylinder length by l. I imagined the cylinder to have open ends (allowing for diffusion) so surface area (SA) was calculated as:

$$SA = 2\pi r l$$

Surface area was assumed to be constant for the duration of the simulation, approximating a compartment that wrinkles or unwrinkles as the volume swells. The implication of this assumption is that ion channel and pump conductances are not constantly rescaled by fluctuating surface areas.

Compartment volume was updated at each time point as this has significant implications for the voltage equations. Volume updates were modelled using the equation below (Hernández and Cristina, 1998):

$$\frac{dw}{dt} = v_w \cdot p_w \cdot SA \cdot (\Pi_i - \Pi_o)$$

In this equation, *dw* is the volume change which is equal to the product of the partial molar volume of water (v_w), the osmotic permeability of a biological membrane(p_w), and the surface area (*SA*). This factor is then multiplied by the difference between the internal and external osmolarities (Π).

I do not model the volume changes that could result from cytoplasmic matrix constituents (impermeant anions) moving between compartments.

2.5.1. VOLUME NORMALIZATION

Volume changes occur because of the difference between internal and external osmotic composition. Changes to impermeant anion average charge also affect compartment volumes. To understand the impact of changing impermeant anion average charges on passive and active dendritic signalling properties, separate from induced volume changes, in a subset of simulations compartment volumes were "clamped" or normalized.

To normalize the volume of a single compartment, I fixed the osmolarity to the average osmolarity of the other compartments (excluding the soma). To do this I firstly calculated the average osmolarity of all compartments (Π_{mean}), and secondly adjusted impermeant anion concentration $[X]_i$ at each time step to achieve the desired osmolarity. This procedure is based on the findings by Dusterwald et al(2018) showing impermeant anion concentration sets compartment volume without influencing steady state ion concentrations for further details see **Appendix 6.1**.

$$\Pi_{mean} = \frac{\sum_j^n \Pi_j}{n}$$

$$[X]_i = \Pi_{mean} - [Na^+]_i - [K^+]_i - [Cl^-]_i$$

2.6. PASSIVE CABLE PROPERTIES

2.6.1. COMPARISON WITH NEURON SIMULATION ENVIRONMENT

I validated our electrodiffusion based model with other models in the field, as well as with an equivalent circuit model using the simulation software NEURON(Hines and Carnevale, 2001), by comparing membrane time and space constants after a current was injected. In NEURON I assembled nine compartments (lengths: 20µm; diameter: 1µm) linearly, each with identical membrane capacitances (2µF/cm^2) and total passive/leak conductances (0.00011 S/cm^2). Resting membrane potential was set to -72.6mV, and an axial resistance of 200 Ω-cm was chosen based on values used in similar dendritic models found on ModelDB (Zhou, 2005; Eyal et al., 2016, 2018; Deitcher et al., 2017). Data from NEURON was extracted and plotted using Matplotlib in an identical manner to the data arising from the electrodiffusion model. In both models I pulsed a +0.1nA current into compartment 9.

To simulate excitatory current in the biophysical model I determined the amount of charge (coulombs) would be required for a specific duration of time using the formula (I = Q/t). This value was converted to moles then divided by the time step (10^{-6}s) and compartment volume to achieve the desired concentration to be added to the compartment at every iteration of the simulation for the duration of the current pulse. I added this value to intracellular Na^+ (for excitatory currents) or intracellular Cl^- concentration (for inhibitory currents).

2.6.2. MEMBRANE TIME AND SPACE CONSTANTS

To calculate the membrane time constant (Tau/τ), I fitted a single exponential curve of the membrane potential between the end of the current pulse and the end of the simulation. Tau was the time taken from the end of the current pulse for the membrane potential to decay to 63% of the final resting value along the curve.

The length constant (Lambda/λ) was calculated similarly. A single exponential curve was fitted for membrane potential versus distance between two points: where the current was inputted, and the furthest point along the multicompartment neuron. Lambda was the distance at which the membrane potential had decayed to 63% of the membrane potential at the furthest point along the fitted curve.

2.7. SYNAPTIC INTEGRATION

2.7.1. SYNAPTIC MODELLING

I simulated synapses on our biophysical multicompartment model to assess how impermeant anions affect synaptic integration. Excitatory (NMDA/Glutamatergic) and inhibitory (GABA/GABAergic) synapses were modelled using the kinetic binding model described by Destexhe et al., (1993, n.d.):

$$R + [NT] \overset{\alpha,\beta}{\Leftrightarrow} R.[NT]$$

A synaptic input begins with the release of a neurotransmitter ([NT]) which attach to unbound receptors (R), forming a transmitter-receptor complexes (R·[NT]). The rate of the neurotransmitter bindings is given as α, and the rate of unbinding as β. The α and β values vary according to neurotransmitter-receptor type. The strength of the current due to the synapse is dependent on the amount of neurotransmitter binding (r - calculated as a ratio of bound to total receptors).

$$r = \frac{Bound\ receptors}{Total\ receptors} = \frac{R.[NT]}{R + R.[NT]}$$

Before the synaptic event it is assumed that the ratio is equal to zero as there are no bound receptors. During the synaptic event r can be calculated with the formula below:

$$\frac{dr}{dt} = \alpha\,[T](1 - r) - \beta r$$

The bound receptor ratio change is the difference between the number of unbound receptors that are being bound minus the number of bound receptors moving to the unbound state. Using this formula, I can calculate the ratio of bound neurotransmitter at a given time point which is required to determine the current moving through the channel.

$$I_{NMDA} = -g_{NMDA}.r_t.(V_m - E_{Na})$$

$$I_{GABA_{Cl}} = g_{GABA}.r_t.(V_m - E_{Cl}) \cdot \left(\frac{4}{5}\right)$$

Current through the glutamatergic channels (I_{NMDA}) is equal to the conductance of the channel (g_{NMDA}) multiplied by the amount of receptor bound at a particular time point (r_t) and the driving force for sodium. The negative sign indicates the inward current due to positive ions moving into the cell. Current through GABAergic channels (I_{GABA}) consists of Cl^- flux (80%) and HCO_3^- flux (20%). As only Cl^- is modelled in our simulations I multiplied I_{GABA} by 80% and use E_{Cl} instead of E_{GABA} to derive the proportion of the GABAergic current due to Cl^-.

Using I_{NMDA} and I_{GABA} , one can calculate the molar quantity of Na^+ or Cl^- as current is charge divided by time. Charge in Coulombs was converted to mole by dividing through by Faraday's constant. I therefore divided by the compartment volume to determine the concentration of Na^+ or Cl^- that is entered the compartment at a particular time step.

2.7.2. ACTION POTENTIAL MODELLING

To model action potentials, I used Hodgkin-Huxley equations (Hodgkin and Huxley, 1952) with default parameter values ($V_1 – V_{18}$) obtained from NeuroWiki (H Chiel and Gill, 2022). Hodgkin & Huxley (HH) accurately model action potentials by plotting the dynamics of voltage gated Na^+ and K^+ channels that are activated once a threshold membrane potential (-50mV) is reached.

Current going through HH K^+ channels is given by:

$$I_{k_{HH}} = g_{k_{HH}}(V_m - E_k)$$

The potassium conductance through the Hodgkin Huxley channel ($g_{k_{HH}}$) is modelled by:

$$g_{k_{HH}} = \bar{g}_K n^4$$

The maximum K^+ conductance is represented by $\bar{g}_K$, while *n* can be thought of as the proportion of voltage gated K^+ channels open. The rate of change of *n* is a function of time, voltage, and intrinsic channel properties given by the equation below:

$$\frac{dn}{dt} = \alpha_n(1 - n) - \beta_n n$$

The rate of *n* change is the difference between the rate (α_n) of closed channels (1-*n*) that are opening and the rate (β_n) of open channels that are closing (*n*). Both α_n and β_n are dependent on the membrane potential and are given by the equations:

$$\alpha_n(V_m) = \frac{-(V_m - V_2)}{V_1\left(e^{\frac{-(V_m - V_2)}{V_3}} - 1\right)}$$

$$\beta_n(V_m) = V_4 e^{\frac{-(V_m - V_5)}{V_6}}$$

Current through the Na^+ - HH channel ($I_{Na_{HH}}$) is calculated similarly to the K^+ HH-channel:

$$I_{Na_{HH}} = g_{Na_{HH}}(V_m - E_{Na})$$

Unlike the voltage gated K^+ channel, the conductance of the Na^+ channel depends on the opening of two types of gates (the probability of each being open is symbolised by *m* and *h*).

The *m* gate is closed at resting membrane potential and opens rapidly when the threshold potential is reached, conversely, the *h* gate is open at resting potential and is triggered to close slowly once the threshold is reached. The interaction between the two gates scales the maximal Na conductance ($\bar{g}_{Na}$) to give the Hodgkin-Huxley Na+ conductance ($g_{Na_{HH}}$):

$$g_{Na_{HH}} = \bar{g}_{Na} m^3 h$$

Both the *m* and *h* gate are modelled in the same way the K+ channel was modelled by determining the forward (α) and reverse rate (β) of channel opening which is a function of both time and membrane potential. The *m* gate is modelled with the three equations below where $V_{7\text{-}12}$ are constants:

$$\frac{dm}{dt} = \alpha_m(1 - m) - \beta_m m$$

$$\alpha_m(V_m) = \frac{-(V_m - V_8)}{V_7\left(e^{\frac{-(V_m - V_8)}{V_9}} - 1\right)}$$

$$\beta_m(V_m) = V_{10} e^{\frac{-(V_m - V_{11})}{V_{12}}}$$

The *h* gate is modelled in a similarly with $V_{13\text{-}18}$ constants reflecting the internal properties of the gate.

$$\frac{dh}{dt} = \alpha_h(1 - h) - \beta_h h$$

$$\alpha_h(V_m) = V_{13} e^{\frac{-(V_m - V_{14})}{V_{15}}}$$

$$\beta_h(V_m) = \frac{1}{V_{16}\left(e^{\frac{-(V_m - V_{17})}{V_{18}}} + 1\right)}$$

2.8. COMPUTATIONAL STRATEGY

The simulation code was developed in the Python 3.10 using the PyCharm Integrated Development Environment. A forward Euler approach was deployed to solve the various differential equations described in the methods above. The broad processes occurring a simulation are summarized in **Fig 2.6.**

Simulation settings and initialization parameters are saved in a separate settings text file, while the state of simulation variables and parameters are saved in an HDF5 (high-density file) at specified intervals. Simulation results were plotted in Jupyter Notebooks by reading HDF5 file results. Further information regarding the class structure used for the simulation code, as well as details about the HDF5 simulation state method can be found in Appendix 6.1 and 6.2. Simulation code can be accessed from github: https://github.com/Eran707/msc_code_repo

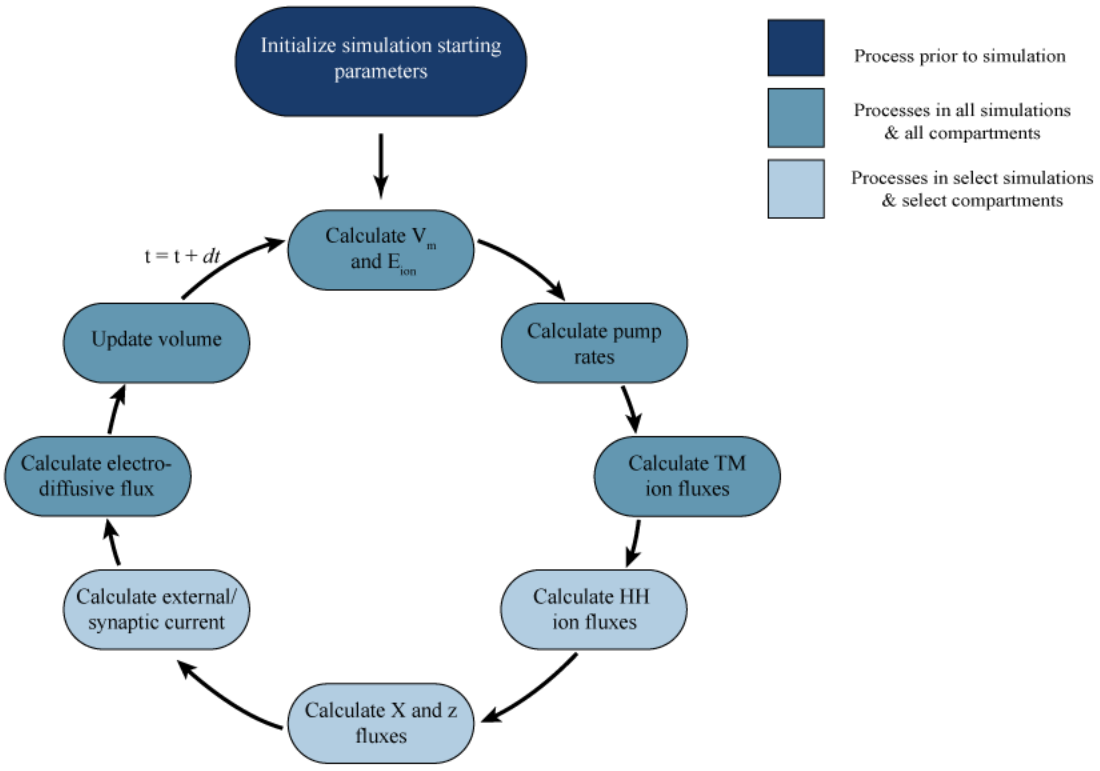

Fig. 2.6: Flow chart of operations occurring in a single simulation. TM is the transmembrane ion fluxes (flux between the external environment and the compartment). HH is the flux through voltage gated Hodgkin-Huxley channels. "X flux" refers to the manipulation of impermeant anion concentration, while "z-change" refers to the manipulation of impermeant anion average charge.

3. RESULTS

3.1. MODIFYING THE ABSOLUTE AMOUNT OF IMPERMEANT ANIONS IN A COMPARTMENT

3.1.1 IMPERMEANT ANION QUANTITY SETS LOCAL COMPARTMENT VOLUME WITHOUT AFFECTING MEMBRANE POTENTIAL OR IONIC DRIVING FORCES

I first set out to determine the effect of increasing the amount of impermeant anions (without changing impermeant mean charge) in a single compartment of my nine compartment multicompartment model. The quantity of impermeant anions in compartment number 8 (Comp8) was increased at a fixed rate of $1x10^{-15}$ mol/s between 100 and 150s ("X-Flux"), whilst the mean charge of impermeant anions was the same as those already in the compartment (z = - 0.85) (**Fig 3.1A**).

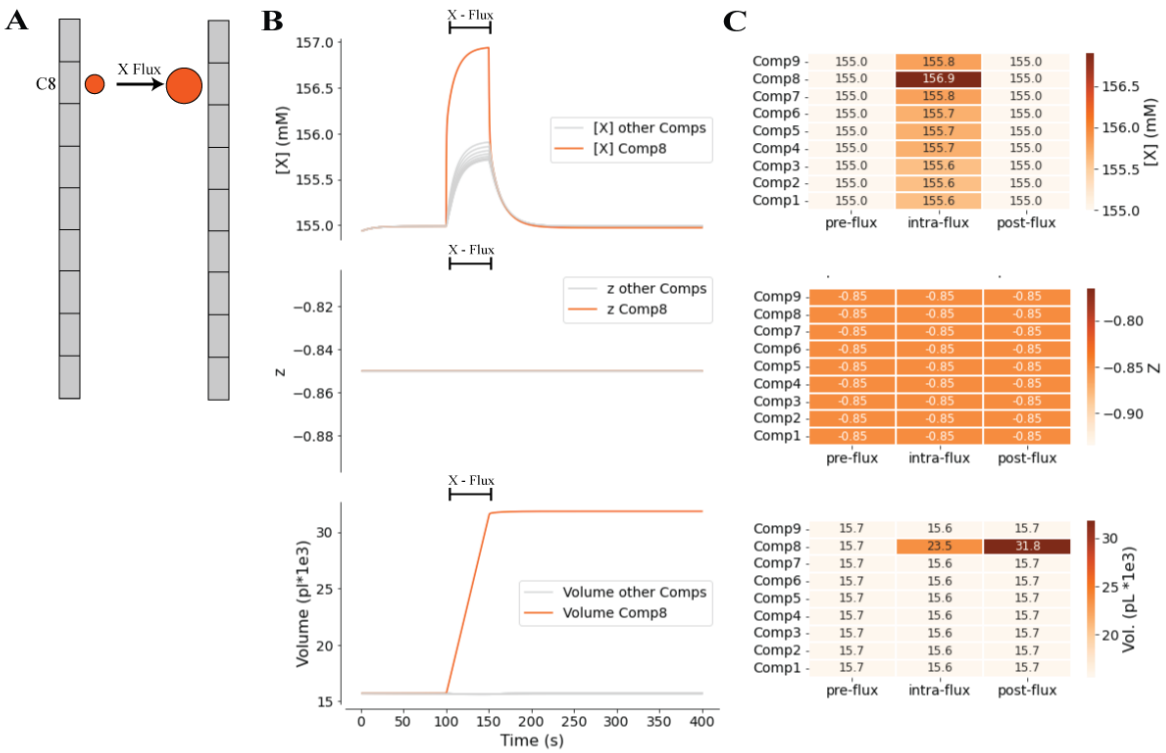

Fig. 3.1A: Impermeant anion quantity sets local compartment volume.
A: Simulation design. Using a 9-compartment model, I increased impermeant anions (rate: 10^{-15} mol/s; mean charge: -0.85) into Comp8 between 100 and 150s in a 500s simulation.
B: Line graphs showing impermeant anion concentration, impermeant anion mean charge and compartment volume in Comp8 (orange) and other compartments (grey) for 400s.
C: Heat maps quantifying impermeant anion concentration (mM), impermeant anion mean charge and compartment volume(pl*10^{-3}) at 3 time points: pre-flux (99.99s); intra-flux (125s); post-flux (500s).

A $5x10^{-14}$ mol increase in impermeant anions resulted in a temporary impermeant anion concentration increase of approximately 2mM during the flux period. The concentration of

impermeant anions in Comp8 returned to pre-flux baseline due to the volume of Comp8 more than doubling (pre-flux: 15.7 x 10^{-3} pl; post-flux: 31.8 x 10^{-3} pl) to accommodate the increase in impermeant anion load. Permanent volume shift occurred only in Comp8 whilst the volume in other compartments remained identical.

During the addition of impermeant anions ("X-Flux") I assessed the changes to other ionic species (Cl^-; Na^+; K^+) (**Fig 3.1B**). During the X-Flux, transient changes in ionic composition occurred; in all compartments however, ion concentrations returned to their pre-flux baseline values at steady state. Considering volume changes in Comp8 occurred (**Fig 3.1A**), a net change in absolute number of mol of other ionic species in that compartment must have resulted from the impermeant flux such that the concentration levels remained uniform.

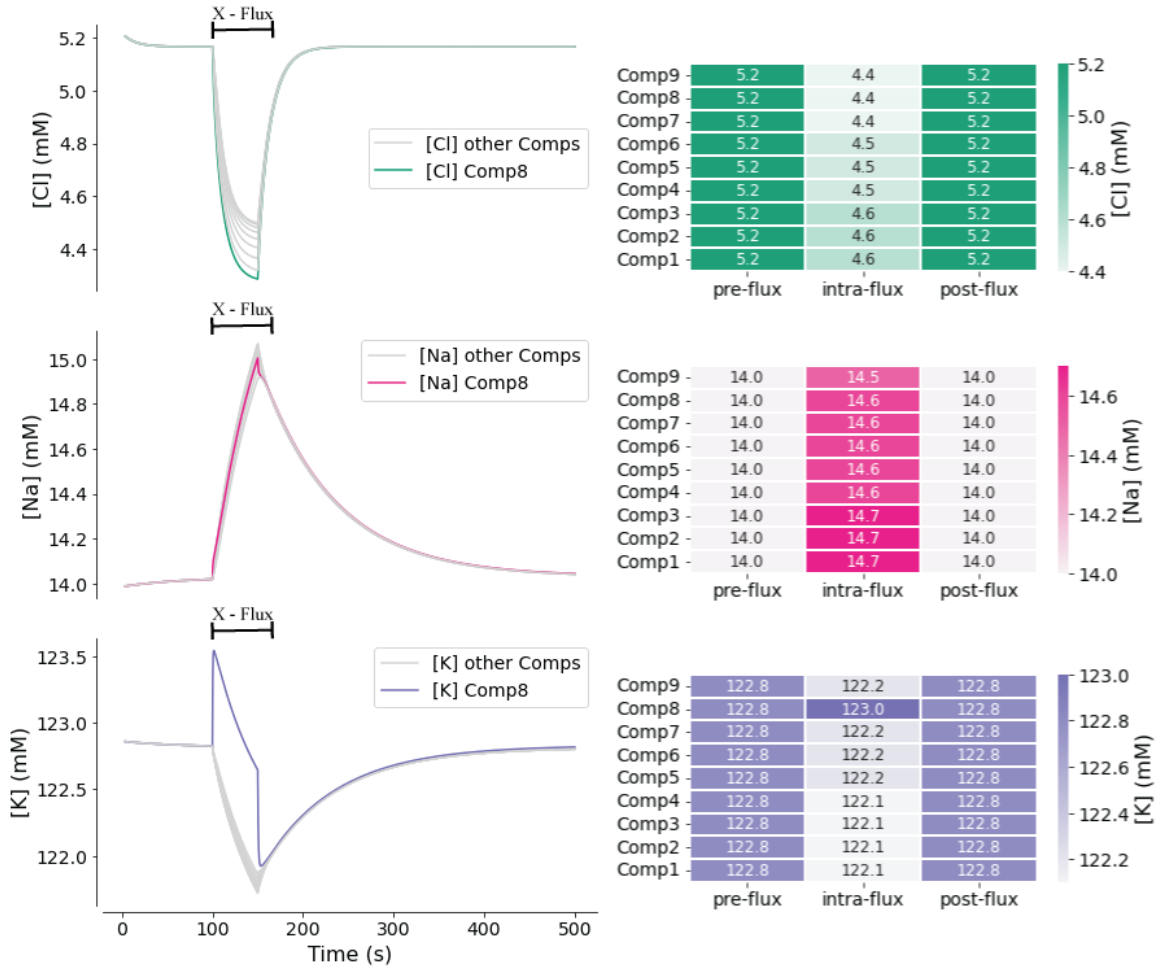

Fig 3.1B: Altering impermeant anion concentration has no effect on steady state concentrations of other ionic species. Using a 9-compartment model, I fluxed impermeant anions (rate: 10^{-15} mol/s; z: -0.85) into Comp8 between 100 and 150s in a 500s simulation.
***Left*:** Line graphs showing concentrations of chloride ($[Cl^-]$ - green), sodium ($[Na^+]$ – pink/red) and potassium ($[K^+]$ – blue) in Comp8 vs. other compartments (colourized vs. grey) for the entire duration of the simulation.
Right: Heat maps quantifying ion concentrations in all compartments at 3 time points: pre-flux (99.99s); intra-flux (125s); post-flux (500s).

Lastly, I evaluated the electrical changes that result from impermeant anion addition without altering mean impermeant anion charge (**Fig 3.1C**). The membrane potential (V_m) dropped transiently in all compartments during impermeant anion flux into Comp8. This was coupled by transient changes in ionic reversal potentials in all compartments. However, at post-flux steady state compartment membrane potential, ionic reversal potentials and ionic driving forces returned to baseline levels.

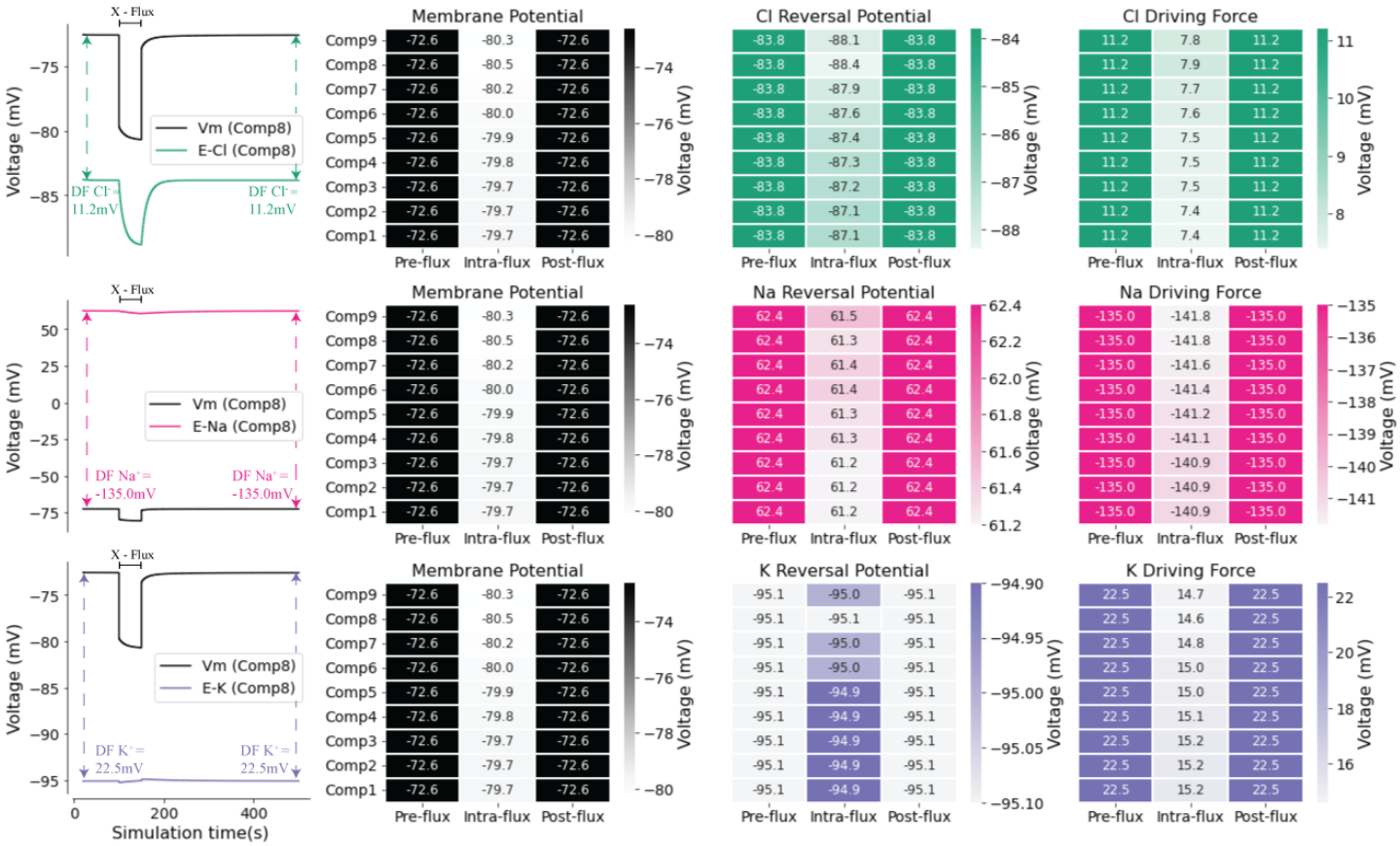

Fig 3.1C: Altering the absolute amount of impermeant anions in a compartment had no effect on steady state membrane potential or ionic reversal potentials.
Using a 9-compartment model, I fluxed impermeant anions (rate: 10^{-15} mol/s; z: -0.85) into Comp8 between 100s and 150s in a 500s simulation.
Line graphs show relationships between membrane potential (Vm : black), chloride reversal potential (E-Cl : green), sodium reversal potential (E-Na : pink), and potassium reversal potential (E-K : blue) in Comp8 for the entire duration of the simulation. Dashed arrows between membrane potential and reversal potential reflect ionic driving forces (DF).
Heat maps quantifying membrane potentials, ionic reversal potentials, and ionic driving forces (membrane potential – ion reversal potential) for all compartments at 3 time points: pre-flux (99.99s); intra-flux (125s); post-flux (500s).

3.2. MODIFYING IMPERMEANT ANION MEAN CHARGE

3.2.1 LOCAL CHANGES TO IMPERMEANT ANION CHARGE ALTERS LOCAL COMPARTMENT VOLUME AND PERMEANT ION CONCENTRATIONS

Using my multicompartment biophysical model, I next tested the effects of changing mean impermeant charge in a single compartment. I decreased impermeant anion mean charge in Comp8 from z = - 0.85 to z = -1.05(" z – change"), gradually between 100s and 200s, while the mean charge of impermeant anions in other compartments remained at baseline (**Fig. 3.2A**).

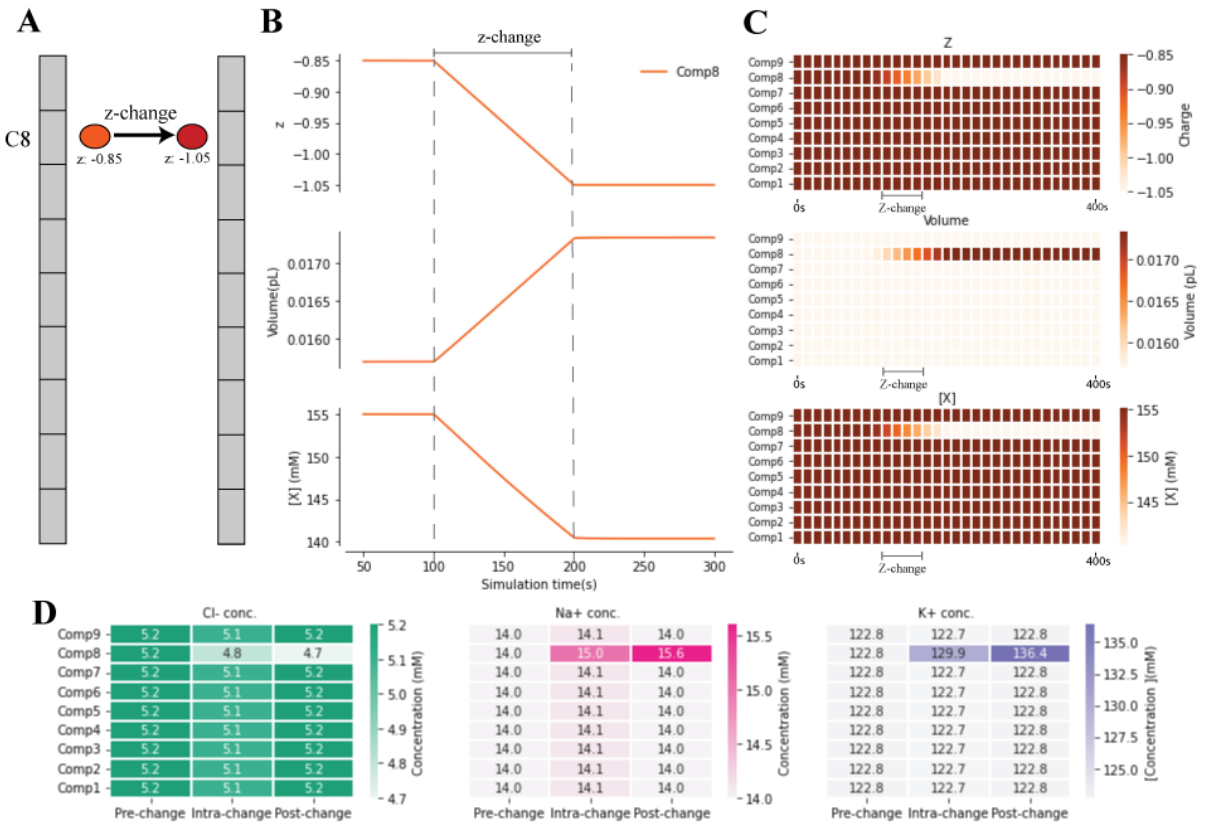

Fig. 3.2A: Impermeant anion mean charge alters local compartment volume and permeant ion concentration.
A: Experimental design. Using a 9-compartment model, impermeant anion average mean charge (z) was reduced from z = -0.85 to z = -1.05 in Comp8 between t=100 to t=200s. Total simulation time = 400s.
B: Line graphs for period t=50s to t=300s showing the linear relationships between z, compartment volume and impermeant anion concentration ([X]) in Comp8.
C: Corresponding heatmaps for period t=0s to t=400s indicating no impermeant anion mean charge, concentration, or volume changes to other compartments during z change into Comp8.
D: Ion concentration pre-change (t=99s), during change (t=150s), and post-change (t=400s).

Impermeant anion mean charge reduction resulted in cations entering the cell, which led to a local increase in Comp8 volume. Impermeant anion and chloride concentrations subsequently decreased. All ion concentrations reached a new equilibrium in Comp8 once the impermeant anion charge stabilized at z = -1.05, while no permanent permeant ion concentration changes were observed in other compartments.

As I was interested in the ionic concentration differences between compartments, I investigated the respective contributions of transmembrane (TM) vs electrodiffusive(ED) ion flux during the simulation(**Fig. 3.2B**).

In Comp8, where z-change occurred, total Na^+ and K^+ moles increased, while Cl^- moles decreased; however, in other compartments total moles of ions at the end of the simulation remained at starting levels. The difference between Comp8 and other compartments arises from electrodiffusive(ED) rather than transmembrane (TM) ion flux (which appears to be similar between compartments).

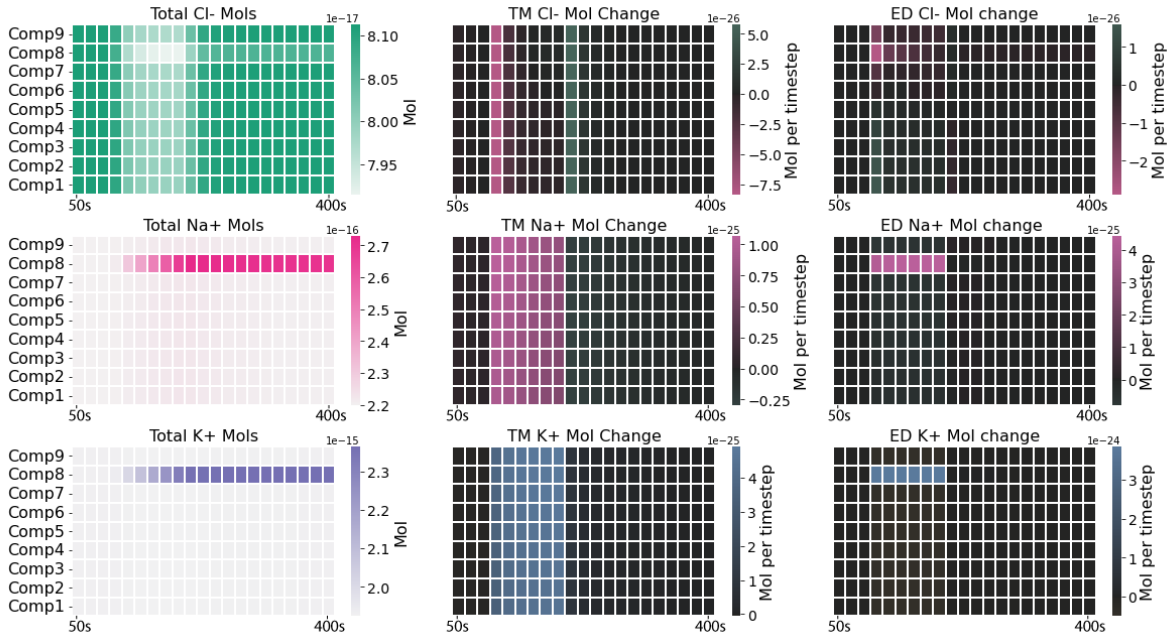

Fig. 3.2B: Ionic flux via electrodiffusion permits local differences in compartmental ion concentrations following alteration of mean impermeant anion charge. Using a 9-compartment model, impermeant anion average charge (z) was reduced from z = -0.85 to z = -1.05 in Comp8 between 100 - 200s. Total simulation time = 400s. Time step = 10^{-6} s. TM = Transmembrane; ED = Electrodiffusion.
Heatmaps show total ion moles, TM mole change per time step and ED mole change per time step in each compartment for Cl^- (top row), Na^+ (middle row), and K^+ (bottom row) between 50s and 400s.

Note that in these simulations we observed a permanent increase in intracellular Na+ concentration in the compartment, which was manipulated. Since the Na+/ K+ ATPase pump rate is dependent on intracellular Na+ concentration (Keener and Sneyd, 2009), this would be predicted to increase the Na+/ K+ ATPase pump rate and the consumption of ATP. Unlike in our previous modelling work (Düsterwald et al., 2018) here we deliberately wanted to exclude the potential consequences of this indirect active process on our results. We therefore clamped the Na+/ K+ ATPase pump rate throughout the simulations that follow.

3.2.2 LOCAL CHANGES TO MEAN IMPERMEANT ANION CHARGE CREATE A NON-ISOPOTENTIAL NEURON WITH NO CHANGES TO IONIC DRIVING FORCE

I next examined the membrane and ion reversal effect that might occur with a change to impermeant anion mean charge (**Fig. 3.2C**). Reducing mean impermeant anion charge from z = -0.85 to z = -1.05 led to a permanent drop in the membrane potential (Vm) of Comp 8. All ionic reversal potentials dropped proportionally such that there were no permanent changes to ionic driving forces. The membrane potential of other compartments transiently shifted during the impermeant charge change but returned to pre-change baseline levels. At the end of the simulation, I observe a non-isopotential dendrite at steady state, but with entirely uniform ionic reversal potentials.

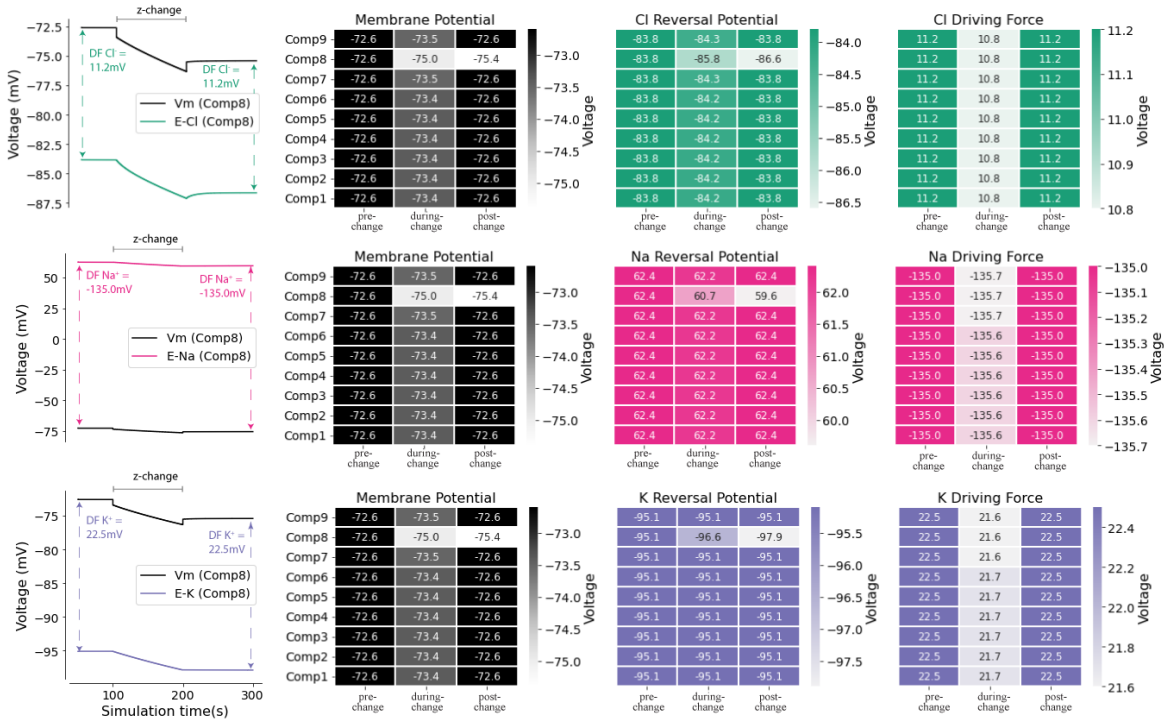

Fig. 3.2C: Impermeant anion mean charge sets local membrane potential without affecting ionic driving forces. Using a 9-compartment model, impermeant anion average charge (z) was reduced from z = -0.85 to z = -1.05 in Comp8 between t=100 to t=200s. Total simulation time = 400s.
Line graphs show relationships between membrane potential (Vm : black), chloride reversal potential (E-Cl : green), sodium reversal potential (E-Na : pink), and potassium reversal potential (E-K : blue) in Comp8 for entire duration of the simulation. Dashed arrows between membrane potential and reversal potential reflect ionic driving forces (DF). Heat maps quantifying membrane potentials, ionic reversal potentials, and ionic driving forces (membrane potential – ion reversal potential) for all compartments at 3 time points: pre-change (t=99s); during (intra) change (t=150s); post-change (t=400s).

Instead of observing the driving forces across the membrane (as in **Fig. 3.2C**), in **Fig. 3.2D** I considered the "driving forces" occurring axially between compartment boundaries. The difference in impermeant anion mean charge between Comp8 and its neighbours resulted in equal but opposite boundary potentials between the Comp7/Comp8 boundary and the Comp8/Comp9 boundary. Similarly, equal but opposite boundary ionic reversal potentials were observed for each ion along these boundaries. The boundary potentials equalled the boundary ionic reversal potentials entailing no boundary (axial) driving force throughout the simulation. This is why despite both local differences in compartment voltage and concentration there is no net flux of any ions at steady state.

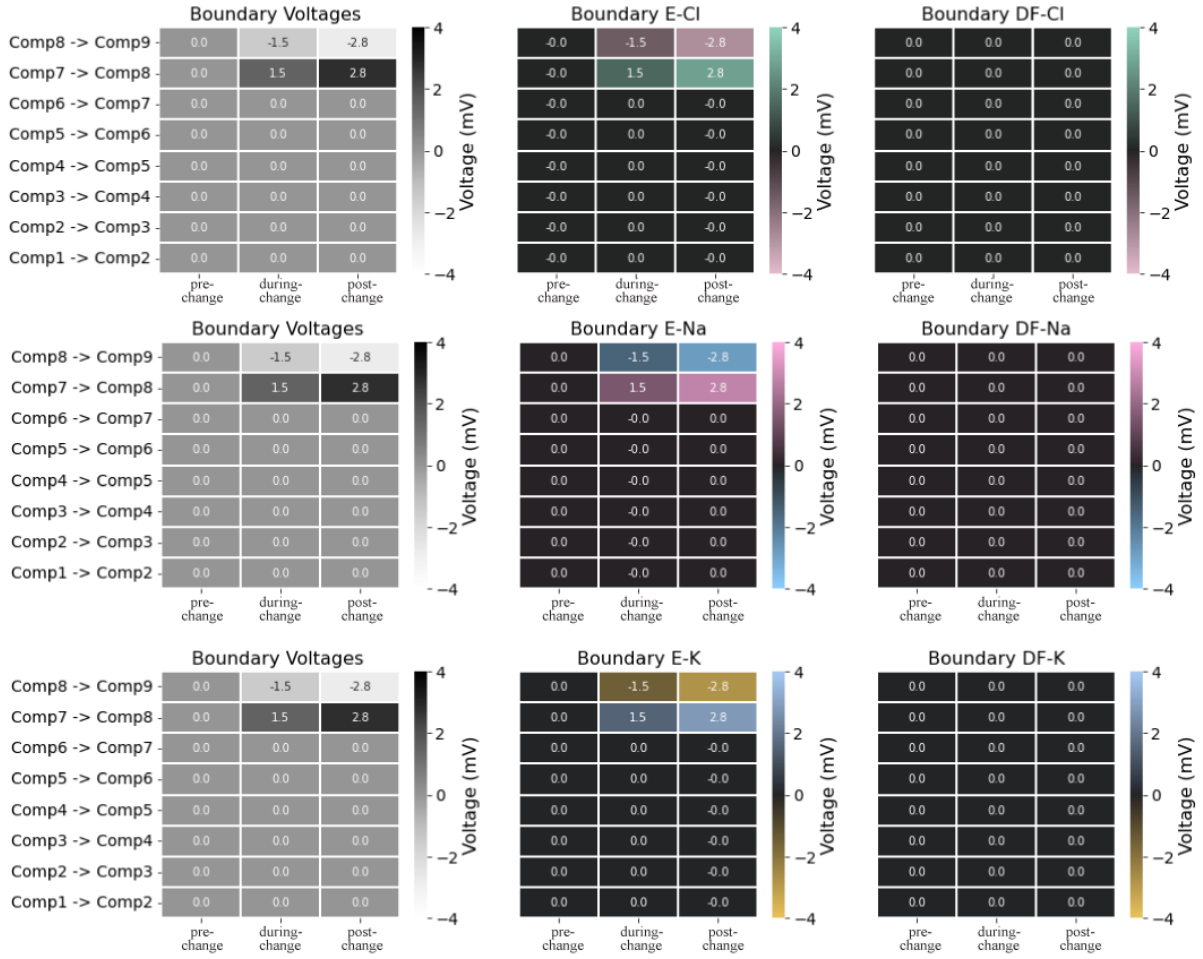

Fig. 3.2D: Differences in impermeant anion mean charge create boundary voltage differences between adjacent compartments without affecting boundary driving forces. Using a 9-compartment model, impermeant anion average charge (z) was reduced from z = -0.85 to z = -1.05 in Comp8 between 100 - 200s. Total simulation time = 400s. Heatmaps demonstrate boundary voltages, boundary reversal potentials (E-ion), and boundary driving forces (DF-ion), for Cl^- (top row), Na^+ (middle row), and K^+ (bottom row) at 3 discrete intervals: pre-change (t = 99s), during (intra) change (t=150s) and post-change (t = 400s).

3.2. MULTIPLE CHANGES IN IMPERMEANT ANION MEAN CHARGE

3.3.1 EFFECTS ACROSS A SPECTRUM OF IMPERMEANT ANION MEAN CHARGE

Using the same 9 compartment model, I evaluated the effects of different impermeant anion mean charge changes in Comp8 across a range of values: z = -0.65;-0.75;-0.85;-0.95;-1.05 (**Fig. 3.3A**). Decreasing the mean charge of impermeant anions led to proportional increases in compartment volume (and resultant decrease in impermeant anion concentration).

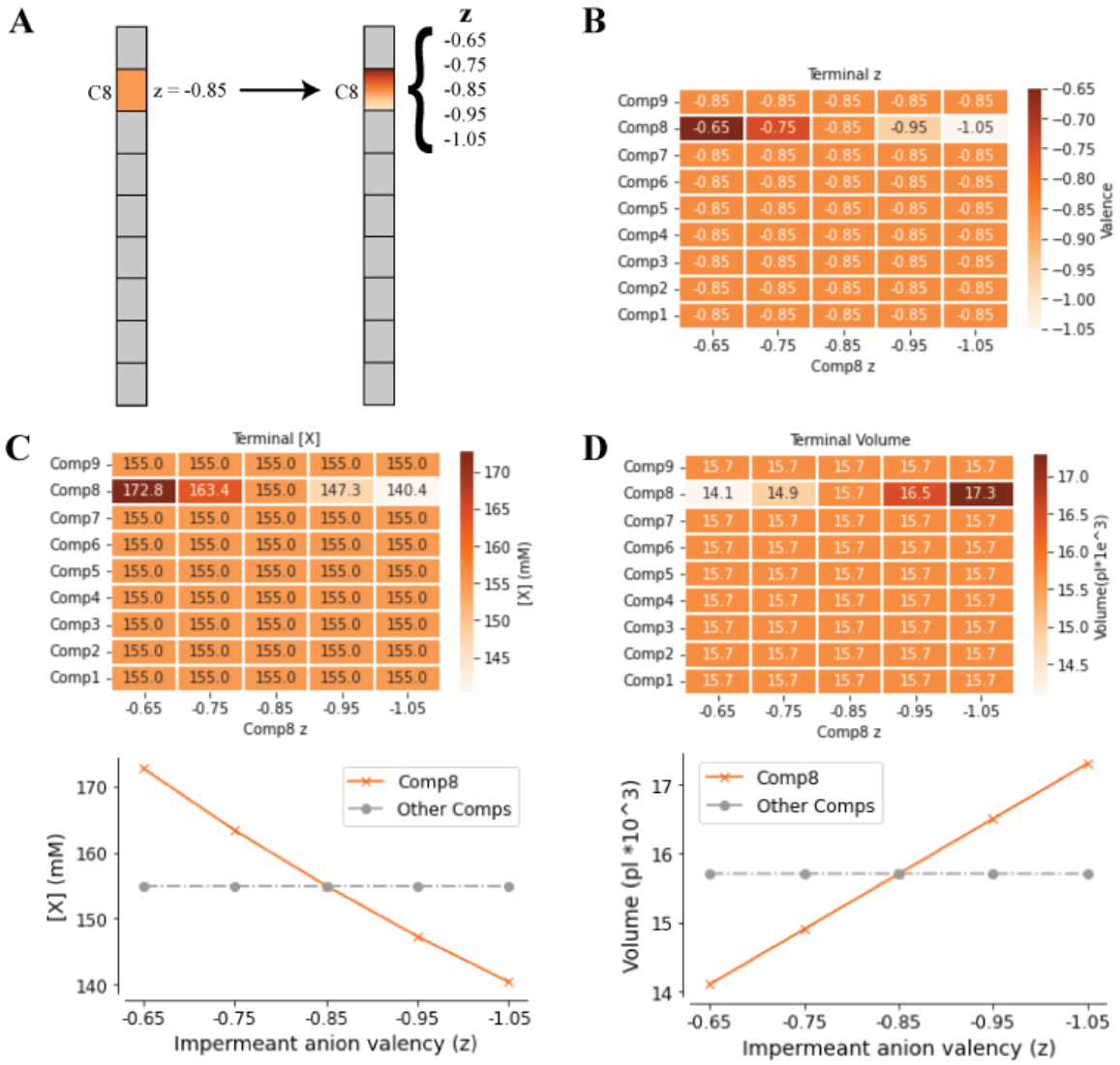

Fig. 3.3A: Compartment volume and impermeant anion concentration is proportional to impermeant anion mean charge

A: Experimental design. Using a 9-compartment model, impermeant anion average charge (z) was reduced from z = -0.85 to z = [-0.65;-0.75;-0.85;-0.95;-1.05] in Comp8 between t=100 to t=200s. Total simulation time = 400s.

B: Heatmap showing z changes occurring only in Comp8 across the various simulations.

C: Heatmap showing terminal (t=400s) impermeant anion concentration ([X]) across the mean charge spectrum with corresponding line graph displaying near linear relationship between z and [X].

D: Heatmap showing terminal (t=400s) compartment volume across the mean charge spectrum with corresponding line graph displaying near linear relationship between z and volume.

Local changes to impermeant anion mean charge establish ionic microdomains (compartments with differing ionic concentrations relative to its neighbours) (**Fig. 3.3B**). Chloride microdomain concentrations are non-linearly proportional to impermeant anion mean charge.

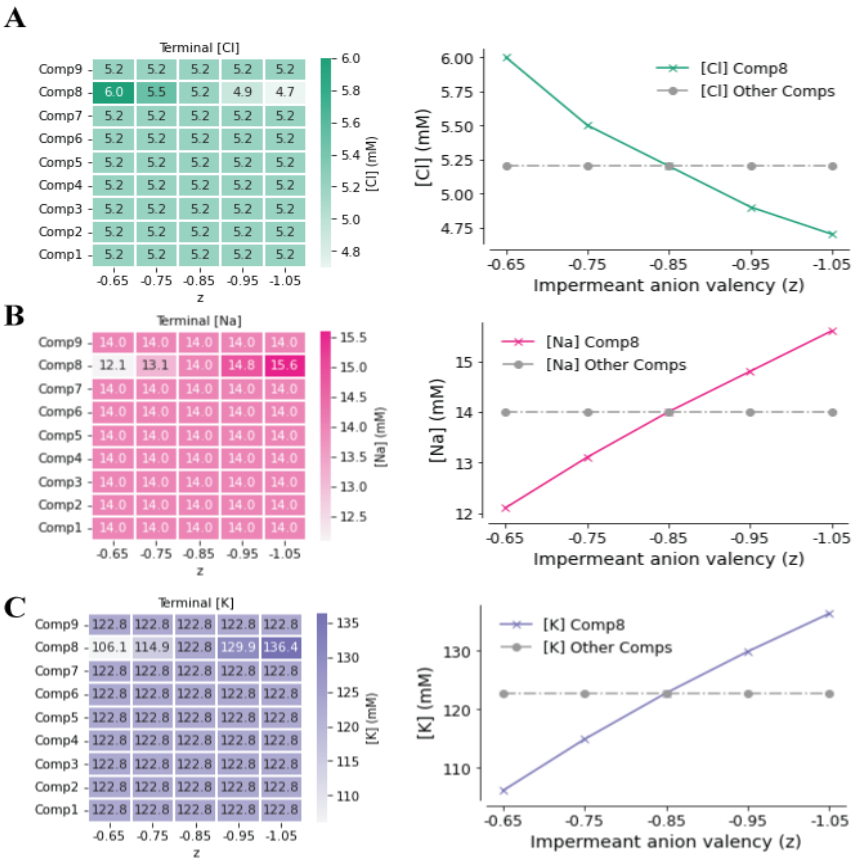

Fig. 3.3B: Local differences in impermeant anion mean charge establish ionic microdomains. Using our multicompartment model five separate simulations were run each with unique impermeant anions mean charge (z) in Comp8: z = -0.65 ; -0.75 ; -0.85; -0.95; -1.05. Heatmaps demonstrate the steady state (terminal) values for ionic concentrations with complimentary line graphs showing relationship between impermeant anion mean charge and [Cl^-] **(A)**, [Na^+] **(B)**, and [K^+] **(C)** microdomains.

Despite the non-linear relationship between chloride microdomain concentrations and impermeant anion mean charge, the transmembrane driving force for chloride remains consistent at 11.2mV across the range of impermeant mean charges (**Fig. 3.3C**). The same phenomenon is observed with Na^+ (DF = 135mV) and K^+ (DF = -22.5mV). This occurs as the membrane potential shifts exactly in tandem with the ionic reversal potentials.

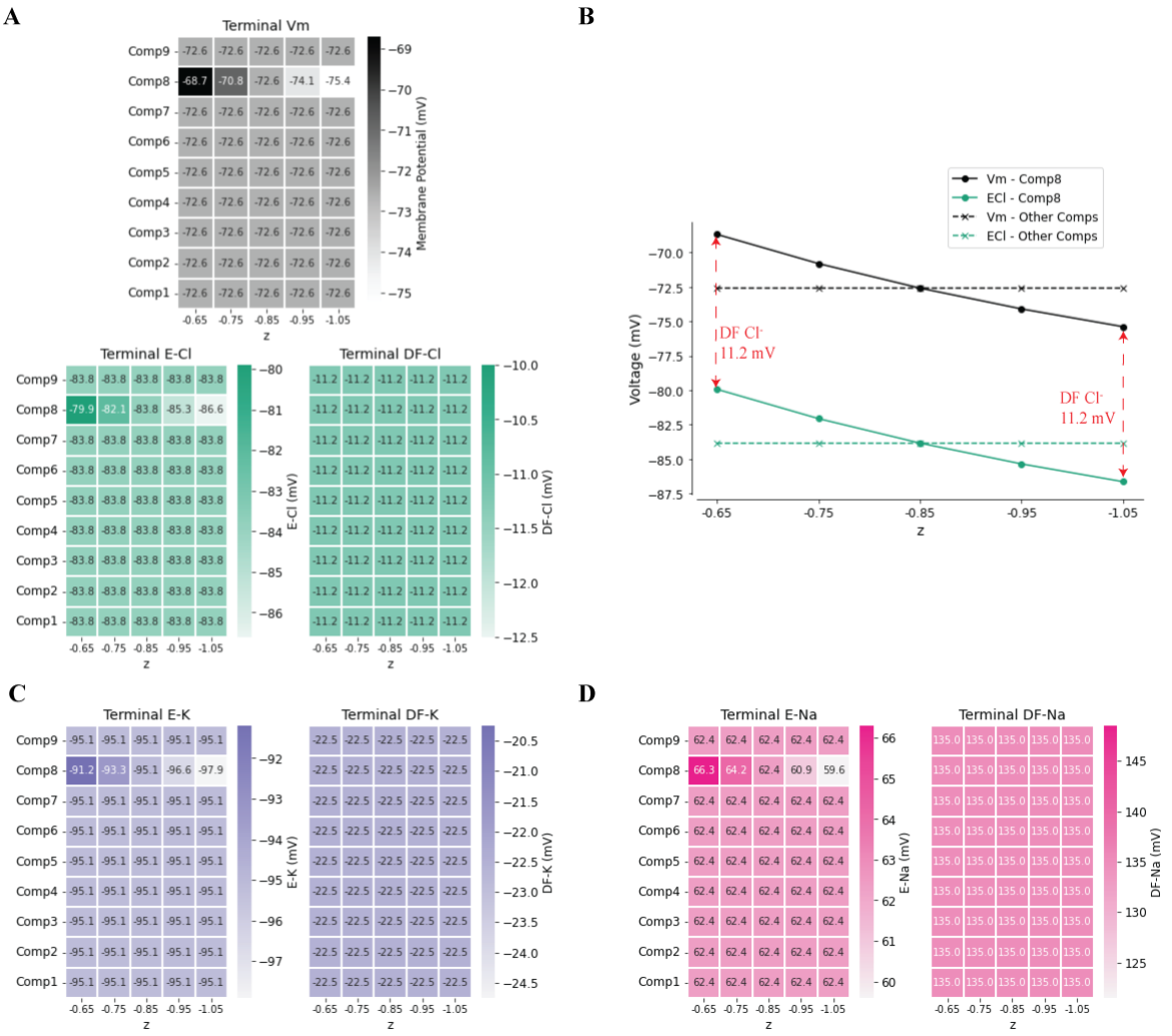

Fig. 3.3C: Conserved transmembrane ionic driving forces irrespective of impermeant anion mean charge. Using our multicompartment model five separate simulations were run each with unique impermeant anions mean charge (z) in Comp8: z = -0.65 ; -0.75 ; -0.85; -0.95; -1.05. Heatmaps demonstrate the steady state (terminal) membrane potentials (V_m), ionic reversal potentials (E_{ion}), and ionic driving forces (DF_{ion}).
A&B: Heatmap and complementary line graphs showing linear relationship shown between V_m and E_{Cl} in Comp8 such that DF_{Cl} remains identical in all compartments across range of impermeant anion mean charges.
C&D: Heatmaps showing although reversal potentials shift, DF_K and DF_{Na} remain consistent across impermeant anion mean charges.

Like transmembrane potentials, boundary potentials also have a relationship with impermeant anion mean charge (**Fig. 3.3D**). However, unlike transmembrane potentials, the relationship between impermeant anion mean charge and boundary potential is non-linear as higher impermeant anion mean charge created greater boundary potentials (z = -0.65; V_b = 3.9mV) relative to lower impermeant anion mean charge (z = -1.05; V_b = 2.8mV). However, as boundary ionic reversal potentials vary precisely with boundary voltages there is no boundary driving force irrespective of impermeant anion mean charge.

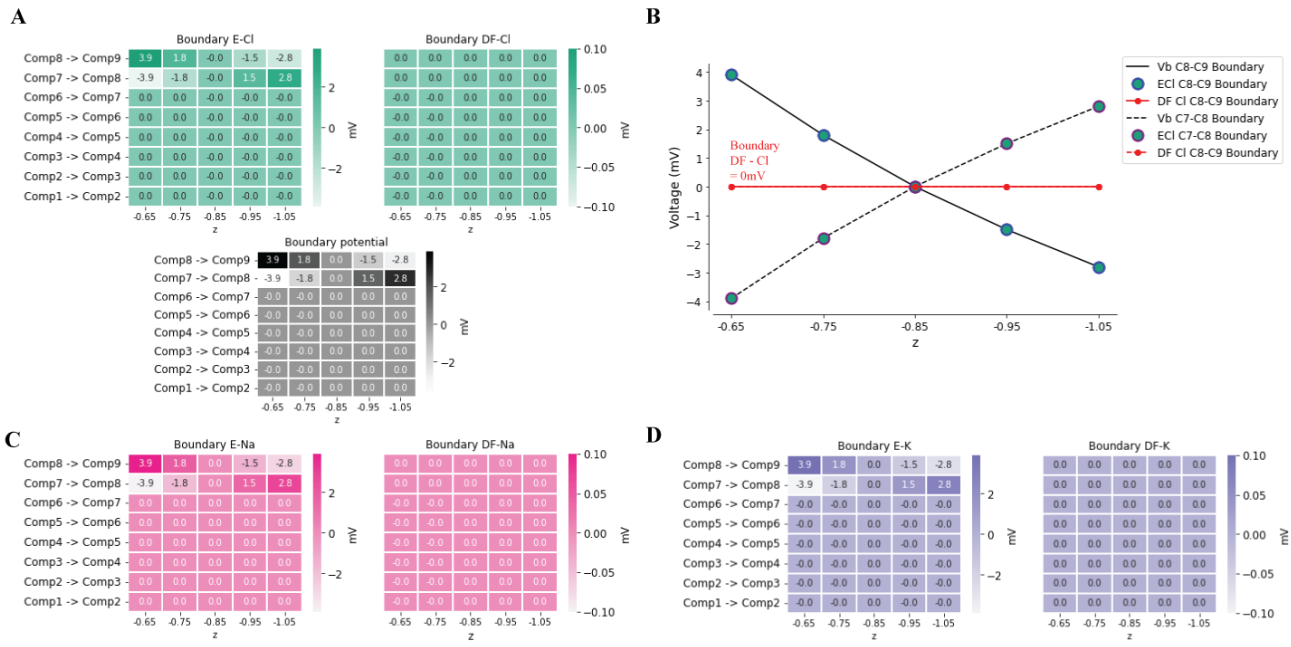

Fig. 3.3D: Zero boundary driving force irrespective of impermeant anion mean charge. Using our multicompartment model five separate simulations were run each with unique impermeantanions mean charge (z) in Comp8: z = -0.65 ; -0.75 ; -0.85; -0.95; -1.05. Heatmaps above demonstrate the steady state (terminal) boundary potentials (V_b), boundary ionic reversal potentials (E_{ion}), and boundary ionic driving forces (DF_{ion}).
A&B: Heatmaps and corresponding line graphs showing equal but opposite relationship between V_b and Boundary - E_{Cl} across the Comp7-Comp8 boundary and Comp8-Comp9 boundary. Boundary DF_{Cl} remains at 0mV across all impermeant anion mean charges.
C&D: Heatmaps demonstrate boundary E_{Na} and E_K are identical to boundary E_{Cl}. Boundary driving forces for all permeant ions are 0mv.

3.3.2 MULTIPLE IMPERMEANT ANION MEAN CHARGE CHANGES WITHIN THE SAME DENDRITE CREATE IONIC MICRODOMAINS WITHOUT AFFECTING IONIC DRIVING FORCES

I next explored whether the above results above could be repeated but in the case of multiple impermeant anion mean charge changes in adjacent compartments within a single dendrite (**Fig. 3.3E**). In Comp4 impermeant anion mean charge was raised from z = -0.85 to z = -0.65, and in Comp5 impermeant anion mean charge was reduced from z = -0.85 to z = -1.05.

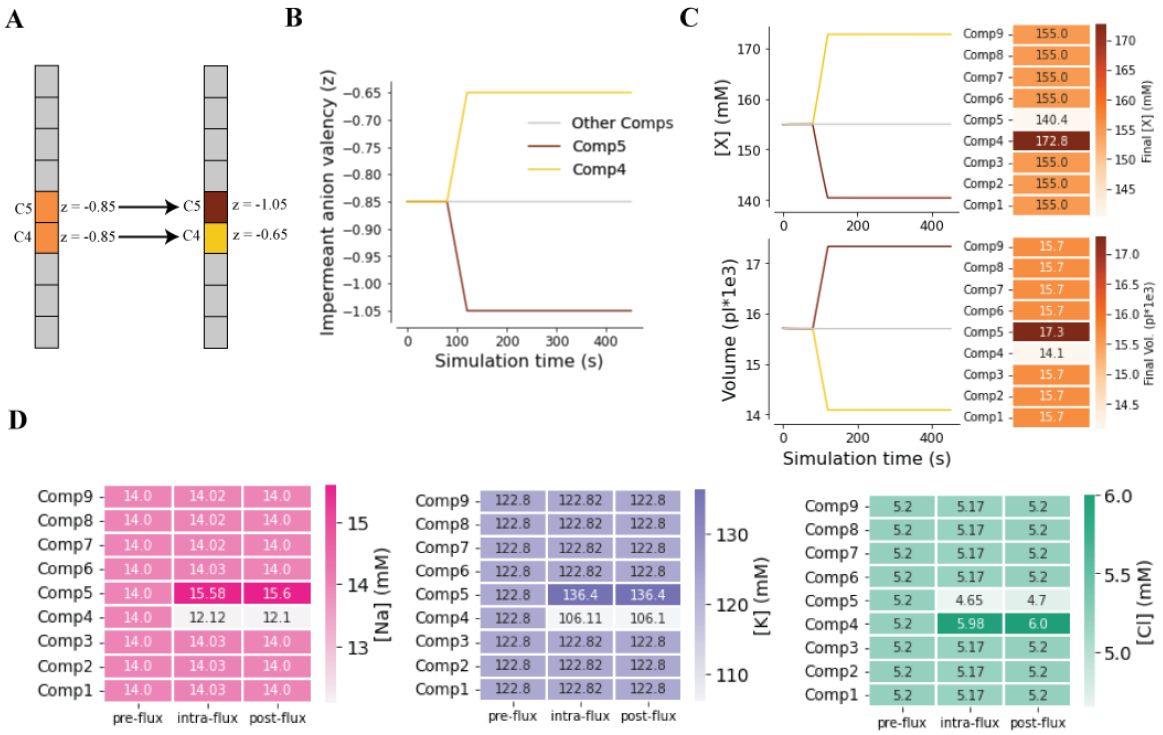

Fig. 3.3E: Multiple ionic microdomains can occur within a dendrite
A: Experimental design. Using a 9-compartment model, impermeant anion average charge (z) was reduced from z = -0.85 to z = -0.65 in Comp4 and to z = -1.05 in Comp5 between t=100 to t=130s. Total simulation time = 450s.
B: Impermeant anion mean charge change occurred only in Comp4 and Comp5, while other compartments remained at baseline mean charge (z = -0.85).
C: Changes to impermeant anion mean charge in Comp4 and Comp5 resulted in a dendrite with altering volumes and impermeant anion concentrations. Heatmaps quantify changes at the end of the simulation (t=450s).
D: Changes to compartment impermeant anion mean charges in Comp4 and Comp5 resulted in a dendrite with adjacent ionic microdomains that arose post impermeant mean charge manipulation. Heatmaps quantify ionic concentrations pre-change (t=99s), during (intra) change (t=115s) and post-change (t=450s).

I found that the dendrite could reach a physiological steady state with these parameters. At steady state the simulated dendrite had compartments of differing volumes adjacent to each other: Comp3: 15.7 x 10^{-3} pl; Comp4:14.1 x 10^{-3} pl ,Comp5: 17.3 x 10^{-3} pl. Ionic microdomains occurred in the compartments with altered impermeant anion mean charges that have identical concentrations to the microdomains in the single z change simulations above.

The dendrite was non-isopotential (**Fig. 3.3F**) at rest with adjacent areas of heterogenous membrane potentials: Comp3: -72.6mV; Comp4: -68.7mV; Comp5: -75.4mV. As expected from the simulations above, there was no impact on the transmembrane driving force and the boundary ionic driving forces were 0mV across the entire dendrite.

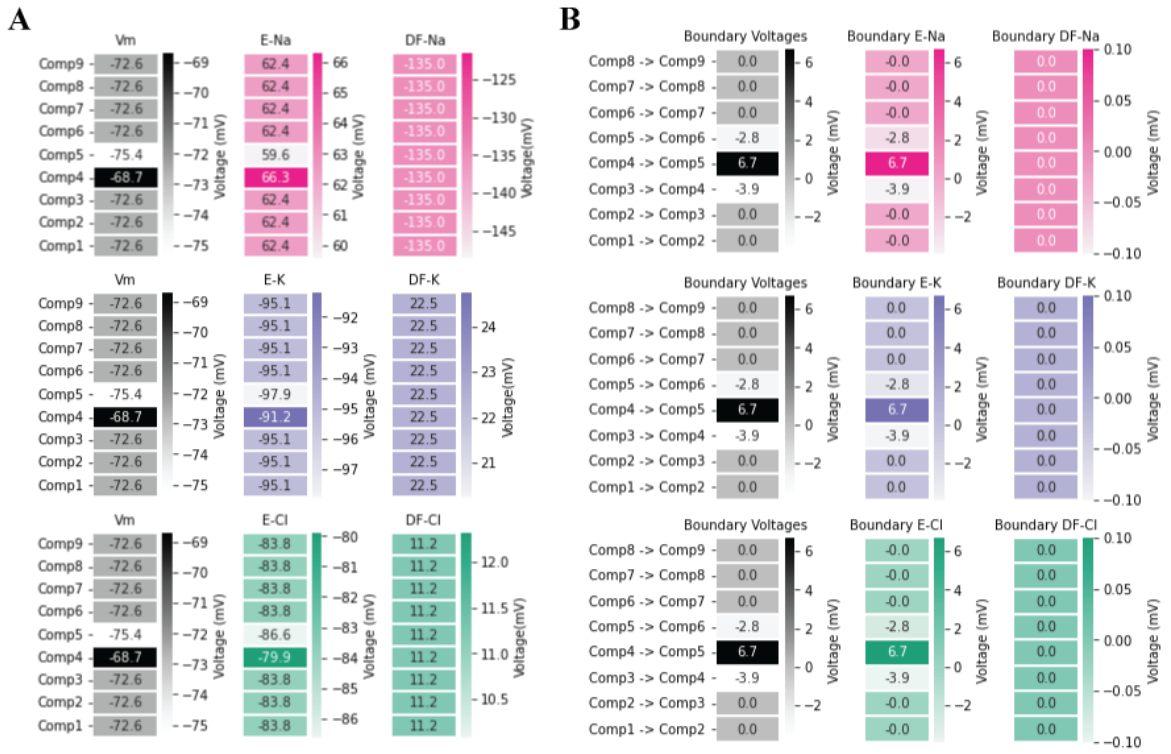

Fig. 3.3F: Non-isopotential dendrites have identical ionic driving forces
Using a 9-compartment model, impermeant anion mean charge (z) was reduced from z = -0.85 to z = -0.65 in Comp4 and to z = -1.05 in Comp5 between t=100 to t=130s. Total simulation time = 450s.
A: Heatmaps above demonstrate the steady state (terminal: t=450s) membrane potentials (V_m), ionic reversal potentials (E_{ion}), and ionic driving forces (DF_{ion}).
B: Heatmaps above demonstrate the steady state (terminal: t=450s) boundary potentials (V_b), boundary ionic reversal potentials (E_{ion}), and boundary ionic driving forces (DF_{ion}). Note the constant membrane potential and compartment driving forces across the entire model.

3.3. IMPERMEANT ANIONS AND PASSIVE CABLE PROPERTIES

3.4.1. COMPARISON BETWEEN THE ELECTRODIFFUSION BASED MODEL AND EQUIVALENT CIRCUIT MODEL

I next compared the passive electrical properties of my multicompartment electrodiffusion model based on the pump-leak mechanism and which uses the "charge difference" approach to calculating the membrane voltage, to an equivalent circuit-based model (using the "charge sum" approach to calculating membrane voltage) constructed in NEURON[1,2], the standard simulation package in the field of neuronal biophysics. In each simulation environment I pulsed a step current of +0.1nA with a 1ms duration into Compartment 9 and compared the voltage traces that were elicited(**Fig. 3.4A**).

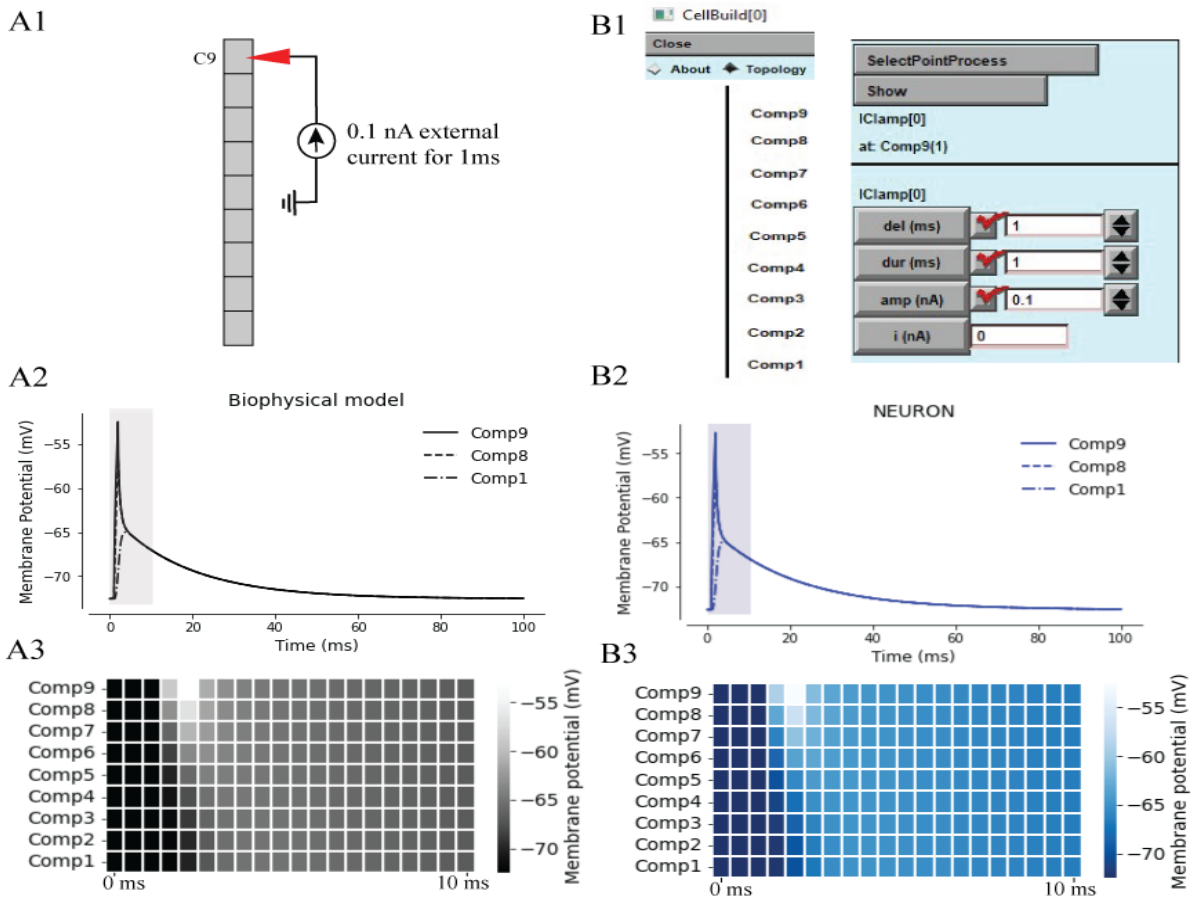

Fig. 3.4A: Comparing the electrodiffusion based biophysical neuronal model to an equivalent circuit-based NEURON model. In a 9-compartment linear model a +0.1nA current was passed into Comp9 for a duration of 1ms. **A1:** Experimental design for biophysical model. **B1:** Cell builder feature in NEURON showing a linearly arranged 9 compartment topology, with external current pulsed via a clamp ("IClamp") occurring on Comp9. **A2 & B2:** Resultant membrane potential traces for Comp9, Comp8 and Comp1 shown for respective models. Amplitude of depolarization in Comp9: -52.46 mV (biophysical model); -52.71mV (NEURON model). **A3 & B3:** Heatmaps below show voltage attenuation across space (y-axis) and time (x-axis) for the first 10ms of the simulation (shaded regions in A2 and B2).

The voltage wave morphology and passive signalling properties of both models are comparable (**Fig. 3.4B**). There was a sharp rise in membrane potential, reaching a maximum amplitude of depolarization in Comp 9 of -52.46mV in the biophysical model, and -52.71mV in the NEURON model. There was also similar current attenuation: in the electrodiffusion-based biophysical model (τ = 16.57ms; λ = 49.04µm) relative to the NEURON model (τ = 18.4ms; λ = 48.57µm).

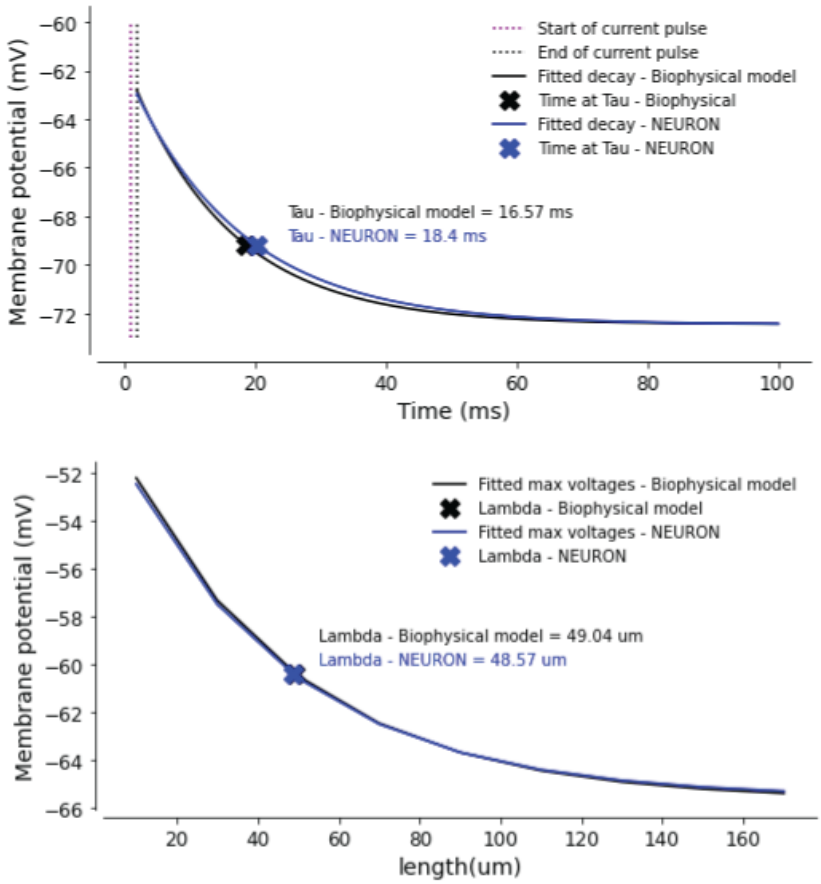

Fig. 3.4B: Minimal difference in the passive signalling properties of the biophysical and NEURON models. In a 9-compartment linear model a +0.1nA current was passed into Comp9 for a duration of 1ms and allowed to decay until 100ms. This setup was performed in the electrodiffusion based biophysical model (left) and equivalent circuit-based NEURON model (right). **Top row:** Time constants (Tau = τ) for each simulation calculated on Comp9: 16.57ms (biophysical model); 18.4ms (NEURON model) . **Bottom row:** Length constants (Lambda = λ) for each of the simulation: 49.04µm (biophysical model) ; 48.57µm (NEURON model)

3.4.2 Dendritic cable properties are largely uncharged when impermeant anion mean charge is varied in a single compartment

In my electrodiffusion based model, I examined the influence a local change in impermeant anion mean charge could have on the passive cable properties of dendrites (**Fig. 3.4C**). Impermeant anion mean charges of z=-0.65;-0.85 and -1.05 were set in Comp8, with volume normalization performed on Comp8 to ensure all that compartment volumes were similar (see Methods). A +0.1nA current for 1ms was pulsed into Comp9 in each simulation. Time and length constants were similar regardless of the mean charge.

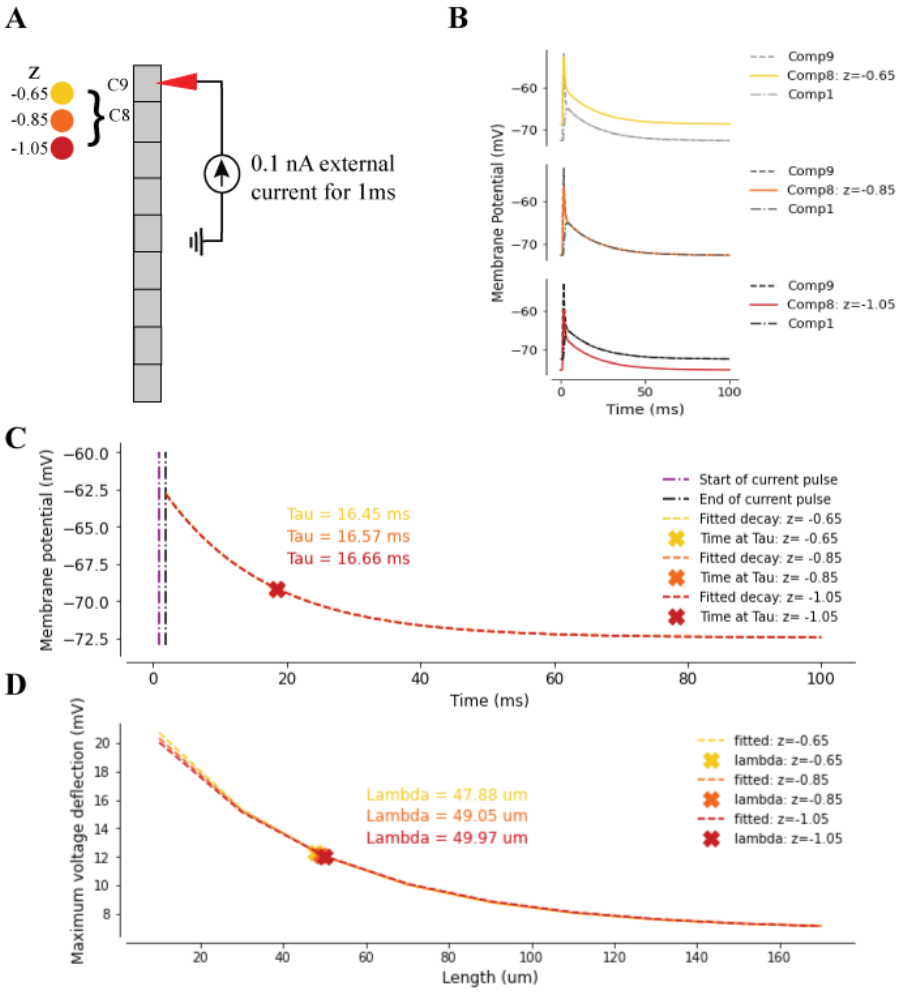

Figure 3.4C: Impermeant anion mean charge changes negligibly affect passive signalling properties.
A: Experimental design. In 3 separate simulations, each with altered impermeant anion mean charge in Comp8 (z=-0.65 ; = -0.85; =-1.05), a +0.1nA current was pulsed into Comp9 for a duration of 1ms**. B:** Voltage tracing for the 3 simulations. Each showing the tracing in Comp9, Comp8, and Comp1. Maximum voltage deflection in Comp9: -52.06mV (z = -0.65); -52.46mV (z= -0.85); -52.76 (z = -1.05). **C:** Time constants (Tau = τ) for each of the simulations: 16.45ms (z = -0.65); 16.57ms (z= -0.85); 16.66 (z = -1.05). **D:** Length constants (Lambda = λ) for each of the simulations: 47.88µm (z = -0.65); 49.05µm (z= -0.85); 49.97µm (z = -1.05).

3.4. IMPERMEANT ANIONS AND SYNAPTIC TRANSMISSION

I next extended my electrodiffusion, pump-leak based biophysical model by joining a soma (length: 40µm; diameter 2µm) with Hodgkin-Huxley channels onto Comp1 to investigate the impact of changing the mean charge of impermeant anions on synaptic integration and action potential generation. Since I use the charge difference method for calculating membrane potential, any changes in compartment volume affect the voltage changes elicited by a given influx of charge. To exclude this effect, I normalized compartment volume when changing impermeant anion mean charge (by adjusting the absolute amount of impermeant anions in a compartment – see methods) thereby ensuring any possible differences in synaptic transmission were due purely to the potential electrical effects of impermeant anions.

3.5.1 IMPERMEANT ANION MEAN CHARGE DOES NOT AFFECT SUBTHRESHOLD EXCITATORY AND INHIBITORY SYNAPTIC INPUT

In compartment 8 (C8) of our extended multicompartment model I altered impermeant anion mean charge by substantial amounts(z = -0.65; z = -0.85; z = -1.05) and allowed the simulation to reach steady state. I then simulated a subthreshold excitatory synaptic input on C8 (g_{NMDA} = 1nS; max neurotransmitter concentration = 1mM) starting at 20ms with a 5ms (**Fig. 3.5A - A**). The shape of the synaptic input was non-linear (described in Methods section 2.7.1). Although there were differences in C8 resting membrane potential across impermeant anion mean charges as expected, no changes were seen at the soma irrespective of upstream impermeant anion change.

I then repeated the model setup with an inhibitory synapse instead of an excitatory synapse onto Comp8 (g_{GABA} = 3nS; maximum neurotransmitter concentration = 1mM) **Fig.5A - B**). Similarly, despite the altered baseline membrane potential in Comp8 across impermeant anion mean charges, there was no change to the extent of hyperpolarization.

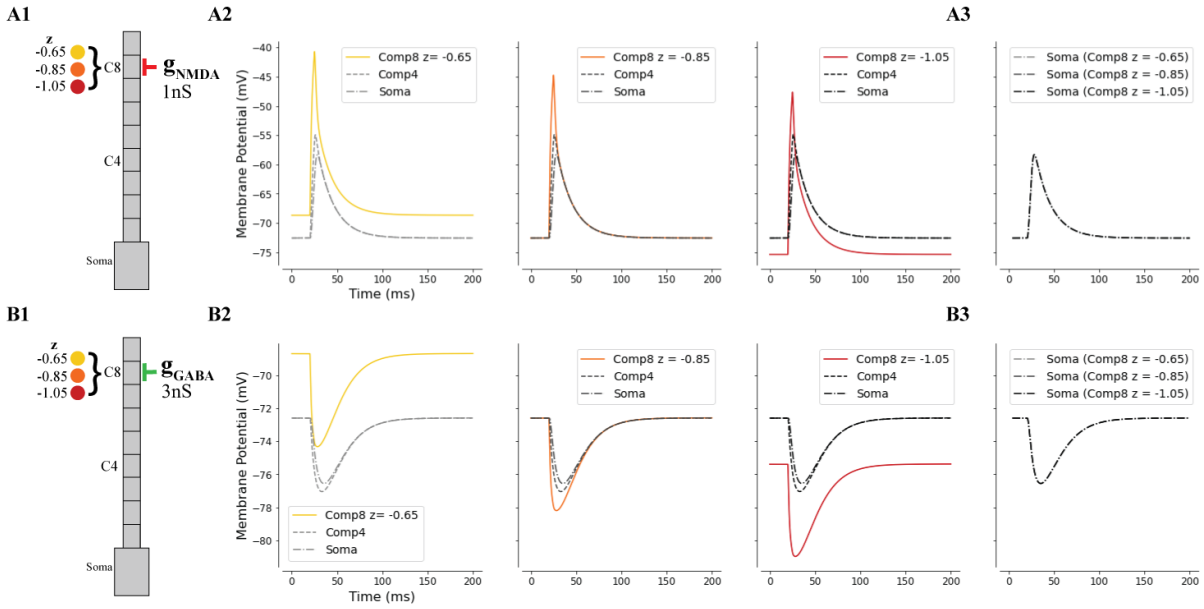

Fig. 3.5A: Subthreshold excitatory and inhibitory inputs onto compartments with altered impermeant anion mean charge show no differential impact at the soma.
Using the extended multicompartment model I altered the impermeant anion mean charge in Comp8 (z = -0.65 shown in yellow ; z = -0.85 shown in orange; z = -1.05 shown in red) and allowed the model to reach a steady state. **A1:** Experimental setup. Subthreshold excitatory glutamatergic input (g_{NMDA} = 1ns; maximum neurotransmitter concentration = 1mM, duration = 5ms) directed on Comp8 occurring at 20ms in a 200ms simulation. **A2:** Membrane potential changes in Comp8, Comp4 and the Soma across simulation time. **A3:** Superimposed membrane potential changes occurring at the soma for each of the different mean charges of impermeant anions.
B1: Experimental setup. Inhibitory GABAergic inputs (g_{GABA} = 3ns; maximum neurotransmitter concentration = 3mM; duration= 5ms) directed on Comp8 occurring at 20ms in a 200ms simulation. **B2:** Membrane potential changes in Comp8, Comp4 and the Soma across simulation time. **B3:** Superimposed membrane potential changes occurring at the soma for each of the different impermeant anion mean charge values.

3.5.2 IMPERMEANT ANION MEAN CHARGE DOES NOT AFFECT ACTION POTENTIAL DYNAMICS

In compartment 8 (C8) of our extended multicompartment model I altered impermeant anion mean charge (z = -0.65; z = -0.85; z = -1.05) and allowed the simulation to reach steady state including ensuring all compartments have the same volume (see Methods). In each of these simulations C8 then received a suprathreshold excitatory synapse (g_{NMDA} = 3nS; max neurotransmitter concentration = 3mM) starting at 20ms with a 5ms synapse duration (**Fig. 3.5B - A**). As expected from the results of subthreshold excitation to Comp8, there is no change in the action potential amplitude or morphology despite the impermeant anion mean charge change in the compartment which received the synaptic input.

Using the same simulation setup, I tested whether differences in impermeant anion mean charge along the dendrite (Comp4) (**Fig. 3.5B - B**), or at Soma (**Fig. 3.5B - C**), would influence the effect of the synaptic input at Comp8. Impermeant anion mean charge differences along the dendrite or soma did not impact action potential generation, amplitude, or morphology.

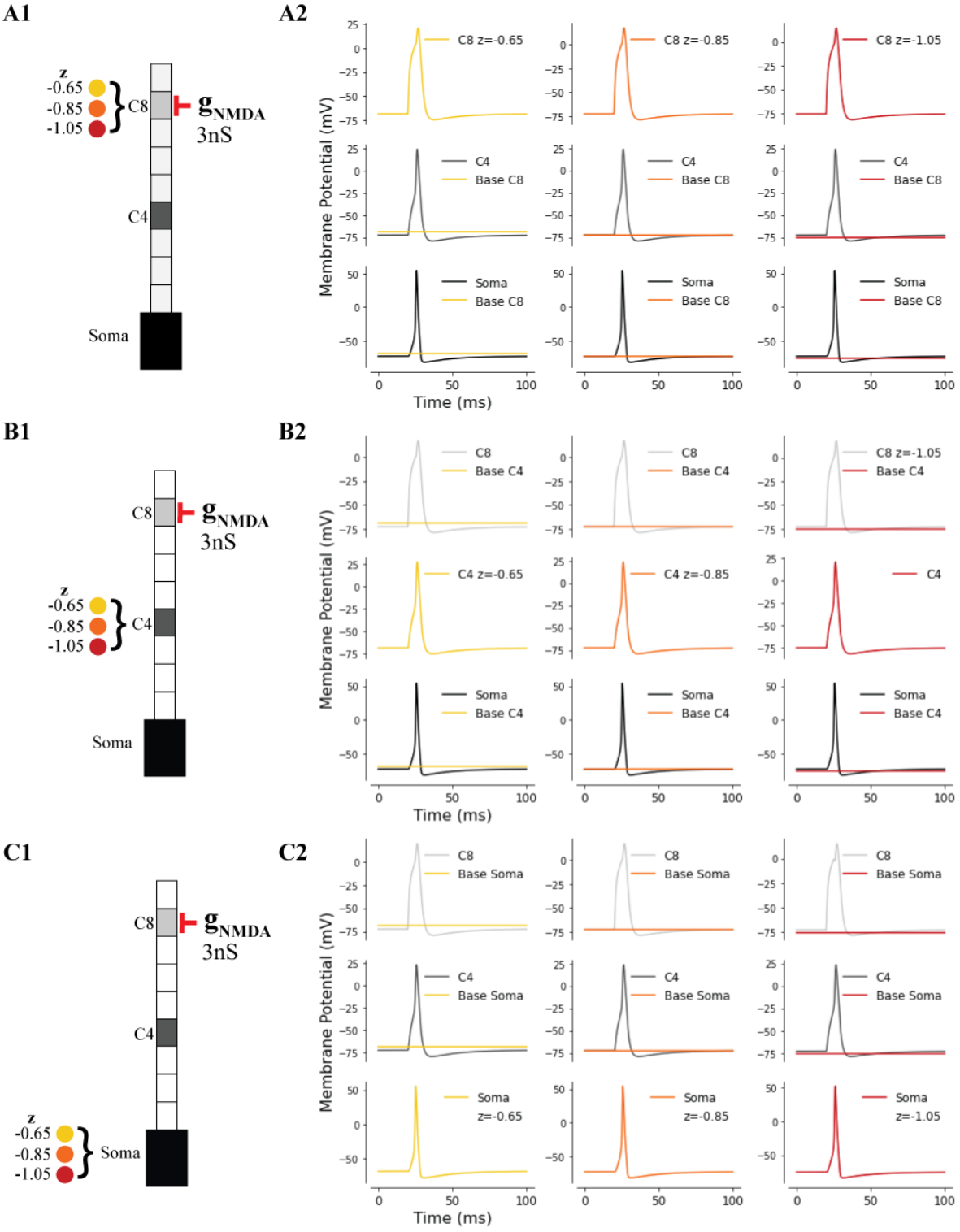

Fig. 3.5B: The mean charge of impermeant anions have no effect on action potential dynamics. Using the extended multicompartment model we altered impermeant anion mean charge (z = -0.65 shown in yellow; z = -0.85 shown in orange ; z = -1.05 shown in red) at the synapse origin (Comp8, **A1**), along the dendrite (Comp4, **B1**) and at the Soma (**C1**). Volume normalization protocol was performed, and the simulation allowed to reach a steady state before adding synaptic input. On Comp8 we directed suprathreshold excitatory glutamatergic inputs (g_{NMDA} = 3ns; maximum neurotransmitter concentration = 3mM, duration = 5ms) occurring at 20ms in a 200ms simulation. **A2, B2, C2:** Membrane potential changes for 100ms of the simulation are shown in Comp8, Comp4 and Soma (top to bottom) for each impermeant anion mean charge change (left to right). Compartments with altered z are colorized.

3.5. KCC2 CONDUCTANCE, AND NOT IMPERMEANT ANION MEAN CHARGE, AFFECTS SYNAPTIC INTEGRATION

3.6.1 SYNAPTIC INTEGRATION IN THE MULTICOMPARTMENTAL NEURON

I evaluated the relationship between excitation and inhibition to better understand synaptic integration in the extended multicompartmental model. An excitatory glutamatergic NMDA synapse (α rate constant = $2x10^6$ $s^{-1}M^{-1}$; β rate constant = $1x10^3$ s^{-1}; maximum neurotransmitter concentration = 3mM) was modelled on Comp8, while an inhibitory GABAergic synapse (α rate constant= $0.5x10^6$ $s^{-1}M^{-1}$; β rate constant = $0.1x10^3$ s^{-1} ; maximum neurotransmitter concentration = 3mM) was modelled on Comp4. Using this setup, I probed what degree of excitation at Comp8 would overcome inhibition at Comp4 and trigger an action potential at the soma (**Fig. 3.6A**).

I varied excitatory and inhibitory conductances (g_{NMDA} & g_{GABA}) to increase the relative strength of excitation and inhibition. At g_{GABA} = 6nS, action potentials occurred when g_{NMDA} > 4nS; At g_{GABA} = 10nS, action potentials occurred when g_{NMDA} > 6nS; At g_{GABA} = 14nS, action potentials only occurred when g_{NMDA} > 10nS.

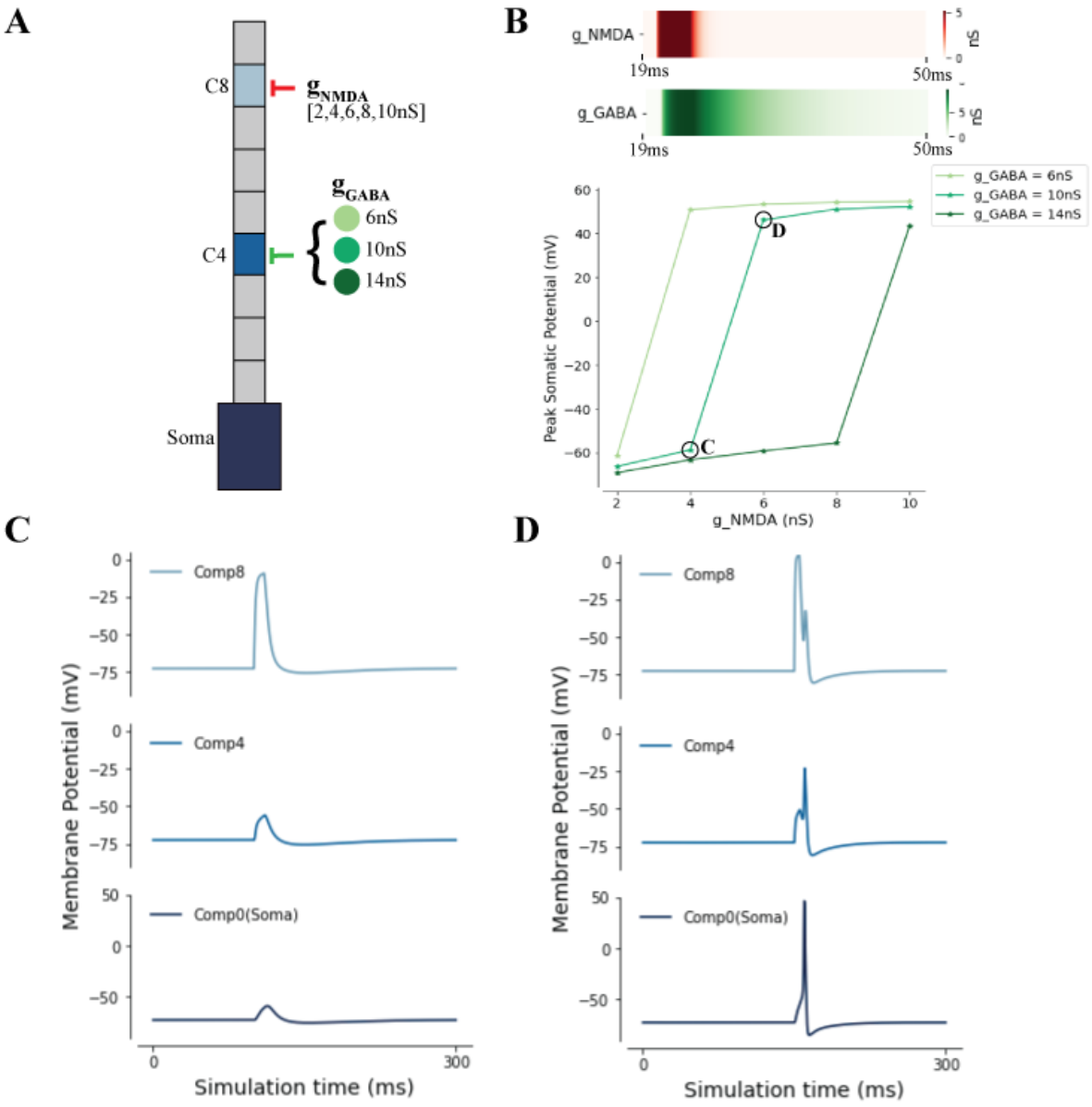

Fig. 6A: Outputs from combined excitatory and inhibitory inputs across varied synaptic conductances. **A:** Experimental setup. Extended multicompartment model including HH channels on the soma with default impermeant anion mean charge (z = -0.85) in all compartments. Excitatory glutamatergic inputs (α rate constant = $2x10^6$ $s^{-1}M^{-1}$; β rate constant = $1x10^3s^{-1}$; maximum neurotransmitter concentration = 3mM) with varied g_{NMDA} of 2nS; 4nS; 6ns; 8ns; 10nS; directed on Comp8 occurring at 50ms in 200ms simulation. At 50.01ms an inhibitory GABAergic input (α rate constant= $0.5x10^6$ $s^{-1}M^{-1}$; β rate constant = $0.1x10^3s^{-1}$; maximum neurotransmitter concentration = 3mM) with varied g_{GABA} of 6nS; 10nS; 14ns was directed on Comp4. Both synapses had a duration of 5ms.
B: Top: heatmaps showing dynamics of g_{NMDA} (red) and g_{GABA} (green). Bottom: change in peak somatic potential (mV) for each g_{NMDA} step. g_{GABA} changes are shown in different shades of green. High and low somatic potentials reflect all-or-nothing action potentials occurring if threshold voltage (-50mV) is reached.
C: Example tracings of membrane potentials in Comp8, Comp4 and Soma where threshold voltage is not reached (g_{NMDA} = 4nS; g_{GABA} = 10nS). **D:** Example tracings of membrane potentials in Comp8, Comp4 and Soma where threshold voltage is reached (g_{NMDA} = 6nS; g_{GABA} = 10nS).

3.6.2 RELATIVE EFFECTS OF IMPERMEANT ANION MEAN CHARGE AND KCC2 CONDUCTANCE ON SYNAPTIC INTEGRATION

I utilised the same multicompartmental setup with an excitatory synapse on Comp8 and an inhibitory synapse on Comp4 to compare the effect of impermeant anion mean charge and KCC2 conductance on synaptic integration. A fixed g_{GABA} of 10nS was used; while g_{NMDA} was varied between 4 and 6.5nS (these values were based on g_{NMDA} conductances on either side of the transition between subthreshold and suprathreshold excitation).

I performed the same set of simulations with 3 different values for impermeant anion mean charge (z =-0.65; z=-0.85; and z = -1.05) in Comp4 (**Fig.3.6B – A1:A4**). Despite differences in membrane potentials along the neuron, the g_{NDMA} transition point to action potential generation for all impermeant anion mean charges was 6nS.

Similarly, I then performed the same set of simulations with 3 different KCC2 strengths in Comp4 (g_{KCC2} = 2µS/cm^2 ; g_{KCC2} = 20µS/cm^2; g_{KCC2} = 80µS/cm^2) (**Fig.3.6B – B1:B4**). Compared to the altered impermeant anion mean charge experiments above, there were fewer differences in the membrane potentials of Comp4, but larger differences in Cl^- driving forces across the multicompartment model – affecting synaptic integration. At g_{KCC2} = 2µS/cm^2 , action potentials were triggered with g_{NMDA} >5.5nS; at g_{KCC2} = 20µS/cm^2 , action potentials were triggered at g_{NMDA} >6nS, and at g_{KCC2} = 80µS/cm^2 action potentials were triggered at g_{NMDA} >6.5nS.

I then further directly compared two simulations from the set above (**Fig.3.6B – C**): (1) synaptic integration with z = -1.05 and (2) with g_{KCC2} = 80µS/cm^2. Although the E_{Cl} is more hyperpolarized in Comp4 in simulation (1), E_{Cl} = -86.6 mV, relative to simulation (2), E_{Cl} = -85.2mV, action potential is triggered at the same g_{NMDA} = 6nS in simulation (1), but not in simulation (2). This "uncoupling" of E_{Cl} from action potential generation, is a direct demonstration that it is the driving force for Cl^- not the absolute E_{Cl}, that is the important variable for determining the effectiveness of synaptic inhibition

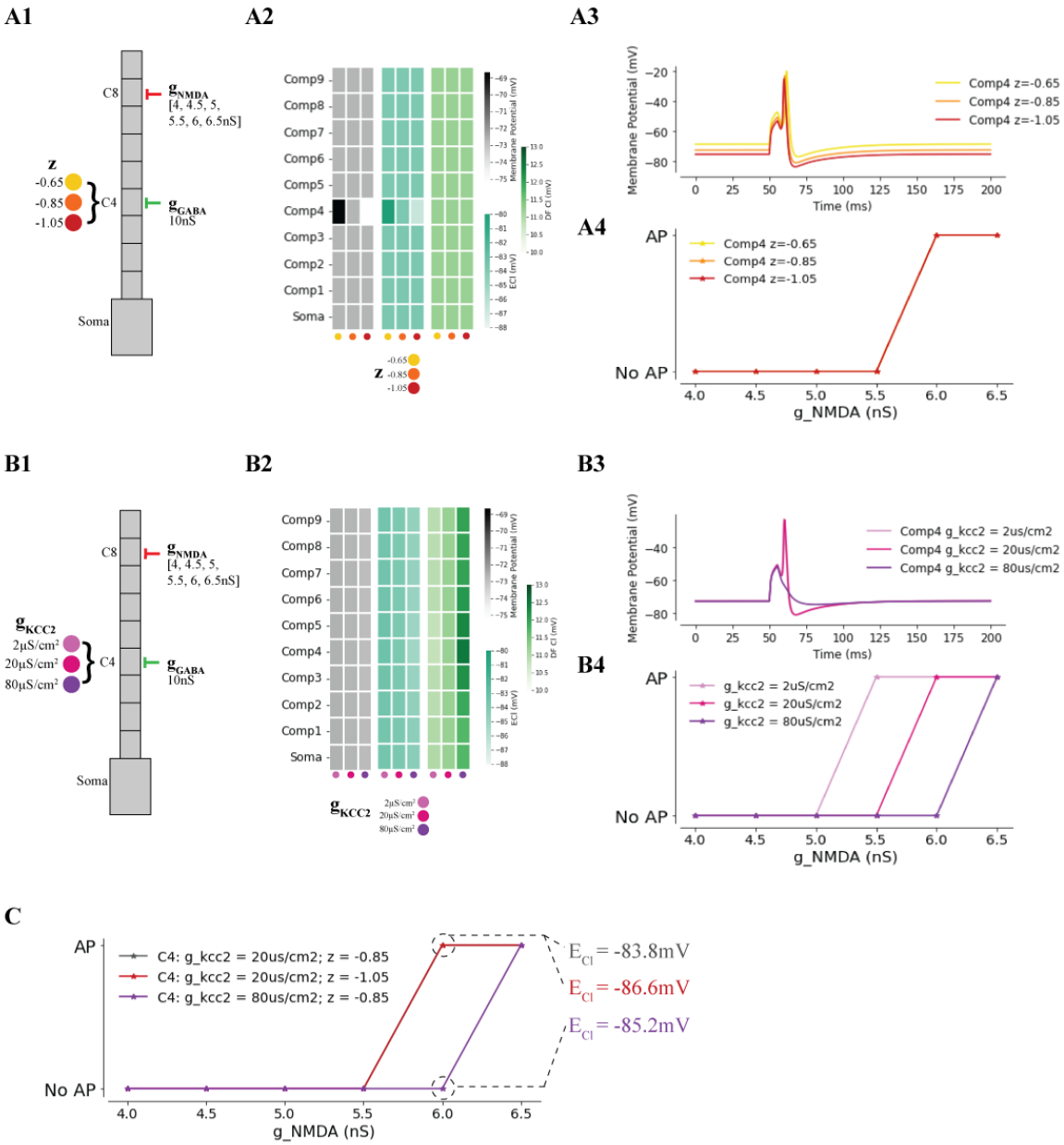

Fig. 3.6B: KCC2 conductance, and not impermeant anion mean charge affect synaptic integration. **A1:** Experimental setup. Extended multicompartment model including HH channels on the soma. Comp4 impermeant anion mean charge varied (z = -0.65: yellow; z = -0.85: orange; z = -1.05: red). Excitatory input with varied g_{NMDA} of 4nS; 4.5nS; 5ns; 5.5ns; 6nS; and 6.5nS were directed on Comp8 occurring at 50ms in 200ms simulation. At 50.01ms an inhibitory GABAergic input with g_{GABA} of 10nS was directed on Comp4. Both synapses had identical maximum neurotransmitter concentration (3mM) and duration (5ms). **B1**: Similar experimental setup, however with varied g_{KCC2} (2µS/cm²: light pink ; 20µS/cm²: dark pink ; 80µS/cm²: purple) in Comp4 instead of differences in impermeant anion mean charge. **A2 & B2:** heatmaps showing membrane potential, ECl and Cl^- DF at baseline (t=25s) for each impermeant anion mean charge and g_{KCC2} tested. **A3 & B3:** Example membrane potential tracings of Comp4 for g_{NMDA} = 6nS across impermeant anion mean charges and KCC2 conductances **A4 & B4:** Result of synaptic integration (action potential - AP- or no AP) for each g_{NMDA} step, reflect all-or-nothing action potentials occurring if threshold voltage (-50mV) is reached. **C:** Comparing action potential generation, and relative ECl values, in 3 simulations where changes were made in Comp4: grey: g_{KCC2} = 20µS/cm² , z = - 0.85; red: g_{KCC2} = 20µS/cm² , z = -1.05; purple: g_{KCC2} = 80µS/cm² , z = -1.05. Note that despite the simulation in red having a more hyperpolarized E_{Cl} at the GABAergic synapse than the purple simulation, an actional potential was generated.

4. DISCUSSION

Impermeant anions refer to negatively charged ions which are unable to traverse the cell membrane. Impermeant anion quantities and mean charge are likely to vary with metabolism as well as protein and nucleic acid synthesis/turnover; these processes are also predicted to occur at discrete spatial locations along a neuron. I developed a biophysically realistic electrodiffusion based multi-compartment neuronal model using the pump-leak framework to investigate the impact of changing impermeant anion properties at differing spatial locations (**Objective A)**.

4.1. IMPERMEANT ANION CONCENTRATION AND CHARGE SET COMPARTMENT VOLUME

I found that either increasing the absolute quantity of impermeant anions or decreasing mean charge of impermeant anions (from z = -0.85 to z = -1.05 without changing their absolute quantity) in a single compartment resulted in local compartment swelling. Both findings agree with similar biophysical models showing that cell volume is determined by both impermeant anion concentration and mean charge(Fraser and Huang, 2004; Düsterwald et al., 2018).

In our neuronal model a relatively small change in impermeant anion concentration (± 2mM, <2% increase from baseline) resulted in a substantial increase in the cell volume (± 50% increase from baseline). This large increase in volume is partly due to our method of modelling the Na/K-ATPase pump rate as constant. As the Na/K-ATPase pump rate is a crucial contributor to cell volume in addition to the Donnan Equilibrium (Kay, 2017), utilizing dynamic Na/K-ATPase pump rates would offset the large increases in volume seen with impermeant anion changes in our model (Düsterwald et al., 2018).

The relationship between impermeant anions and cell volume may help explain aspects of neuronal morphology. Considering that the machinery that constitute and produces impermeant anions occurs predominantly in regions closer to the soma, the cone-shaped morphology (large cell body with tapering dendrites) of many neurons may be due partly to a gradient of impermeant anions emanating from the soma.

4.2. LOCAL DIFFERENCES IN IMPERMEANT ANION MEAN CHARGE CAN CAUSE A PHYSIOLOGICALLY STABLE NON-ISOPOTENTIAL DENDRITE

Objective B of this thesis was to investigate the electrical effects of impermeant anions on neurons. **Result 3.1** shows that modifying the absolute quantity of impermeant anions without altering mean charge ("X-flux") in a single compartment did not change steady state membrane potential or ionic reversal potential in that compartment. Increased impermeant anion quantity only resulted in increased compartment volumes, which ensured that steady state ion concentrations, including that of impermeant anions remained stable. Unlike in **Fig.4.1** proposed by (Delpire and Staley, 2014), as permeant ion concentrations were unaffected by increases in impermeant anion quantity there were no alterations to membrane potential or ionic reversal potentials. Hence E_{GABA} (which is predominantly based on E_{Cl}) did not change.

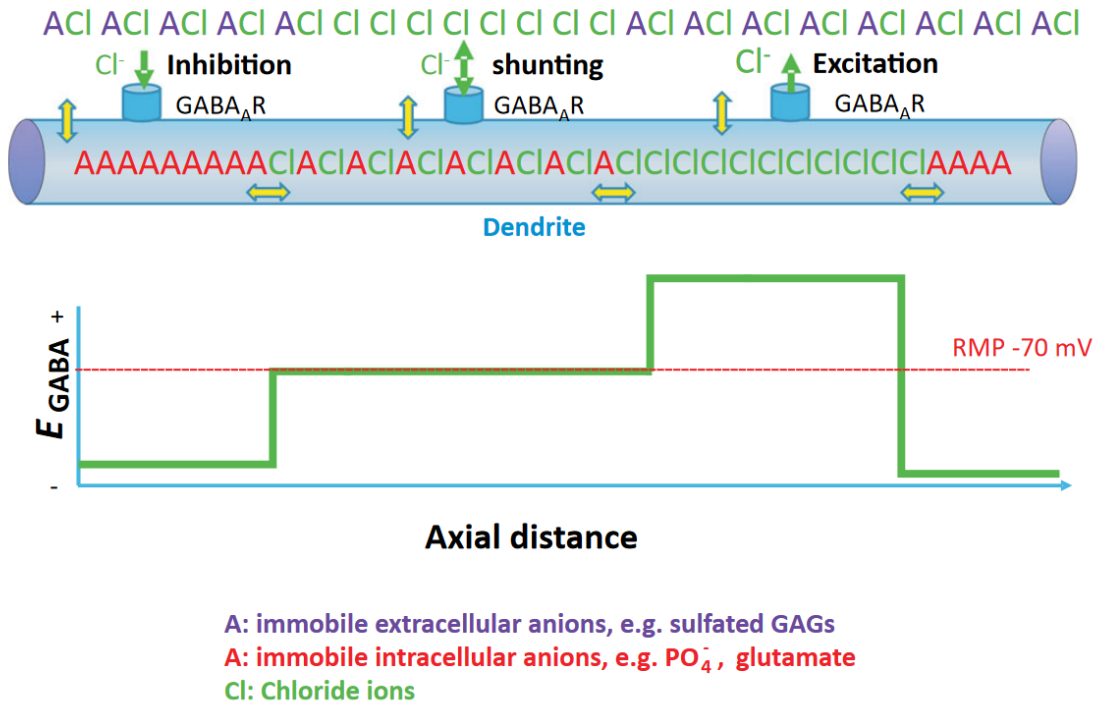

Fig. 4.1: Effect of local changes to impermeant anion concentration on neuronal physiology according to Delpire & Staley (2014)

When altering impermeant anion mean charge, the membrane potential and ionic reversal potentials of the compartment were affected (**Result 3.2**). Decreasing impermeant mean charge in a single compartment, resulted in a local drop in membrane potential, and new steady state ion concentrations. In other compartments, membrane potential and ion concentrations remained the same. Therefore, non-uniform impermeant anion mean charge across compartments resulted in a non-isopotential dendrite.

Ionic reversal potentials shifted simultaneously, and in equal magnitude, to decreases in membrane potential. Drops in both ionic reversal potential and membrane potential meant that ionic driving forces were unaffected. **Fig4.2.** demonstrates these findings and compares the conclusions reached in this thesis with that postulated by Delpire & Staley (**Fig 4.1**). Differences in impermeant anion mean charge between compartments resulted in equal but opposite boundary potentials and boundary ionic reversal potentials, which meant that no boundary driving force was established.

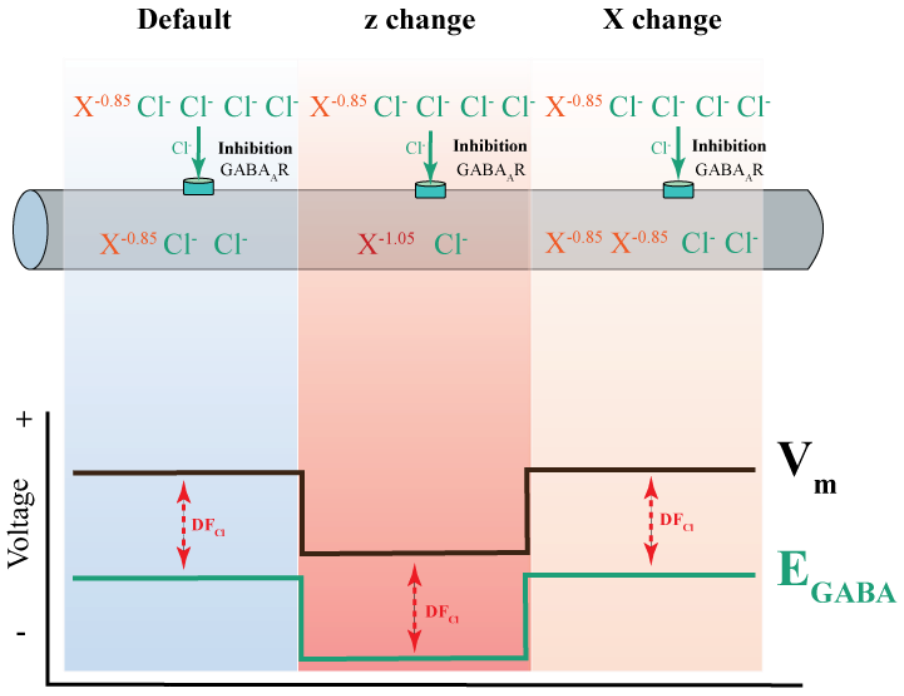

Fig 4.2: Electrical effects of spatial differences in impermeant anion charge (z) and concentration (X) along a dendrite. No changes to Cl^- driving forces (DF_{Cl}) occurred due to identical shifts in E_{Cl} and V_m accompanying modifications in impermeant anion mean charge. Constant DF_{Cl} resulted in equal inhibition at each region along the dendrite.

This means that at steady state, without any input of energy dendrites can maintain different local membrane potentials and ionic reversals potentials. However, this does not result in a constant net flux of ions between compartments as boundary driving forces are zero.

I then looked to compare these effects across a range of impermeant anion mean charges (z = -0.65 to z = -1.05) (**Result 3.3**). I found that impermeant anion mean charge is inversely proportional to compartment volume and directly proportional to impermeant anion concentration (decreasing impermeant mean charge without changing the absolute number of molecules results in compartment swelling, thereby decreasing impermeant anion concentration). I observed non-linear relationships between impermeant anion mean charge and permeant ion concentration, most prominently with Cl^-.

Despite non-linear changes in ion concentrations, transmembrane ionic driving forces across the range of impermeant anion mean charge values were identical. The greater the absolute difference between impermeant mean charge in one compartment compared to its neighbouring compartments, the greater the axial boundary potentials were. However, across the spectrum of impermeant anion mean charge investigated, no boundary driving forces were established. These results were replicated when multiple impermeant anion mean charge changes were established within a dendrite.

4.3. IONIC MICRODOMAINS IN NON-ISOPOTENTIAL DENDRITES

I demonstrated that ionic microdomains (local areas within cells that have differing ion concentrations to neighbouring regions) can occur due to spatial differences in impermeant anion mean charge. This is possible without active ion transport using energy to maintain ion gradients because a balance of chemical and electrical forces is maintained. To simplify this finding, consider a hypothetical scenario of a dendrite with three compartments (A, B and C), where in compartment B impermeant anion mean charge has been reduced to z = -1.05 resulting in a ionic microdomain with reduced Cl^- (**Fig4.3**).

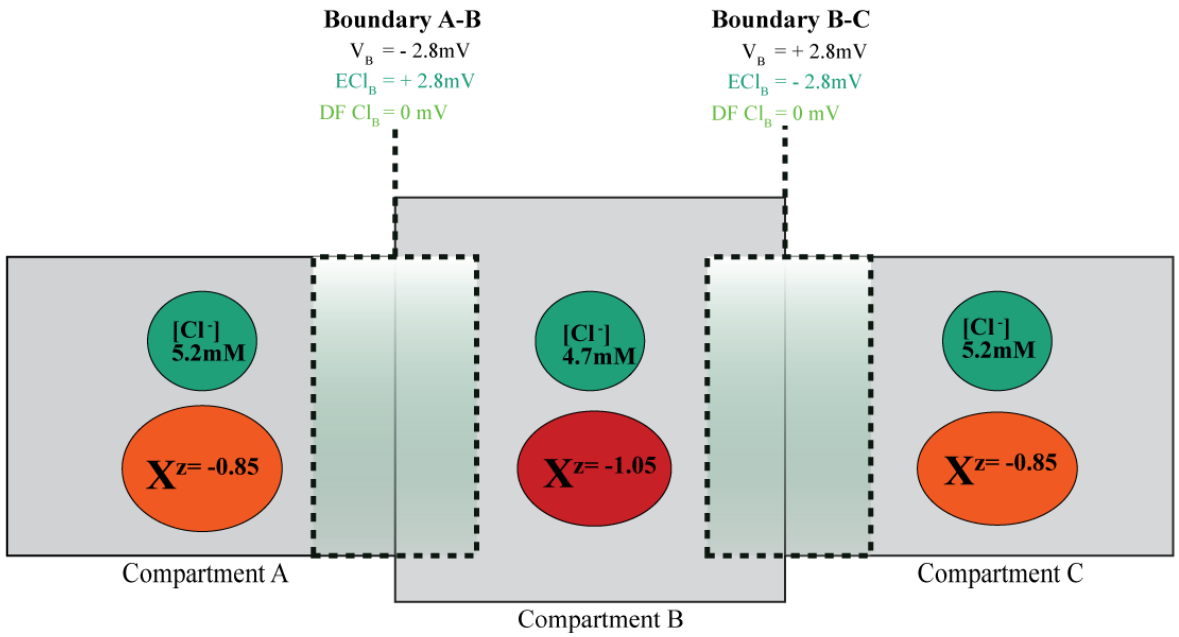

Fig. 4.3: Boundary interactions maintaining chloride microdomains. Impermeant anion mean charge discrepancy in Compartment B, leads to compartment swelling and a Cl^- microdomain. Equal but opposite boundary potentials (V_B) and boundary chloride reversal potentials (ECl_B) develop such that there is no boundary Cl^- driving force (DF Cl_B) at either boundary.

In this scenario, examining the boundaries between compartments is a useful way to understand the forces involved. Across boundary A-B and boundary B-C, there is a Cl^- concentration gradient, reflected as a boundary reversal potential (ECl_B) that differs in direction at each boundary. Although considered as a 'force', diffusion down concentration gradients reflects the stochastic process of increasing entropy (Einstein, 1905), hence no free energy per mole is required (Hille, 2001).

In the opposite direction, an electrostatic force occurs due to the charge separation between impermeant anions of different mean charge – referred to as the boundary potential (V_B).

At steady state these opposing potentials are equal such that the boundary driving force for Cl^- (DF Cl_B) is zero; therefore, I suggest that a non-isopotential neuron with ionic microdomains can be physiologically stable as there is no change in the energy expenditure of the cell.

Although no experimental work has yet proven that altering impermeant anion mean charge can result in an ionic microdomains, (Rahmati et al., 2021) demonstrate that Cl^- microdomains (and corresponding variances in E_{GABA}) occur in murine dendrites, while further suggesting that impermeant anion differences, rather than CCCs, are responsible. The multicompartment model developed in this thesis (with fixed KCC2 conductances) supports this experimental finding by demonstrating that maintenance of Cl^- microdomains can be independent of chloride cotransporter activity.

This thesis however disagrees with (Rahmati et al., 2021) regarding the relationship between impermeant anions and dendritic morphology. In (Rahmati et al., 2021) actin depolymerization (i.e., a disturbance to impermeant anions) was sufficient to cause a change in Cl^- microdomains yet dendritic morphology was unaffected. Our multicompartmental model predicts that altering either impermeant anion concentration or mean charge would impact dendritic morphology (as shown by the swollen compartment in **Fig4.3**). Possible reasons for this discrepancy include: 1) my model did not consider axial volume changes, and 2) the compartments defined in our model were on a larger spatial scale (20µm X 1 µm) than the spatial scale used in the experimental setup (± 0.1 µm X 0.1 µm), where experimentally measuring changes to compartment volumes would be challenging. This is not the only contention this thesis makes with the current literature.

(Rahmati et al., 2021) also claim that impermeant anions not only establish Cl^- microdomains but can also shift the effect of GABAergic signalling i.e., modify Cl^- driving force as demonstrated in **Fig4.1**. My biophysical modelling framework contends that this is unlikely to be the case. Altering impermeant anions cannot directly alter Cl^- driving force or the effectiveness of inhibition.

4.4. PASSIVE CABLE PROPERTIES OF NON-ISOPOTENTIAL DENDRITES

Objective C of this thesis entailed investigating the passive cable properties of non-isopotential dendrites. I firstly validated my electrodiffusion based biophysical multicompartment model based on the pump-leak mechanism created in this thesis to a similar equivalent circuit based isopotential model created in NEURON (Hines and Carnevale, 2001) (**Result 3.4**). To achieve comparatively similar membrane length and time constants to the NEURON based model I halved the electrodiffusion constants used in other studies (Qian and Sejnowski, 1989; Düsterwald et al., 2018).

An incidental additional finding from this thesis may be the improved approximation of ionic electrodiffusion constants. The electrodiffusion constants by (Hille, 2001) are based upon ionic diffusion in water however diffusion through neuronal cytoplasm is likely different. Further research, perhaps using a similar comparative method as used in this thesis, is needed to predict these constants more accurately.

As I have shown that impermeant anions do not affect ionic driving forces in the transmembrane or axial planes, I would not expect impermeant anions in non-isopotential dendrites to alter the passive signalling properties of neurons. Indeed, simulations with modified impermeant anion mean charge at a single location only modestly affected the time and length constants (1-4% change). These slight differences may be related to the curve fitting procedures, or due to the artificial volume normalization procedure I employed.

4.5. IMPERMEANT ANIONS DO NOT ALTER SYNAPTIC TRANSMISSION AND INTEGRATION

Objective D of this thesis was to investigate how altering the properties of impermeant anions could modify the effect of synaptic input. To this end, no differences to the somatic potential were observed when subthreshold excitatory inputs were directed onto compartments with altered impermeant anion mean charge (**Result 3.5)**. Impermeant anions modified between the synaptic origin and the soma, and at the soma itself, did not alter synaptic potentials. Similarly, inhibitory synaptic potentials were unaffected by altering the properties of impermeant anions.

I next investigated the influence of impermeant anions on synaptic integration (**Objective E**) or the effectiveness of synaptic inhibition to prevent action potential generation. In **Result 3.6**, excitatory and inhibitory inputs were both incorporated in simulations with modified impermeant anion mean charge. Altering impermeant anion mean charge had no impact on synaptic integration, irrespective of the strength of inhibitory and excitatory synapses. That is, despite differing mean charges of impermeant anions altering the local Cl^- reversal potentials in dendritic compartments that received GABAergic synaptic input, there was no effect on the ability of synaptic inhibition to prevent action potential generation. Therefore, in my model altering impermeant anion mean charge had no impact on synaptic integration.

Lastly a comparison between varying impermeant anions and altering the activity of the cation-chloride cotransporter KCC2 was made. By decreasing impermeant anion mean charge, E_{Cl} was reduced to -86.6mV, whilst in as separate simulation increasing KCC2 activity in the same compartment caused a reduction of E_{Cl} to -85.2 mV. Despite a more depolarized $E_{Cl,}$ the increase to KCC2 activity was able to suppress an action potential at g_{NMDA} = 6nS, whilst the simulation with decreased impermeant anion mean charge could not. This phenomenon is explained by the fact that changes to KCC2 impacted Cl^- driving force which was not the case when impermeant anion mean charge was modified. In summary, Cl^- driving force – not E_{Cl} – underpins the function of inhibitory signalling.

4.6. MODEL LIMITATIONS

To isolate the direct potential effects of impermeant anions on membrane potential, ion concentrations, ion reversal potentials and driving force my model was simplified in four ways: keeping surface area constant (and hence not scaling transmembrane ion channel conductances); utilizing a static ATPase rate; normalizing compartment volume in a non-physiological manner (in the later results); and assuming a fixed extracellular ionic bath. I don't believe these simplifications are likely to have had a bearing on the broad conclusions of this thesis.

One aspect not explored was the impact of impermeant anions on voltage dependant conductances. Alterations to impermeant anion average charge affects membrane potential but ionic driving forces remain the same. Therefore, I believe that the likelihood of voltage dependent channel opening would be impacted by altered impermeant anion average charge,

however the effect of channel opening (magnitude and direction of ion flux) would remain the same. Further simulations should be performed to investigate this hypothesis.

Another limitation to maintain model simplicity and efficiency of computational time was the omittance of $HCO3^-$ ions both in general neuronal ion dynamics and in relation to modelling GABAergic synapses. Moreover, I did not directly model the changes that occur to the pH of a cell when impermeant anions changed, nor how changes in pH might alter the mean charge of impermeant anions.

Another limitation could be the method of modelling electrodiffusion I used. I employed a 1-dimensional electrodiffusion based model (Qian and Sejnowski, 1989), however in reality electrodiffusion occurs in 3-dimensions across multiple electrical fields in neurons (Savtchenko et al., 2017). Furthermore, precise ion diffusion coefficients through cytoplasm are unknown, and approximations were used based on ionic movement through water.

Using the multicompartment model I reach the conclusion that neurons can be non-isopotential at steady state. This conclusion is contingent on modelling all impermeant anions as fixed constituents within a compartment. In living neurons this is not the case as proteins and other impermeant anions display cytosolic motion. However, it is still likely that there are larger molecules which cannot move and are relatively fixed in space. There are no mathematical models of axial macromolecular flux present in the literature. Moreover, impermeant macromolecules likely contribute to the axial resistance of the neuron and this was not explicitly modelled.

4.7. Clinical implications of impermeant anion physiology

Impermeant anions accumulate in several neurodegenerative disorders such as Alzheimer's, and Parkinson's disease (Goedert et al., 2017; Schaffert and Carter, 2020). These disorders are associated with a host of aberrant neuronal signalling patterns. I show that differences to impermeant anion concentration and charge do not impact synaptic integration and action potential generation, I therefore hypothesize that neuronal dysfunction in these disorders are likely from cytotoxic effects of the abnormal proteins rather than direct electrical effects on the neurons.

Impermeant anions and the Na/K^-ATPase play an important role in regulating neuronal volume. In ischaemic conditions (such as stroke), ATP depletion occurs due to cessation of aerobic metabolism. Under these conditions, impermeant anions left unchecked result in

further cell swelling, raised intracranial pressure, and cell death in a self-perpetuating cycle (Pasantes-Morales et al., 2000; Elkin et al., 2010). Speculatively, alternative methods of reducing intracranial pressure, perhaps by modifying impermeant anion mean charge could reduce the reliance on invasive treatments such as decompressive craniotomies.

4.8. FUTURE DIRECTIONS

To validate findings of my computational model, experimental work should be performed. The recent development of genetically encoded voltage indicators (Yang and St-Pierre, 2016) may be useful in providing experimental evidence that subcellular non-isopotential voltage compartments occur in resting neurons. Perhaps this could be combined with other techniques used to localize proteins such as Multiplexed Protein Maps (Gut et al., 2018) to investigate whether there is a colocalization between protein distribution and non-isopotential voltage compartments. This suggestion would still be limited by the fact that there are currently no experimental techniques to determine impermeant anion mean charge in dendritic compartments. Furthermore, currently available genetically encoded voltage indicators are not ratiometric and cannot report absolute membrane potential.

To build on our model, I could include changes occurring to the extracellular matrix (ECM) which has been shown to play a role in both cell volume regulation and Cl^- homeostasis (Glykys et al., 2017). Degradation of ECM occurs in many pathological states (Cui et al., 2013), however the effects of ECM degradation on the signalling properties of neurons are unclear. Moreover, altered pH that occurs in several pathologies relating to acidosis may affect extracellular protein mean charge. How this affects signalling is also unknown, though could be computationally simulated by better incorporating HCO_3^- and H^+ into the model.

Adding greater complexity to how CCCs are modelled would be another way to represent neural physiology more accurately. Some studies have shown that in addition to ion transport, CCCs may be involved in water flux and the response to osmotic challenges (Boettger, 2003; Bergeron et al., 2006; Blaesse et al., 2009). Although whether CCCs are themselves permeable to water, or that water itself is involved in the energetics of ion transport is disputed (Kaila et al., 2014). Incorporating another major CCC in neurons, NKCC1 (Na-K-Cl cotransporter), may better resolve the function of CCCs in Cl^- homeostasis and neural inhibition.

Improvements could also be made to the method of modelling electrodiffusion. The model by (Mori, 2015) is more comprehensive than the model used in this thesis by simulating osmotic fluxes as well as ion fluxes between neurons, glial cells and the extracellular fluid in a series of partial differential equations. This model may be more useful for studying disease states (such as cortical spreading depression that has known glial and extracellular changes), however in the case of this thesis I look at inhibition more broadly and thus my simplified model is likely more appropriate

Future studies could also consider adapting the Poisson-Nernst-Plank (PNP) electrodiffusion approach of modelling axons (Pods et al., 2013; Boahen and Doyon, 2020), to a dendritic model. This would prevent any assumptions in the model by calculating the electric field from first principles at each time step. The PNP technique is however highly computationally expensive and would require greater improvements in computing power than that currently available. Moreover the PNP technique does not account for water fluxes.

Models with increased morphological and synaptic complexity would also provide better approximations to real neurons. In this thesis I placed a singular synaptic input at the distal portion of a linear dendrite and vary the spatial location of impermeant anions; in reality, neurons have multiple dendrites receiving several inputs (Adrian and Zotterman, 1926). The spatial location of inhibitory synapses is known to affect firing rates of neurons and Cl^- concentrations along dendrites (Currin et al., 2020), however, whether impermeant anions alter these properties is unknown and would require more complex models.

4.9. CONCLUSION

Both the absolute quantity of impermeant anions and their mean charge are principal components in setting neuronal volume. Non-uniform distributions of impermeant anion mean charge (but not absolute quantity) result in physiologically stable non-isopotential neurons with ionic microdomains. At steady state these discrepancies in local membrane potentials and ion concentrations do not impact the passive or active electrical properties of neurons. Neural signalling is a function of ionic driving forces, which are maintained at irrespective of impermeant anion mean charge by active or secondary active transport mechanisms. These findings explain how electrical signalling remains consistent in the face of an ever-changing impermeant anion milieu with implications related to our understanding of both normal and pathological neuronal physiology.

5. REFERENCES

Abbott J, Davson H, Glen I, Grant N (1971) Chloride transport and potential across the blood-CSF barrier. Brain Research 29:185–193.

Adrian ED, Zotterman Y (1926) The impulses produced by sensory nerve endings: Part 3. Impulses set up by Touch and Pressure. J Physiol 61:465–483.

Alfonsa H, Merricks EM, Codadu NK, Cunningham MO, Deisseroth K, Racca C, Trevelyan AJ (2015) The Contribution of Raised Intraneuronal Chloride to Epileptic Network Activity. Journal of Neuroscience 35:7715–7726.

Barmashenko G, Hefft S, Aertsen A, Kirschstein T, Köhling R (2011) Positive shifts of the GABAA receptor reversal potential due to altered chloride homeostasis is widespread after status epilepticus. Epilepsia 52:1570–1578.

Ben-Ari Y (2002) Excitatory actions of gaba during development: the nature of the nurture. Nature Reviews Neuroscience 3:728–739.

Bergeron MJ, Gagnon E, Caron L, Isenring P (2006) Identification of key functional domains in the C terminus of the K+-Cl- cotransporters. J Biol Chem 281:15959–15969.

Blaesse P, Airaksinen MS, Rivera C, Kaila K (2009) Cation-Chloride Cotransporters and Neuronal Function. Neuron 61:820–838.

Blaustein MP, Kao JPY, Matteson DR, Blaustein MP eds. (2012) Cellular physiology and neurophysiology, 2nd ed. Philadelphia, PA: Elsevier/Mosby.

Boahen F, Doyon N (2020) Modelling dendritic spines with the finite element method, investigating the impact of geometry on electric and calcic responses. J Math Biol 81:517–547.

Boettger T (2003) Loss of K-Cl co-transporter KCC3 causes deafness, neurodegeneration and reduced seizure threshold. The EMBO Journal 22:5422–5434.

Brumback AC, Staley KJ (2008) Thermodynamic Regulation of NKCC1-Mediated Cl- Cotransport Underlies Plasticity of GABAA Signaling in Neonatal Neurons. Journal of Neuroscience 28:1301–1312.

Burton RF (1983) The composition of animal cells: solutes contributing to osmotic pressure and charge balance. Comparative Biochemistry and Physiology Part B: Comparative Biochemistry 76:663–671.

Coombs JS, Eccles JC, Fatt P (1955) The specific ionic conductances and the ionic movements across the motoneuronal membrane that produce the inhibitory post-synaptic potential. The Journal of Physiology 130:326–373.

Cui H, Freeman C, Jacobson GA, Small DH (2013) Proteoglycans in the central nervous system: Role in development, neural repair, and Alzheimer's disease. IUBMB Life 65:108–120.

Currin CB, Trevelyan AJ, Akerman CJ, Raimondo JV (2020) Chloride dynamics alter the input-output properties of neurons Berry H, ed. PLoS Comput Biol 16:e1007932.

Deitcher Y, Eyal G, Kanari L, Verhoog MB, Atenekeng Kahou GA, Mansvelder HD, de Kock CPJ, Segev I (2017) Comprehensive Morpho-Electrotonic Analysis Shows 2 Distinct Classes of L2 and L3 Pyramidal Neurons in Human Temporal Cortex. Cerebral Cortex 27:5398–5414.

Delpire E, Staley KJ (2014) Novel determinants of the neuronal Cl− concentration. The Journal of Physiology 592:4099–4114.

Destexhe A, Mainen ZF, Sejnowski TJ (1993) An Efficient Method for Computing Synaptic Conductances Based on a Kinetic Model of Receptor Binding. :4.

Destexhe A, Mainen ZF, Sejnowski TJ (n.d.) 1 Introduction: the kinetic interpretation of ion channel gating. :30.

Doyon N, Prescott SA, Castonguay A, Godin AG, Kröger H, De Koninck Y (2011) Efficacy of Synaptic Inhibition Depends on Multiple, Dynamically Interacting Mechanisms Implicated in Chloride Homeostasis Morrison A, ed. PLoS Comput Biol 7:e1002149.

Doyon N, Vinay L, Prescott SA, De Koninck Y (2016) Chloride Regulation: A Dynamic Equilibrium Crucial for Synaptic Inhibition. Neuron 89:1157–1172.

Düsterwald KM, Currin CB, Burman RJ, Akerman CJ, Kay AR, Raimondo JV (2018) Biophysical models reveal the relative importance of transporter proteins and impermeant anions in chloride homeostasis. eLife 7:e39575.

Einstein A (1905) Investigations on The Theory of Brownian Motion. :11.

Elkin BS, Shaik MA, Morrison B (2010) Fixed negative charge and the Donnan effect: a description of the driving forces associated with brain tissue swelling and oedema. Phil Trans R Soc A 368:585–603.

Ellingsrud AJ, Solbrå A, Einevoll GT, Halnes G, Rognes ME (2020) Finite Element Simulation of Ionic Electrodiffusion in Cellular Geometries. Front Neuroinform 14:11.

Eyal G, Verhoog MB, Testa-Silva G, Deitcher Y, Benavides-Piccione R, DeFelipe J, de Kock CPJ, Mansvelder HD, Segev I (2018) Human Cortical Pyramidal Neurons: From Spines to Spikes via Models. Front Cell Neurosci 12:181.

Eyal G, Verhoog MB, Testa-Silva G, Deitcher Y, Lodder JC, Benavides-Piccione R, Morales J, DeFelipe J, de Kock CP, Mansvelder HD, Segev I (2016) Unique membrane properties and enhanced signal processing in human neocortical neurons. eLife 5:e16553.

Fraser JA, Huang CL-H (2004) A quantitative analysis of cell volume and resting potential determination and regulation in excitable cells: Quantitative relationships between cell volume and resting potential. The Journal of Physiology 559:459–478.

Gianazza, E, Righetti PG (1980) Size and Charge Distribution of Macromolecules in Living Systems. Journal of Chromatography 193:1–8.

Glykys J, Dzhala V, Egawa K, Balena T, Saponjian Y, Kuchibhotla KV, Bacskai BJ, Kahle KT, Zeuthen T, Staley KJ (2014a) Local Impermeant Anions Establish the Neuronal Chloride Concentration. Science 343:670–675.

Glykys J, Dzhala V, Egawa K, Balena T, Saponjian Y, Kuchibhotla KV, Bacskai BJ, Kahle KT, Zeuthen T, Staley KJ (2014b) Response to Comments on "Local impermeant anions establish the neuronal chloride concentration." Science 345:1130–1130.

Glykys J, Dzhala V, Egawa K, Kahle KT, Delpire E, Staley K (2017) Chloride Dysregulation, Seizures, and Cerebral Edema: A Relationship with Therapeutic Potential. Trends in Neurosciences 40:276–294.

Goedert M, Eisenberg DS, Crowther RA (2017) Propagation of Tau Aggregates and Neurodegeneration. Annu Rev Neurosci 40:189–210.

Gut G, Herrmann MD, Pelkmans L (2018) Multiplexed protein maps link subcellular organization to cellular states. Science 361:eaar7042.

H Chiel, Gill J (2022) Hodgkin Huxley Model Parameters. Hodgkin Huxley Model Parameters Available at: https://neurowiki.case.edu/wiki/HodgkinHuxleyModelParameters [Accessed June 3, 2022].

Hernández JA, Cristina E (1998) Modeling cell volume regulation in nonexcitable cells: the roles of the Na^+ pump and of cotransport systems. American Journal of Physiology-Cell Physiology 275:C1067–C1080.

Herz AVM, Gollisch T, Machens CK, Jaeger D (2006) Modeling Single-Neuron Dynamics and Computations: A Balance of Detail and Abstraction. Science 314:80–85.

Hille B (2001) Ion Channels of Excitable Membranes, 3rd ed. MA, USA: Sinauer Associates Inc.

Hines ML, Carnevale NT (2001) Neuron: A Tool for Neuroscientists. Neuroscientist 7:123–135.

Hodgkin AL, Huxley AF (1952) A quantitative description of membrane current and its application to conduction and excitation in nerve. The Journal of Physiology 117:500–544.

Hsu Y-T, Chang Y-G, Chern Y (2018) Insights into GABAergic system alteration in Huntington's disease. Open Biol 8:180165.

Johnston D, Wu SM (1995) Foundations of cellular neurophysiology. Cambridge, Mass: MIT Press.

Kager H, Wadman WJ, Somjen GG (2000) Simulated seizures and spreading depression in a neuron model incorporating interstitial space and ion concentrations. J Neurophysiol 84:495–512.

Kahle KT, Khanna AR, Alper SL, Adragna NC, Lauf PK, Sun D, Delpire E (2015) K-Cl cotransporters, cell volume homeostasis, and neurological disease. Trends in Molecular Medicine 21:513–523.

Kaila K (1992) Ionic Basis of GABA-A Receptor Channel Function in the Nervous System. Progress in Neurobiology 42:489–537.

Kaila K, Price TJ, Payne JA, Puskarjov M, Voipio J (2014) Cation-chloride cotransporters in neuronal development, plasticity and disease. Nat Rev Neurosci 15:637–654.

Kay AR (2017) How Cells Can Control Their Size by Pumping Ions. Front Cell Dev Biol 5:41.

Keener J, Sneyd J eds. (2009) Mathematical Physiology. New York, NY: Springer New York. Available at: http://link.springer.com/10.1007/978-0-387-75847-3 [Accessed May 29, 2022].

Koleske AJ (2013) Molecular mechanisms of dendrite stability. Nat Rev Neurosci 14:536–550.

Lee HHC, Deeb TZ, Walker JA, Davies PA, Moss SJ (2011) NMDA receptor activity downregulates KCC2 resulting in depolarizing GABAA receptor-mediated currents. Nat Neurosci 14:736–743.

Liu Y, Garnham CP, Roll-Mecak A, Tanner ME (2013) Phosphinic acid-based inhibitors of tubulin polyglutamylases. Bioorg Med Chem Lett 23:4408–4412.

Lodish H, Berk A, Zipursky S, Matsudaira P, Baltimore D, Darnell J (2009) Intracellular Ion Environment and Membrane Electric Potential. In: Molecular Cell Biology, 4th ed. New York, NY.

Lopreore CL, Bartol TM, Coggan JS, Keller DX, Sosinsky GE, Ellisman MH, Sejnowski TJ (2008) Computational Modeling of Three-Dimensional Electrodiffusion in Biological Systems: Application to the Node of Ranvier. Biophysical Journal 95:2624–2635.

Markram H et al. (2015) Reconstruction and Simulation of Neocortical Microcircuitry. Cell 163:456–492.

McDougal RA, Morse TM, Carnevale T, Marenco L, Wang R, Migliore M, Miller PL, Shepherd GM, Hines ML (2017) Twenty years of ModelDB and beyond: building essential modeling tools for the future of neuroscience. J Comput Neurosci 42:1–10.

Mohapatra N, Tønnesen J, Vlachos A, Kuner T, Deller T, Nägerl UV, Santamaria F, Jedlicka P (2016) Spines slow down dendritic chloride diffusion and affect short-term ionic plasticity of GABAergic inhibition. Sci Rep 6:23196.

Mori Y (2015) A multidomain model for ionic electrodiffusion and osmosis with an application to cortical spreading depression. Physica D: Nonlinear Phenomena 308:94–108.

Morón JA, Devi LA (2007) Use of proteomics for the identification of novel drug targets in brain diseases. J Neurochem 102:306–315.

Pasantes-Morales H, Franco R, Torres-Marquez ME, Hernández-Fonseca K, Ortega A (2000) Amino Acid Osmolytes in Regulatory Volume Decrease and Isovolumetric Regulation in Brain Cells: Contribution and Mechanisms. Cell Physiol Biochem 10:361–370.

Podlaski WF, Seeholzer A, Groschner LN, Miesenböck G, Ranjan R, Vogels TP (2017) Mapping the function of neuronal ion channels in model and experiment. eLife 6:e22152.

Pods J, Schönke J, Bastian P (2013) Electrodiffusion Models of Neurons and Extracellular Space Using the Poisson-Nernst-Planck Equations—Numerical Simulation of the Intra- and Extracellular Potential for an Axon Model. Biophysical Journal 105:242–254.

Qian N, Sejnowski TJ (1989) An electro-diffusion model for computing membrane potentials and ionic concentrations in branching dendrites, spines and axons. Biol Cybern 62:1–15.

Rahmati N, Normoyle KP, Glykys J, Dzhala VI, Lillis KP, Kahle KT, Raiyyani R, Jacob T, Staley KJ (2021) Unique Actions of GABA Arising from Cytoplasmic Chloride Microdomains. J Neurosci 41:4957–4975.

Raimondo JV, Burman RJ, Katz AA, Akerman CJ (2015) Ion dynamics during seizures. Front Cell Neurosci 9 Available at: http://journal.frontiersin.org/Article/10.3389/fncel.2015.00419/abstract [Accessed May 9, 2022].

Raimondo JV, Richards BA, Woodin MA (2017) Neuronal chloride and excitability — the big impact of small changes. Current Opinion in Neurobiology 43:35–42.

Rivera C, Voipio J, Payne JA, Ruusuvuori E, Lahtinen H, Lamsa K, Pirvola U, Saarma M, Kaila K (1999) The K+/Cl- co-transporter KCC2 renders GABA hyperpolarizing during neuronal maturation. Nature 397:251–255.

Savtchenko LP, Poo MM, Rusakov DA (2017) Electrodiffusion phenomena in neuroscience: a neglected companion. Nat Rev Neurosci 18:598–612.

Schaffert L-N, Carter WG (2020) Do Post-Translational Modifications Influence Protein Aggregation in Neurodegenerative Diseases: A Systematic Review. Brain Sci 10:E232.

Solbrå A, Bergersen AW, van den Brink J, Malthe-Sørenssen A, Einevoll GT, Halnes G (2018) A Kirchhoff-Nernst-Planck framework for modeling large scale extracellular electrodiffusion surrounding morphologically detailed neurons Barreto E, ed. PLoS Comput Biol 14:e1006510.

Sperelakis N (2012) Gibbs–Donnan Equilibrium Potentials. In: Cell Physiology Source Book, pp 147–151. Elsevier. Available at: https://linkinghub.elsevier.com/retrieve/pii/B978012387738300010X [Accessed May 9, 2022].

Szabadics J, Varga C, Molnár G, Oláh S, Barzó P, Tamás G (2006) Excitatory Effect of GABAergic Axo-Axonic Cells in Cortical Microcircuits. Science 311:233–235.

Tang D, Qian A-H, Song D-D, Ben Q-W, Yao W-Y, Sun J, Li W-G, Xu T-L, Yuan Y-Z (2015) Role of the potassium chloride cotransporter isoform 2-mediated spinal chloride homeostasis in a rat model of visceral hypersensitivity. Am J Physiol Gastrointest Liver Physiol 308:G767-778.

Taylor SF, Tso IF (2015) GABA abnormalities in schizophrenia: A methodological review of in vivo studies. Schizophr Res 167:84–90.

Thul PJ et al. (2017) A subcellular map of the human proteome. Science 356:eaal3321.

Tosteson DC, Hoffman JF (1960) Regulation of Cell Volume by Active Cation Transport in High and Low Potassium Sheep Red Cells. Journal of General Physiology 44:169–194.

Trappenberg TP (2010) Fundamentals of computational neuroscience, 2nd ed. Oxford ; New York: Oxford University Press.

Vardi N, Zhang LL, Payne JA, Sterling P (2000) Evidence that different cation chloride cotransporters in retinal neurons allow opposite responses to GABA. J Neurosci 20:7657–7663.

Voipio J, Boron WF, Jones SW, Hopfer U, Payne JA, Kaila K (2014) Comment on "Local impermeant anions establish the neuronal chloride concentration." Science 345:1130–1130.

Yang HH, St-Pierre F (2016) Genetically Encoded Voltage Indicators: Opportunities and Challenges. J Neurosci 36:9977–9989.

Zhang R, Zhang S, Du J (2013) KCC2-dependent subcellular ECl difference of ON-OFF retinal ganglion cells in larval zebrafish. Frontiers in Neural Circuits 7 Available at: https://www.frontiersin.org/article/10.3389/fncir.2013.00103 [Accessed June 9, 2022].

Zhou Y (2005) A Model for Interaural Time Difference Sensitivity in the Medial Superior Olive: Interaction of Excitatory and Inhibitory Synaptic Inputs, Channel Dynamics, and Cellular Morphology. Journal of Neuroscience 25:3046–3058.

6. APPENDIX

6.1. VOLUME NORMALIZATION PROCEDURE

To isolate the potential effects of impermeant anions independent of volume change I normalized the volume of compartments were impermeant anions were manipulated in simulation from Results section 3.4 onwards.

Step 1: Calculate the average osmolarity of all compartments

Compartment volume is a function of the difference between internal and external osmolarities. As external osmolarities are fixed the internal determine the compartment volumes. Therefore, by averaging the osmolarities of all the compartments (bar the soma), we can approximate the average compartment volume.

Step 2: Adjust internal impermeant anion concentration based on average osmolarity.

Düsterwald et al., (2018) showed that impermeant anion concentration can alter the cell volume without affecting the concentration of other ionic species. Therefore, to achieve the desired average osmolarity we modify the impermeant anion concentration in the compartment.

6.2. Class structure for python simulation software

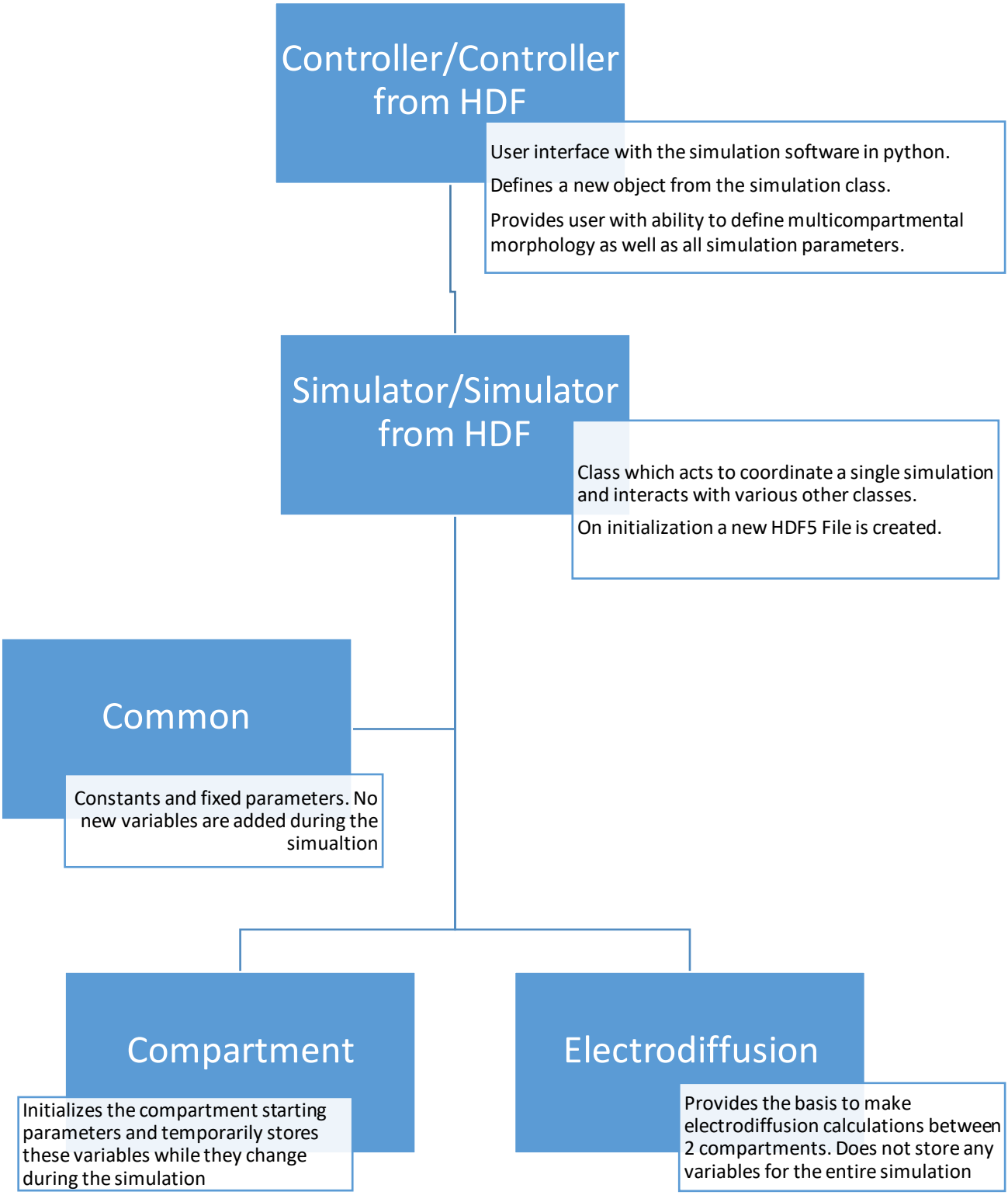

6.3. HDF5 File Structure

Sequential results at each simulation interval are saved in an HDF5 (Hierarchical Data Format version 5) which uses a directory like structure. Integration between python and HDF5 files is performed via methods contained in the h5py library. The HDF5 file for a simulation is saved in the root directory under the specified simulation name.

HDF5 files can be read and written to using python or similar language. Alternatively, HDF5 files can be opened using an open-source online reader, such as NeXus-HDF5 file viewer accessible at: https://ncnr.nist.gov/ncnrdata/view/nexus-hdf-viewer.html

Each HDF5 file will have fixed groups:

1) "COMPARTMENTS"
    - Contains a folder for each compartment label by the compartment name (e.g., "Comp1").
    - Inside each compartment folder there is a dataset for every time interval, labelled by the step number. Importantly these are not labelled sequentially as values are stored based on ASCII value order as opposed to numerical order.
    - The array stored in each compartment dataset is ordered as follows:

Item number	**Parameter**	**Unit**
0	Time	s
1	Radius	dm
2	Length	dm
3	Volume	l
4	$[Na^+]_i$	Mol/l
5	$[K^+]_i$	Mol/l
6	$[Cl^-]_i$	Mol/l
7	$[X]_i$	Mol/l
8	z	Unitless
9	$\Delta[Na^+]_i$	Mol/l
10	$\Delta[Na^+]_{leak}$	Mol/l
11	$\Delta[Na^+]_{ATPase}$	Mol/l

12	$\Delta[K^+]_i$	Mol/l
13	$\Delta[K^+]_{leak}$	Mol/l
14	$\Delta[K^+]_{ATPase}$	Mol/l
15	$\Delta[K^+]_{KCC2}$	Mol/l
16	$\Delta[Cl^-]_i$	Mol/l
17	$\Delta[Cl^-]_{leak}$	Mol/l
18	$\Delta[Cl^-]_{KCC2}$	Mol/l
19	V_m	V
20	E_k	V
21	E_{Cl}	V

2) "CURRENT-SETTINGS"

- Empty if no external current is added
  - If there is a current added there will be a subfolder with its name (e.g., "CURRENT-1"
  - Inside there will be a dataset containing the values below:

Item number	**Parameter**	**Unit**
0	Compartment number	Unitless
1	Current type: 0 = inhibitory 1 = excitatory	Unitless
2	Current start time	s
3	Current duration	s
4	Current amplitude	A
5	Current frequency	Hz

3) "ELECTRODIFFUSION"

- Contains a folder for each compartment boundary label by the electrodiffusion name (e.g., "Comp1->Comp2") .

- Inside each compartment folder there is a dataset for every time interval, labelled by the step number. Importantly these are not labelled sequentially as values are stored based on ASCII value order as opposed to numerical order.

Item number	Parameter	Unit
0	$\Delta[Na^+]_{ED}$	Mol/L
1	$\Delta[K^+]_{ED}$	Mol/L
2	$\Delta[Cl^-]_{ED}$	Mol/L
3	$\Delta[X^z]_{ED}$	Mol/L

- Values are in relation to the first compartment
    - E.g. a value of +1 in item number # represents 1 Mol/L entering compartment 1 from compartment 2

4) "SYNAPSE-SETTINGS"

- Empty if there are no synapses
- If there is a synapse added there will be a subfolder with its name (e.g., "SYNAPSE-1"
- Inside there will be a dataset containing the values below:

Item number	Parameter	Unit
0	Compartment number	unitless
1	Synapse type: = 0 ("Excitatory") = 1 ("Inhibitory")	unitless
2	Forward rate constant (α)	$s^{-1} \cdot mol^{-1}$
3	Reverse rate constant (β)	s^{-1}
4	Synapse start time	s
5	Synapse duration	s
6	Synapse end time	s
7	Maximum neurotransmitter concentration	Mol/L

8	Synaptic conductance	Siemens

5) "TIMING"
    - Contains 3 folders:
        - "DT" : time step (seconds)
        - "INTERVALS" : number of intervals save to HDF5 file
        - "TOTAL_T" : total simulation time (seconds)

6) "X-FLUX-SETTINGS"
    - Empty if there is no impermeant anion flux (X-flux)
    - If there is an X-flux added there will be a subfolder with its name (e.g., "X-FLUX-1"
    - Inside there will be a dataset containing 4 values

Item number	**Parameter**	**Unit**
0	Flux rate	Mol/s
1	z	unitless
2	Flux start time	s
3	Flux end time	s